Joining particle and fluid aspects in streamer simulations

PROEFSCHRIFT

ter verkrijging van de graad van doctor aan de
Technische Universiteit Eindhoven, op gezag van de
Rector Magnificus, prof.dr.ir. C.J. van Duijn, voor een
commissie aangewezen door het College voor
Promoties in het openbaar te verdedigen
op woensdag 4 februari 2009 om 16.00 uur

door

Li Chao

geboren te Henan, China

Dit proefschrift is goedgekeurd door de promotor:

prof.dr. U.M. Ebert

Copromotor:
dr. W.H. Hundsdorfer

To my father Li Shikai,
To my mother Yang Yumei,
and my sisters.

Contents

Chapter 1

Introduction

1.1 Streamers in nature, laboratory and applications

Streamers are a basic mode of electrical breakdown of ionizable matter in an intense electric field. When a nonconducting medium is suddenly exposed to a strong electric field, a streamer may penetrate it as a sharp nonlinear ionization wave that leaves a thin non-thermal plasma channel behind. Streamers are used in industrial applications such as ozone generation and gas purification, and they occur in nature in processes such as lightning and transient luminous events (TLEs) in the upper atmosphere.

The emergence and propagation of streamers has a long research history. When Townsend's theory [240] was not able to explain the low voltages for the breakdown of long sparks, there was a broad discussion about mechanisms by Rogowski [210], Sammer, Loeb, Meek, Raether and others in the 1920s and 30s; until Raether developed the concept of field enhancement at the streamer head [200, 201]. in the 1920s and 30s. Studies and reviews in English appeared since 1940 by Loeb [145] and Meek [156] and later by Raether [202]. Although much has been learned about streamer discharges since then, we still do not fully understand the phenomena, and extensive research is being performed to deepen our understanding.

1.1.1 Industrial applications

As in any other discharge, the basic mechanism in a streamer is the ionization of neutral molecules or atoms by electron impact. The generation rate of free electrons which are able to excite or ionize neutral particles depends on the electric field strength, and so does other chemical reactions. The characteristic feature of the streamer consists of a space charge layer around the streamer head, which enhances the field ahead of the streamer (as will be discussed in more detail in Sect. 1.2.1). This
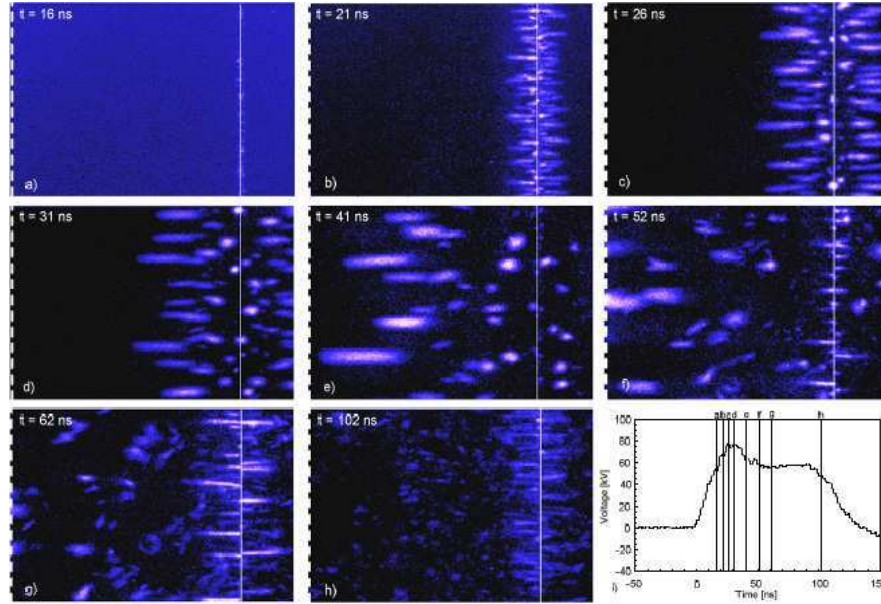
Figure 1.1: *Time-resolved side-view pictures for the corona reactor with a wire-plane electrode setup. In each picture, the white line is the wire and the dotted line the reactor wall [258].*

self-generated field ensures a sufficient ionization rate for the streamer to propagate even if the background field is too low to sustain propagation. Therefore a much lower voltage is needed between electrodes for a discharge, which makes it more efficient to produce the high energy electrons, and results in a more efficient way for molecular excitations and various chemical processes. This is used in numerous applications of streamers in so-called corona reactors.

Dust precipitators use dc corona to charge small particles in order to draw them out of a gas flow. The corona discharge has been used in the treatment of exhaust gases such as nitrogen oxides, sulfur oxides and dioxin [260, 259], or for removal of volatile and toxic compounds; this process is based on the production of radicals and ozone in the discharge [105, 106]. Fig. 1.1 shows a picture of the breakdown in a corona reactor in a wire-to-plane electrode configuration.

A new application field is the combination of chemical and hydrodynamic effects. In the streamer head, the active species, electronically excited atoms and molecules, can efficiently start and control combustion, and lead to additional mixing [229].

The "electric wind" or "ion wind" produced by corona discharges [144] has been

known for a long time. The momentum transfer from the charged particles to neutral molecules or atoms creates an electro-hydrodynamic force which was recently found to be significant in nonneutral or unipolar regions and important for flow control in aerodynamic applications [58, 28, 27].

1.1.2   Laboratory investigations of streamers

The laboratory experiments and observations are important for understanding streamers and for broadening their applications. Furthermore, a streamer discharge is the initial stage of a spark breakdown. The experiments on streamers in early days were carried out mostly in cloud chambers [145, 207] to develop a theory of the avalanche-streamer-spark process. Later, streak photography together with image intensifiers enabled researchers to image the temporal evolution of a slit-formed section of the total streamer picture with μs resolution. Recently intensified charge coupled device (ICCD) cameras yield full pictures of the streamer with exposure times as short as 1 ns [248, 73]. The latest development is the stereographic reconstruction of the streamer discharge tree in three dimensions [179, 178].

Fig. 1.2 shows snapshots of positive streamers in ambient air emerging from a positive point electrode at the upper left corner of the picture and extending to a plane electrode at the lower end of the picture. The distance between point and plane electrode is 4 cm and the applied voltage about 28 kV. With different exposure times of the ICCD camera, one obtains a picture where the light emission is integrated over the respective exposure time. On the rightmost picture with 300 ns exposure time, we see the full filamentary structure of streamers with clear channels between the two electrodes; on the leftmost picture with the shortest exposure time of 1 ns, we see actively growing heads of the channels where electric field strength and ionization rate are high. As a consequence, the other pictures have to be interpreted not as glowing channels but as the trace of the streamer head within the exposure time. Streamer velocities can therefore be directly determined as trace length divided by exposure time [39].

1.1.3   Lightning and sprite discharges in our atmosphere

Lightning is the best known natural phenomenon directly related to streamer discharges. When a lightning stroke has to pave its way from the cloud to the ground, it does it in the form of a hot leader channel whose path in turn is paved by a cold streamer zone consisting of many branched streamer channels [204]. In the past 20 years, new lightning related phenomena above thunderclouds, such as sprites and blue jets, have been discovered. These phenomena are summarized as Transient
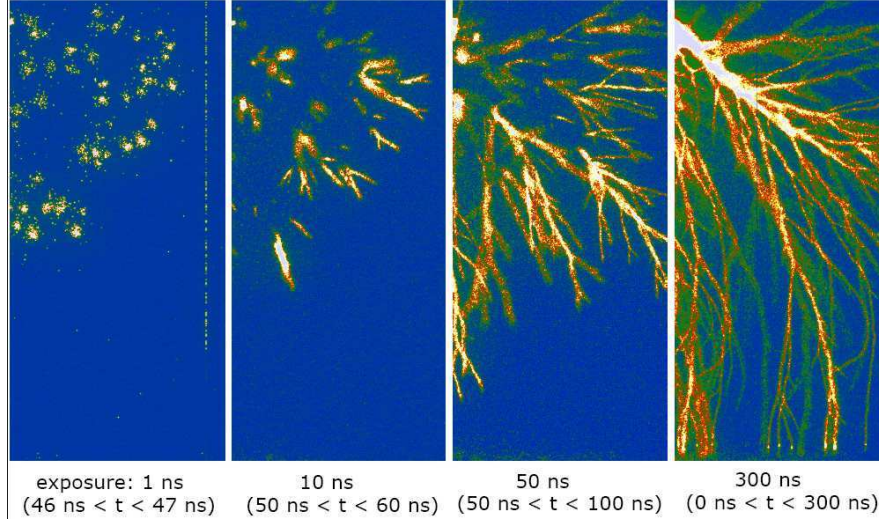
Figure 1.2: *ICCD photographs in lab experiments of positive streamers in ambient air be-tween a point electrode in the upper left corner and a plane electrode below. The photographs are taken within a 4 cm gap with an applied voltage 28 kV, and only the right halves of the fig-ures are shown. The exposure times of the photographs are 1, 10, 50, and 300 ns from the left to right, respectively. We also give the exact time interval in the brackets (where $t = 0$ is the time when the streamers emerge from the upper point). The figure is reproduced from [73].*

Luminous Events (TLEs).

Sprites are large luminous discharges, which appear in the mesosphere at 40 to 90 km altitude above large thunderstorms, stretching out over tens of kilometers in the horizontal direction as well. Sprites typically follow intense positive cloud-to-ground lightning discharges [216, 26]. When the positive charges are quickly removed from the cloud by a lightning stroke, the remaining negative charges in the thundercloud produce a strong electric field above the thundercloud up to the conducting ionosphere; the conductivity of the ionosphere is maintained by solar radiation. Sprites move with speeds of 10^7 m/s or more; in most cases they first move downward from the ionosphere [230].

Since the first images were captured in 1989 [84], sprites have been observed above thunderstorms all over the world. Different methods have been employed to observe and detect them: ground based telescopes, airplanes, satellites, and various networks for lightning detection. Fig. 1.3 shows a photograph of a sprite discharge, which consists of densely packed branching filaments. An amazing variety of sprite forms have been reported. The diameters of individual filaments range from tens to
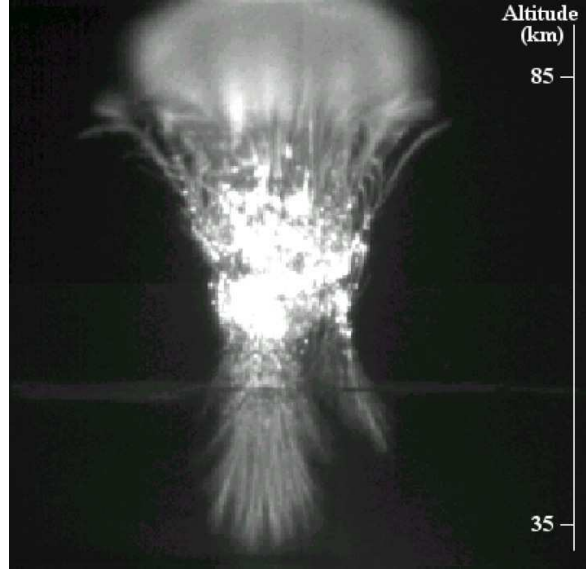
Figure 1.3: *Photograph of a sprite with the altitude indicated on the right.*

a few hundreds of meters [90, 88, 89].

Blue jets develop upwards from the cloud to terminal altitudes of about 40 km at much lower speed than sprites, about 10^5 m/s. Blue jets were originally documented during airplane based observations [255] and are characterized by a blue conical shape. A number of blue jets and gigantic blue jets were observed since then from the ground, and from space by optical detectors on satellites. Recent photographic [256] and video observations [191] of blue jets at close range have clearly shown small scale streamer structures within blue jets, similar to that reported for sprites.

1.1.4 Similarity relations between streamers and sprites

From a few centimeters for streamers produced in the laboratory to tens of kilometers for sprites, the lengths of the discharge channels vary over a large range, and the diameters do the same. But the similar filamentary structure indicates that similar mechanism may work for these physical phenomena at different length scales.

The lab experiments have been used to quantified the general properties of streamers such as velocity and diameters [262, 184, 36, 37]. Streamers were also studied at varying air density [39]. It was found that the minimal streamer diameter d_m multiplied by pressure p can be well approximated by $p \cdot d_m = 0.20 \pm 0.02$ mm·bar over

33 ms video   1 ms   50 μs
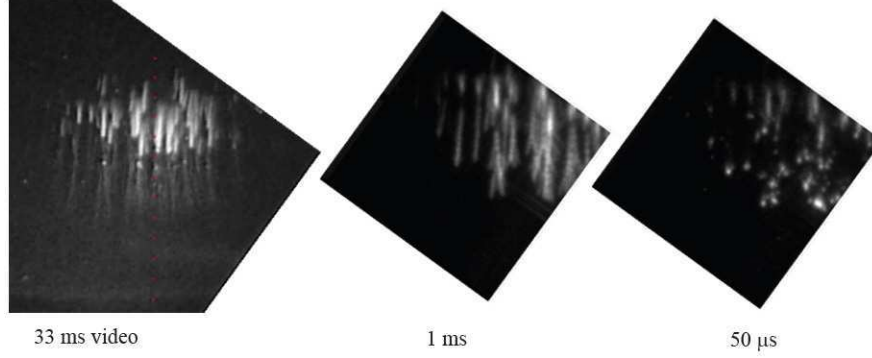
Figure 1.4: *Sprites have been recorded at 10000 frames per second with 50 μs image exposure time. The recorded sprites start with a streamer head forming at an altitude near 80 km and then move rapidly downwards while brightening. The streamer speeds vary between 10^6 and 10^7 m/s. The exposure times of the photographs are 33 ms, 1 ms and 50 μs from the left to right respectively. The figure is taken from [155]; its presentation is guided by the streamer figure 1.2.*

two decades of air pressure (10 to 1000 mbar) at room temperature. The value also fits the smallest diameters of sprite discharges at heights of 80 km where the pressure is as low as 10 μbar when extrapolated to room temperature. Furthermore, the minimal velocity of streamers and sprites is similar. This is a strong experimental support for the theoretical similarity laws discussed below and in [39].

High speed telescopic imaging of sprites also has been reported recently [136, 169]. Sprites have been recorded at 10,000 frames per second (fps) with 50 μs image exposure time [155]. At this time resolution it is possible to resolve the temporal development of streamer tips as shown in Fig. 1.4. These measurements were inspired by the earlier time resolved streamer measurements shown in Fig. 1.2. The figures demonstrate the physical similarity of sprite discharges and streamers in the laboratory.

The similarity of streamer discharges at 1 bar and sprites at 10 μbar follows from the fact that the important collisions are collisions between free electrons and neutral molecules, and that the collision frequencies, including elastic, inelastic ands ionizing collisions, are proportional to the density of the medium. Therefore the basic length scale of the streamer discharge, the mean free path ℓ_{MFP} of the electron, is inversely proportional to the density. Similarity for varying density N therefore implies that the length (i.e., mean free path, discharge length or streamer diameter, etc.) scales as $\ell = \ell_0 \frac{N_0}{N}$ where quantities with a subscript 0 correspond to reference values at standard temperature and pressure, and the electric field scales as $\mathbf{E} = \mathbf{E}_0 \frac{N}{N_0}$; the

similarity laws for densities are detailed, e.g., in [73, 39]. These similarities have motivated the introduction of the unit Townsend for the ratio $\mathbf{E}/N$ of the electric field over density, or the reduced field. In Chapter 2, actually the reduced electric field is used to characterize the results, while all other results in this thesis are presented for pressure 1 bar and at room temperature. But they can easily be converted to other gas densities. We stress that all results in this thesis are for ionization fronts in pure nitrogen where the similarity laws are ideally valid. Photo-ionization in air introduces corrections to these similarity laws above pressures of about 80 mbar [150], but these corrections seem to be negligible in the experiments [39].

1.1.5 Run-away electrons and terrestrial gamma ray flashes

In 1994, the Compton Gamma Ray Observatory (CGRO), a NASA satellite in low-Earth orbit, observed by accident that there are not only cosmic, but also Terrestrial Gamma-ray Flashes (TGFs); these flashes were later found to be clearly correlated with lightning strokes [83]. Dwyer *et al.* [72, 100] have proposed that these gamma ray flashes are due to highly energetic cosmic particles that create cosmic air showers and ionization avalanches of relativistic electrons in the high field zone inside the thundercloud. Similar relativistic run-away electron avalanches have also been suggested to initiate the lightning stroke leader in the thundercloud. They argued that the thundercloud field would be too low to start a classical discharge.

In 2003, gamma radiation was also detected at ground level in rocket triggered lightning [72]. Meanwhile, hard X-ray radiation was also found in laboratory experiments with long spark discharges [70, 203, 174]. In particular, the temporal resolution and large statistics of the study [174] shows that short X-ray bursts occur during the streamer-leader phase of the spark discharge. These X-ray bursts are clearly correlated with the streamer-leader process and not at all with cosmic air showers. The most likely candidate for gamma-radiation from sparks and lightning at ground level is therefore the streamer zone around the leader channel.

In contrast to sprites where the streamer concept can be directly applied, a lightning discharge undergoes a distinct evolution in several phases: the streamer-leader process, successive return strokes and the short-circuit along the formed channel that forms the visible lightning stroke. Streamers therefore are the very first phase that paves the way for the consecutive evolution. Streamers have a strong self-generated electric field at their growing tips and the electrons in this high field zone have a non-Maxwellian energy distribution with a long tail at high energies, as we will discuss in Chapter 2. If the electrons in the tail of the distribution occasionally reach an energy above ~100 eV, the chance that they collide with air particles (the total cross section) decreases continuously with increasing energy [100]. Electrons

then can run away from the streamer, gaining energy and consecutively diminishing friction. Bremsstrahlung then could transfer this electron energies into high energetic X-rays.

1.2   Streamer theory and the structure of the thesis

1.2.1   The streamer mechanism

Streamers typically arise from electron avalanches, either next to an electrode or somewhere in ionizable matter. The local field needs to be large enough to support the growth of the avalanche by impact ionization. This means that the electron collides with the neutral molecules (or atoms) and, if the electric field is strong enough, it eventually gains enough energy to ionize a neutral particle, releasing a new electron and a positive ion. The two electrons again gain energy from the field, both colliding with and possibly ionizing other neutrals, thereby creating a so called "electron avalanche". More precisely, the field needs to be so high, that the electron on average gains at least as much energy during its free flight, as it looses in inelastic collisions.

As long as electron and ion densities are small enough, we can neglect the charge induced field and assume that both densities grow due to impact ionization in a stationary field. However, the electrons are mobile and they will drift in the direction opposite to the electric field (while the ion mobility is much smaller and typically neglected). This will eventually create a charge layer around the ionized region that screens the electric field in the interior and enhances it in the exterior. When the charge generated field becomes comparable to the background field, a streamer emerges (as discussed in detail in [161]). Charge layer and field screening or enhancement are the characteristic features of the streamer. The enhanced field at the streamer tip allows it to penetrate undervolted regions, i.e., regions where the background electric field is too low to sustain impact ionization.

Now we need to distinguish positive (or cathode directed) and negative (or anode directed) streamers. A positive streamer propagates in the direction of the electric field and a negative streamer against the electric field. Both of them are traveling ionization waves that propagate into a nonionized region, but the electrons that advance the front come from a different source.

In a negative streamer or at the negative end of a double-headed streamer, the electrons drift into the nonionized region and impact ionization starts here as well, therefore the ionized region expands in the direction opposite to the electric field.

In a positive streamer or at the positive end of a double-headed streamer, a positive space charge layer is formed by electron depletion. The electrons move back-

ward into the streamer body, and the positive streamer can proceed only if there is a source of electrons ahead of its tip — otherwise it only can move with the much slower ion drift velocity. In air, it is generally accepted that the source of free electrons ahead of the streamer tip is the nonlocal photo-ionization, characteristic for nitrogen-oxygen mixtures. While one intuitively would expect that positive streamers in air therefore would propagate slower than negative ones, experiments show the opposite [37]. This is because the electron drift in a negative streamer actually can reduce the field enhancement at the streamer tip as found in recent simulations [151].

For positive streamers in other gases like pure nitrogen or argon, the electron source could be cosmic radiation or radioactivity, field induced detachment from negative ions or another photo-ionization mechanism. The question is under investigation.

To concentrate on a simple process with fairly known reaction rates, in this thesis only negative discharges in pure nitrogen are investigated (with the exception of Chapter 7 where the inception of a positive streamer near a needle electrode is studied).

We end by summarizing the essential ingredients of the streamer mechanism:

1. drift and diffusion of the electrons in the local field,

2. generation of electrons and ions due to impact ionization (and due to photoionization or some other nonlocal mechanism for positive streamers),

3. modification of the externally applied field by space charges.

1.2.2   Modeling approaches

Dielectric breakdown model, fluid model and particle model

Most streamers observed in nature or laboratory have very complex tree-like structures of filaments. The Dielectric Breakdown Model (DBM) was introduced originally by Niemeyer and Pietronero [177, 245] to describe the propagation of multiply branching streamers as growing fractal trees; the approach was later extended by other authors [189, 190, 7, 175]. However the dielectric breakdown model approximates the branching by simply adding new line channels based on a phenomenological probabilistic approach, and no inner structure of the streamers is included. But actually, the modeling of one single streamer channel is already a challenging job, and streamer diameters and velocities vary widely. Therefore most modeling efforts based on a microscopic description have been devoted to the initiation, propagation and branching of one single streamer channel.

The microscopic mechanisms of a streamer were summarized above. They can be incorporated either into a fluid (or density) model and into a particle (Monte Carlo) model. While the particle model traces the flight and collision of single particles [24, 130, 56], the fluid model approximates the particle dynamics by the evolution of continuous particle densities [204, 249, 163],

The fluid model usually is computationally more efficient than the particle model if the number of particles is much larger than the number of grid points where the particle densities need to be evaluated. This is normally the case except in the early stage of the avalanche phase. Fluid models have been used to simulate both positive and negative streamers and to study the structures of streamer fronts that are impossible or very hard to measure in nature or laboratory, such as the inner structure of the space charge layer or the strength of the induced field [99, 127, 249, 163].

The fluid model and its predictions

The fluid model consists of continuity equations for the plasma species and the Poisson equation for the electric field. It includes the basic physical components necessary for streamer propagation, i.e., electron drift in the local field, diffusion and impact ionization.

Solving the fluid equations numerically is not an easy task due to the multi-scale nature of streamers. The boundaries of the computational domain should be far away, while a high resolution for the inner structure of the streamer head is needed, where the electron and ion densities decay sharply and where the electric field changes rapidly in time and space. These numerical challenges have been met by adaptive grid refinement [163, 185]. Improvement of the numerical techniques is only one aspect of the recent development in the fluid models; more physics is included by using more complicated and realistic plasma-chemical models [125, 184, 193, 151], better techniques of modeling electrode geometries [14, 151] and efficient description of non-local photoionization sources [186, 30, 142, 143, 150]. The fast development of the modeling techniques have finally allowed simulational and experimental results to converge within a narrow range for some important properties of both negative and positive streamers, for example, for propagation velocities and radii of streamer channels [142, 187, 184, 151].

The phenomenon of streamer branching was studied recently in [209, 13, 142, 183, 162]. Streamer branching can develop spontaneously in a fluid simulation without introducing any fluctuation and perturbation. To understand this branching phenomenon, the thin charge layer within the streamer head can be approximated by a moving boundary which allows to study the branching instability analytically [157]. The nonlinear analysis of the ionization fronts [158, 73, 34] has given

more insights and has explained the streamer branching as a Laplacian instability.

Multiple streamers have not been studied much. Naidis has studied the correction to the streamer velocity due to electrostatic interaction with neighboring streamers in a 2-D model. Recently, Luque *et al.* [149] have shown how two streamers interact with each other in 3D simulations, which is the first result to show when and how streamers merge or repel each other; streamer merging or reconnections are studied experimentally by Nijdam *et al* [178]. A different approach to streamer interactions is presented in [148] where streamers propagate in a regular array and influence each other electrostatically.

The particle model and its predictions

The particle model is a completely different approach to streamer modeling; it follows individual electrons through the gas. The free flight of the charged particles is calculated using Newton's law, and the collisions between the electrons and the neutral species are described by a Monte Carlo method, in which the collision time is sampled by random numbers based on the collision frequency.

Particle models have been used to describe the avalanche to streamer transition [130, 65]. A particle model is very well suited to deal with the inception and avalanche phase of streamers, when the number of particles is still manageable. Particle models also have been used to simulate streamer propagation and streamer branching by using heavy super-particles [56], but the super-particle induced stochastic errors lower the quality of the represented physics in the simulation as we will show in Chapter 5.

Particle models have gained increasing interest recently because they represent the full microscopic physics, and in particular, the full behavior of individual electrons and excited molecules on an atomistic level. As already discussed in Sect. 1.2.1, streamer tips can enhance the local field much above the external field. The acceleration of electrons in these enhanced fields has been proposed [15] to explain the occurrence of X-ray radiation that was observed in experiments [239]. As discussed in Section 1.1.5, the X-ray emissions from natural and triggered lightning and long laboratory sparks may be related to the run-away electrons originating from such streamer tips. If streamers can represent a robust source of runaway electrons, the related studies may also be relevant for TGFs. In [168], the particle model has been used in a simplified electric field profile to calculate fluxes of runaway electrons. The generation rate and fluxes of such high energy electrons from a streamer need further study.

1.2.3   Motivation and scope of the thesis

We have shown in Sect. 1.1 that streamers widely occur both in nature and in applications. For many years, the simulation and modeling of streamers has been motivated by their well-known ability to generate chemically active species, which can be used for treatment of hazardous and toxic pollutants. The recent discovery of sprites and blue jets and the current questions in lightning physics and terrestrial gamma ray flashes have posed new challenges to modeling, simulations and theory.

The microscopic streamer physics has been described either by a fluid model or by a particle model. The fluid model is computationally much more efficient and has been widely used in streamer modeling. However, when physical phenomena are created by the dynamics of individual electrons, only a microscopic model such as a particle model can trace the dynamics. Here is a list of such phenomena:

1. As discussed in Sect. 1.1.5, Terrestrial Gamma ray Flashes (TGFs) and X-ray bursts from lightning and laboratory sparks question our understanding of the discharge processes in our own atmosphere [110]. Relativistic electron avalanches created by very energetic cosmic particles have been suggested to explain both TGFs and lightning inception. However, the laboratory experiments rather suggest that X-ray bursts could be due to run-away electrons from streamer heads, and that lightning by itself generates X-rays. This requires to model the electron energy distribution with its tails in the high field region at the streamer tip.

2. While streamers can branch even within the fully deterministic fluid model due to a Laplacian interfacial instability, fluctuations of the particle densities at the ionization front might trigger this instability earlier than they would occur in the fluid simulation.

3. The inception process of streamers both in laboratory and in the atmosphere is not fully understood. The particle model is very suitable to study the avalanche created by single electrons.

4. Molecule species are excited to specific levels by colliding electrons in the streamer ionization front. This is not only of interest for modeling photon emissions, but also for spectroscopic field measurements and for understanding streamer gas chemistry.

The particle model deals with the streamer dynamics at the lowest atomic level, and includes the elastic, exciting and ionizing collisions of electrons with neutral molecules that are only roughly approximated by a fluid model. But it demands an enormous computational power and storage that is far beyond the ability of present

computers for a full long streamer. This has lead to the use of super-particles, where one computational particle stands for many real particles. However, the super-particle approach causes numerical heating and stochastic artifacts, as will be discussed further in Chapter 5.

Therefore it is fair to say that neither the fluid model nor the particle model can handle macroscopic physical phenomena very well that are caused by the local non-equilibrium distribution of electron energies with its long tails. The objective of this thesis is therefore to develop a new kind of model that combines the computational efficiency and the detailed physics of the two models by coupling them in space.

The natural structure of the streamer consists of an ionized channel and an ionization front. In the channel, the electrons are dense enough to be approximated as continuous densities, and the field is too low to accelerate them to high energy. In the ionization front the electron density is decreases rapidly while the field increases, and the electrons have high energies far from equilibrium. By applying the particle model in the most dynamic and exotic region with relatively few electrons and the fluid model in the remaining region that contains the vast majority of the electrons, our aim is to follow the full 3D streamer propagation while important physics such as run-away electrons and front fluctuations are kept. The key is a hybrid model that couples particle and fluid description of the streamer in different parts of space.

1.2.4 Organization of the thesis

With the parameters re-derived from the particle swarm experiments, the fluid model is compared with the particle model for planar fronts in Chapter 2. The comparison shows a similar velocity of the ionization front and ionization level behind the front if the electric field ahead of the front is 50 kV/cm or lower. When the field is increased, the velocity does not differ much between both models, but the ionization level behind the front is substantially larger in the particle model. To understand this density difference, we zoomed into the ionization front and compared the electron mean energies obtained from the particle model with the local field approximated energies assumed in the fluid model. The local field approximated energies appear to be lower in the ionization front than the mean energies of electrons in particle simulation, while they agree well behind the front. The higher energy electrons result in higher ionization rates in the front, and consequently generate higher electron and ion densities behind the front in the particle simulation.

In Chapter 3, we present the first results of the spatially hybrid simulation for a planar front, where the particle model is applied at the ionization front and the fluid model is used for the rest. Different particle densities are obtained when the position of the model interface varies. When the model interface is put at the density

peak and the whole ionization front is included in the particle region, the hybrid simulation generates similar results as the particle simulation; when the model interface is put at the leadind edge and most of the ionization front is included in the fluid region, the hybrid model reproduces the fluid simulation results.

The first coupling attempt verified our spatial coupling concept and tested our coupling method, and it also disclosed the inconsistency of the transport coefficients between the particle model and the fluid model. In Chapter 4, instead of coupling the particle model with the classical fluid model, we introduced an extended fluid model. By adding an electron density gradient term, the extended fluid model takes the nonlocal ionization rates into account. The extended fluid model is compared with both the particle model and the classic fluid model in so-called swarm experiments; these are simulations of particles avalanches or swarms in a contant uniform electric field. The extended model generates the same swarm as in the particle simulation, and it also gives the same distribution of the initially present electrons as the particle simulation, which differs in the classical fluid model. We then coupled the particle model with the extended fluid model. The important issues in coupling, namely i) where to apply the two models, ii) how to realize a correct interaction between them, are also discussed.

The 3D fluid model and 3D particle model are developed and presented in Chapter 5. The 3D Poission equation is solved by a FISHPACK subroutine, and its numerical error is estimated with a test problem. The possible stochastical errors and the numerical artifacts in a superparticle simulation are investigated by using real particles and super-particles to simulate the same avalanche to streamer transition and comparing with each other.

The particle model and the fluid model are coupled together in 3D in Chapter 6. The 3D coupling employs the method developed for the planar front, while new techniques are also developed to cope with problems arising from the complexity of the 3D geometry. The 3D hybrid model is tested on a 3D uniform grid and first results are presented.

While we mainly develop a spatially hybrid model in the thesis, in Chapter 7 we present simulation results for the inception process of streamers near a needle electrode. The simulation implements the same needle electrode geometry as used in the laboratory. The electric field around the needle is calculated using a charge simulation method coupled with the 3D fishpack. The simulations have been done with or without the space charge induced electric field.

We end with some concluding remarks and suggestions for further research in Chapter 8.

Chapter 2

Deviations from the local field approximation in negative streamer heads

Negative streamer ionization fronts in nitrogen under normal conditions are investigated both in a particle model and in a fluid model in local field approximation. The parameter functions for the fluid model are derived from swarm experiments in the particle model. The front structure on the inner scale is investigated in a 1D setting, allowing reasonable run-time and memory consumption and high numerical accuracy without introducing super-particles. If the reduced electric field immediately before the front is $\leq$ 50 kV/(cm bar), solutions of fluid and particle model agree very well. If the field increases up to 200 kV/(cm bar), the solutions of particle and fluid model deviate, in particular, the ionization level behind the front becomes up to 60% higher in the particle model while the velocity is rather insensitive. Particle and fluid model deviate because electrons with high energies do not yet fully run away from the front, but are somewhat ahead. This leads to increasing ionization rates in the particle model at the very tip of the front. The energy overshoot of electrons in the leading edge of the front actually agrees quantitatively with the energy overshoot in the leading edge of an electron swarm or avalanche in the same electric field.

2.1   Introduction

Streamers [145, 202] are growing filaments of weakly ionized non-stationary plasma produced by a sharp ionization front that propagates into non-ionized matter. Streamers are used in industrial applications such as lighting [134, 22] or gas and water purification [247, 97], and they occur in natural processes as well such as lightning [19, 71, 257] or transient luminous events in the upper atmosphere [216]. Therefore accurate modeling and simulation of streamers is of high interest.

Most streamer models (see e.g. [64, 99, 249, 126, 127, 14, 77, 163, 215, 150]) are so called fluid models for the densities of different particle species in the discharge. These models build on the assumption of local equilibrium: transport and reaction coefficients in the continuity equations are functions of local parameters only. If this parameter is the local electric field, we refer to this assumption as the *local field approximation*. This assumption is commonly considered to be valid as long as equilibration length or time scales are much smaller than the spatial or temporal gradients in the electric field. For the strongly varying electric fields within a streamer ionization front, the validity of the local field approximation was investigated in [173, 131, 142]. The general 'sentiment' in these studies is that the approximation suffices for practical purposes and that more detailed methods tracking the behavior of individual particles lead to just minor corrections.

Another recent result supporting the fluid approximation for streamers was that even streamer branching [248, 38, 73] can be understood in terms of an inherent instability of the fully deterministic fluid equations [13, 209, 73, 163, 162]. These studies have shown that a streamer in nitrogen can reach a state in which the width of the space charge layer that creates the field enhancement at the streamer tip, is much smaller than the streamer diameters; the streamer then can branch spontaneously due to a Laplacian interfacial instability.

However, despite success and progress of fluid approximations and simulations for streamers, there are three major reasons to reinvestigate the local field approximation:

1. Not all streamers are alike. Experiments as well as simulations show that rapidly applied high electric voltages can create streamers that are more than an order of magnitude faster and wider than streamers at lower voltages [36]. Whether earlier findings on streamers in lower potentials apply to those fast and wide streamers as well has to be investigated.

2. The detection of x-rays emanating from lightning strokes [69, 226, 70, 168] indicates that electrons can gain very high energies within early stages of the lightning event. Therefore runaway electrons within streamer and leader pro-

cesses should be investigated. Runaway electrons by definition violate a local approximation.

3. Streamer branching is an inherent instability of a fully deterministic fluid model. However, fluctuations of particle densities might trigger this instability earlier than they would occur in the fully deterministic fluid model. In particular, in the leading edge of an ionization front, particle densities are very low and the fluid approximation eventually breaks down. As the front velocity of this so-called pulled front [77, 75] is determined precisely in the leading edge region, single particle dynamics and fluctuations should be accounted for.

These three observations motivate our present reinvestigation of the local field approximation for streamers. The starting point is a Monte Carlo model for the motion of single free electrons in nitrogen. We note that complete streamers have been simulated with Monte Carlo particle models before [56], however, a drawback of such models is that the computation time grows with the number of particles and eventually exceeds the CPU space of any computer. This difficulty is counteracted by using super-particles carrying charge and mass of many physical particles; but super-particles in turn create unphysical fluctuations and stochastic heating.

In the present paper, we compare the results of a Monte Carlo particle model and a fluid model. We circumvent the problems caused either by a too large particle number or by the introduction of super-particles by investigating a small, essentially one-dimensional section of the ionization front as illustrated in Fig. 2.1. We suppress effects of lateral boundaries by periodic boundary conditions. As the electric field essentially does not deviate from the planar geometry within the region where the particle densities vary rapidly, a planar ionization front [132] is a very good approximation of this inner structure. Of course, a planar front will not incorporate the electric field enhancement caused by a curved front [64, 132], but this outer scale problem concerns only the electric field and can be dealt with through an inner-outer matching procedure [21, 81, 74]. Planar fronts allow us to investigate individual particle kinetics and fluctuations within the front and its specific strong spatio-temporal gradients in a systematic way and within reasonable computing time.

In this paper, we concentrate on negative streamer fronts in pure nitrogen under normal conditions. We thoroughly discuss the case where the reduced electric field at the streamer tip is 100 kV/(cm bar), and we summarize results for fields ranging from 50 to 200 kV/(cm bar). The paper is organized as follows. In Sect. 2.2, first our Monte Carlo particle code and its numerical implementation are described. Then the derivation of the fluid model is recalled, and the numerical implementation of the fluid model is summarized. Then swarm or avalanche experiments in a fixed
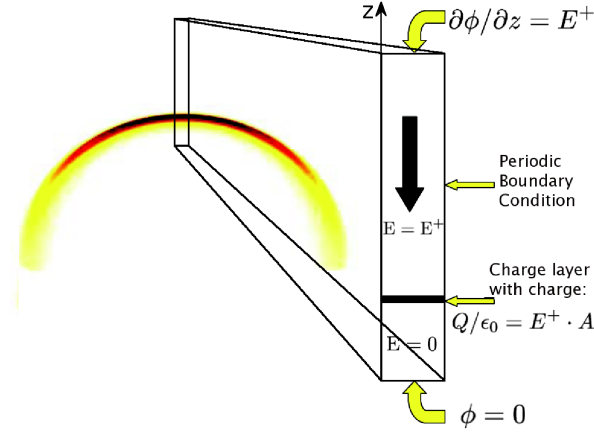
Figure 2.1: *The relation between the full streamer problem and the planar fronts described in this paper: the left picture shows the narrow space charge layer surrounding the negative streamer head [209, 163, 162]; the width of the layer is much smaller than the streamer diameter which creates the characteristic field enhancement ahead and field suppression behind the front. The right picture shows a zoom into the inner structure of the space charge layer with an essentially planar ionization front as treated in this paper. In the transversal direction, periodic boundary conditions are applied. The simulation can start initially with charge Q evenly distributed in a thin layer of transversal area A. Q is so large that it screens the field below the charge layer.*

field are performed in the particle model, the approach of electrons to a steady state velocity distribution is investigated, and the parameter functions for the fluid model are generated. This sets the stage for a quantitative comparison of front solutions in particle and fluid model in Sect. 2.3. Here first the setup of planar front simulations is described, then the results of the planar front simulations within fluid and particle model and analytical results are presented and compared. The emphasis lies on front profile, front velocity and ionization level behind the front. It will be shown that differences can be attributed to the electron kinetics in the leading edge of the front where the electric field does not vary, and that the electron energy distribution there agrees quantitatively with that in the leading edge of an ionization avalanche or swarm. Sect. 2.4 contains our conclusions on the validity of the fluid approximation. An appendix contains analytical approximations on the ionization level behind an ionization front.

2.2 Set-up of particle model and fluid model in local field approximation

In this section, we summarize features of particle and fluid models, their numerical implementation and mutual relation as a basis for the quantitative comparison of ionization fronts in particle and fluid model in Sect. 2.3.

Our starting point is a model that contains all microscopic physical mechanisms that are thought to be relevant for the propagation of a negative impact ionization front in pure nitrogen. It models the generation and motion of single free electrons and positive ions in the neutral background gas. While propagating freely, the electrons follow a deterministic trajectory according to Newton's law. The collision of electrons with neutral molecules is treated as a stochastic Monte Carlo process. Because the mobility of the positive ions is two orders of magnitude smaller than that of the electrons, ions are treated as immobile within the short time scales investigated in this paper. Neutral molecules are assumed to have a uniform density with a Maxwellian velocity distribution. The electron-neutral collisions, including all relevant elastic, excitation, and ionization collisions, are treated with the Monte Carlo method. Electron-electron or electron-ion processes as well as density changes of the neutral gas are neglected as the degree of ionization stays below 10^{-5} even at atmospheric pressure [77, 73]. This well-known model will be summarized in Sect. 2.2.1. The space charges can change the local electric field, this is accounted for by solving the Poisson equation. The particle model gives a very detailed and complete description at the expense of significant computational costs where we stress that one particle is one electron and super-particles are not used.

If densities are high enough and fields vary slowly in space and time, the average behavior of the electrons can be modeled by a fluid approximation for electron and ion densities whose parameters depend on the local electric field only. The derivation of the fluid approximation can be formalized by taking the zeroth and the first moment of the Boltzmann equation. However, for the practical purpose of determining mobilities, ionization rates and diffusion coefficients as a function of the electric field, we directly perform swarm experiments with the particle model in a constant electric field. This procedure together with the averaging processes involved are described in Sect. 2.2.3. Here also the relaxation of an electron swarm to steady state motion and the velocity distribution of steady state motion in a given homogeneous field are discussed.

2.2.1   The Monte Carlo particle model

Physical processes

In the particle scheme, at each instant of time t, there is a total number of $N_e(t)$ electrons and $N_p(t)$ ions. The single electrons are numbered by $i = 1, \ldots, N_e(t)$ at time t; they are characterized by a position $\mathbf{x}_i(t)$ and a velocity $\mathbf{v}_i(t)$, each within a continuous three dimensional vector space. Between collisions, electrons are accelerated and advanced according to the equation of motion. For the positive ions, only their position $\mathbf{x}_j^p$, $j = 1, \ldots, N_p(t)$ is taken into account while their mobility is so low that their velocity can be neglected. The electric field is determined from the Poisson equation together with appropriate boundary conditions.

The collisions account for the impact of free electrons on neutral nitrogen molecules. As the neutrals are abundant, their density determines the probability of an electron-neutral collision. The collision can be elastic, inelastic or ionizing. In inelastic collisions, electron energy is partially converted into molecular excitation; in ionizing collisions, electron energy is consumed to split the neutral into a positive ion and a second free electron. The probability distribution of the different collision processes depends on the electron energy at the moment of impact; we use the cross section data from the SIGLO Database [165]. As the collisions are random within a probability distribution, the actual occurrence of a specific collision within a sample is determined by a Monte Carlo process.

Once an elastic or inelastic collision process is chosen, the energy loss of the electron and therefore the absolute value of its velocity after the collision is fixed. However, model results will depend on the angular distribution of the emitted electrons, which again follows a probability distribution. Different scattering methods have been discussed in the literature [129, 181, 195, 29, 234]. Here we will only focus on the scattering method used in the present paper.

In an elastic collision, the longitudinal scattering angle χ and the azimuthal scattering angle φ relative to the direction of the incident electron, are given in [181]. In an inelastic collision, the energy loss of incident electrons has to be taken into account, but the scattering angle is calculated in the same way as for an elastic collision.

In an ionizing collision, energy conservation dictates

$$\varepsilon_1 + \varepsilon_2 = \varepsilon_c - \varepsilon_{ion} \tag{2.1}$$

where ε_c, ε_1 and ε_2 are the energy of the incident, the scattered and the ejected electron, respectively, and ε_{ion} is the ionization threshold energy. We use Opal's

empirical fit [182] for the distribution of the ejected electron energy

$$\varepsilon_2 = B \tan\left[p_1 \arctan \frac{\varepsilon_c - \varepsilon_{ion}}{2B}\right], \tag{2.2}$$

where $B \approx 13$ eV in the energy range of interest and p_1 is a random number equally distributed between 0 and 1. For the scattering angles, Boeuf and Marode [29] assumed that (i) the incident, ejected and scattered electron velocities are coplanar, and (ii) that the scattered and ejected electron velocities are perpendicular. These assumptions lead to

$$\cos^2 \chi_1 = \frac{\varepsilon_1}{\varepsilon_c - \varepsilon_{ion}}, \qquad \cos^2 \chi_2 = \frac{\varepsilon_2}{\varepsilon_c - \varepsilon_{ion}}. \tag{2.3}$$

where $\chi_{1,2}$ are the respective scattering angles. The set of equations (2.1), (2.2), and (2.3) determines the distribution of energies and scattering angles of the scattered and the ejected electron in an ionizing collision.

Numerical implementation

The particle code moves electrons within the applied plus the self-induced field and includes their collisions. Therefore the numerical calculation consists of three parts: the Newtonian electron motion within the field, the field generated by the charged particles, and collisions. At each time step of length Δt, the field is calculated from the charge densities on a lattice with grid size $\Delta \ell$. Then the electrons move in continuous phase space according to the field, possibly interrupted by Monte Carlo collision processes. Electrons can experience more than one collision during one time step Δt.

In more detail, position and velocity of the electrons are determined in continuous phase space from their Newtonian equation of motion according to the electric field at their initial position within the time interval. The commonly used integration is the leap-frog method [24], in which the electron positions and velocities are offset in time by $\Delta t/2$.

For the electron-neutral collisions, time, type and scattering angles are determined in a Monte Carlo process by sequences of random numbers. For N_2, the maximal average collision frequency $\nu_{\max}$ is about 9.7×10^{12}/s, therefore the minimal average collision time $T_{\min} = 1/\nu_{\max}$ is about 0.1 ps. By introducing so-called null-collisions, in which no collisions occur, $T_{\min}$ can be chosen as average collision time independently of the electron energy ε. The probability $P(t)$ that an electron will travel a time t without collision (including null collisions) is

$$P(t) = e^{-\nu_{\max}t}. \tag{2.4}$$

Therefore the next collision time $\Delta t_{collision}$ of an electron is drawn in a Monte Carlo process from the distribution

$$\Delta t_{collision} = T_{\min} \cdot \ln \frac{1}{p_2} \tag{2.5}$$

where p_2 is again a random number. When a collision occurs, the energy of the incident electron is calculated, and the distribution of the collision processes is determined according to the collision frequencies; then a random number determines the collision type (null collision, elastic, excitation or ionization collision). At the collision, the electron velocities are changed according to the processes discussed in Sec. 2.2.1. Then the next collision time for the particle is determined. This approach is described in more detail in [29, 42].

At each time step of length Δt, the electric field is calculated on the grid with mesh $\Delta \ell$. First, the number of elementary charges $n_p - n_e$ within a grid cell is counted; it directly determines the charge density within the cell. Then the change of electric field components normal to the cell faces are determined from the densities within the cells through the Poisson equation. This simple interpolation on cells of appropriate size causes no artifacts as we are dealing with particles carrying just one elementary charge e, not with super-particles. The condition on the cell size is (i) that it is large enough that a elementary charge in the cell center does not create substantial fields on the cell boundary, and (ii) that it is small enough that no strong density gradients occur between neighboring cells. Here it should be noted that density gradients due to particle number fluctuations are strongly suppressed when we deal with real particles, not super-particles. Therefore more involved interpolation methods like Particle in Cell (PIC) [24] are not required.

The choice of the spatial and temporal mesh determines the computational accuracy as well as the computational costs. We have tested different meshes in planar fronts as described in Sect. 2.3.1. The results, most prominently the ionization density behind the front, converge for a sufficient discretization. However, a balance has to be found between computational accuracy and computational costs. We choose the time step as $\Delta t = 0.3$ ps, which is of the same order as the minimal average collision time $T_{\min}$, and the cell size as $\Delta \ell = 2.3$ μm, which is the basic length scale according to dimensional analysis in [77]. On this mesh, the electron density behind planar fronts has an error of less than 0.2%.

2.2.2 The fluid model

Derivation from the Boltzmann equation

Fluid models in general can be derived from the Boltzmann equation [107, 57, 221, 93]. They approximate the motion of charged particles by continuity equations:

$$\frac{\partial n_e}{\partial t} + \nabla \cdot \mathbf{j}_e = \mathcal{S} \tag{2.6}$$

$$\mathbf{j}_e = -\mu \mathbf{E} n_e - \mathbf{D} \nabla n_e \tag{2.7}$$

where n_e is the electron density, $\mathbf{j}_e = \mathbf{u} n_e$ is the flux density and $\mathbf{u} = \langle \mathbf{v} \rangle$ is the mean velocity of electrons. $\mathcal{S}$ is the source of electrons due to collisions and impact ionization, μ represents the mobility and $\mathbf{D}$ is the diffusion matrix.

The coefficients $\mathcal{S}$, μ and $\mathbf{D}$ appearing in equations (2.6) and (2.7) are to be obtained from elsewhere. One common approach [103] is to solve the Boltzmann equation for a homogeneous and constant electric field E within a background gas of constant density. In a uniform electric field, the electrons gain energy from the field and loose it in inelastic collisions, reaching some steady state transport conditions [212, 8]. We will derive our coefficients directly from swarm experiments in the particle model in the next section. Furthermore, the electron source term can be written as

$$\mathcal{S} = |n_e \ \mu(E) \ \mathbf{E}| \ \alpha(E), \tag{2.8}$$

when attachment and recombination can be neglected. Using these coefficients in a given gas and density as a function of the electric field is called the local field approximation.

Of course, this fluid model has to be extended by continuity equations for other relevant excited or ionized species. For a non-attaching gas with neglected ion mobility, the continuity equation for the density n_p of positive ions has to be included

$$\frac{\partial n_p}{\partial t} = \mathcal{S}. \tag{2.9}$$

Alternatively, the fluid model (2.6)–(2.9) can also be motivated by physical considerations and conservation laws [77, 161, 163]. The continuity equations coupled to the Poisson equation for the electric field,

$$\nabla \cdot \mathbf{E} = \frac{\mathrm{e} \ (n_p - n_e)}{\epsilon_0}. \tag{2.10}$$

In the present paper, the highest possible consistency between particle and fluid model is achieved by determining the transport coefficients and ionization rate $\mu(E)$,

matrix $\mathbf{D}(\mathbf{E})$, and $\alpha(E)$ for the fluid model from swarm experiments in the particle model; this will be done in Sect. 2.2.3.

Solutions of the particle model and of the fluid model in local field approximation will differ when the electric field or the electron density vary rapidly in space or time as the electrons then will not fully "equilibrate" to the local electric field [173]. We will investigate these deviations further below.

Numerical implementation

The fluid equations are solved on a uniform grid where the electron densities n_e and ion densities n_p are calculated at the centers of the grid cells. The densities can be viewed as averages over the cell like in the particle model. The field strength is also calculated at the cell centers. The electric field components are taken on the cell faces, where they determine the mass fluxes.

The equations for the particle densities are discretized in space with the finite volume method, based on mass balances for all cells. The particle densities are updated in time using the third order upwind-biased advection scheme combined with a two-stage Runge-Kutta method. For the details and the tests of the algorithm, we refer to [163].

Analytical studies [77, 75] and numerical investigations [162, 163] show that the ionization front is a pulled front; therefore a very fine numerical grid is required in the leading edge region of the front, and standard refinement techniques refining in the interior front region fail. Like for fronts in the particle model, we also have tested different numerical meshes for fronts in the fluid model, these fronts are treated in Sect. 2.3.1. On a too coarse grid, the front moves too fast and is too smooth due to numerical diffusion of the electron density. To achieve the same numerical accuracy below 0.2 % as for the particle model, the fluid model requires an approximately four times finer mesh, namely $\Delta \ell = 0.575~\mu$m and $\Delta t = 0.075$ ps. This mesh will be used below.

2.2.3   Kinetics and transport of electron swarms in constant fields

Swarm experiments deal with electron swarms moving and multiplying in a constant electric field without changing it. If the field is high enough such that the electron number grows measurably, such a swarm is also called an avalanche. Swarms or avalanches in homogeneous fields are an important experimental and theoretical tool to investigate the electron dynamics.
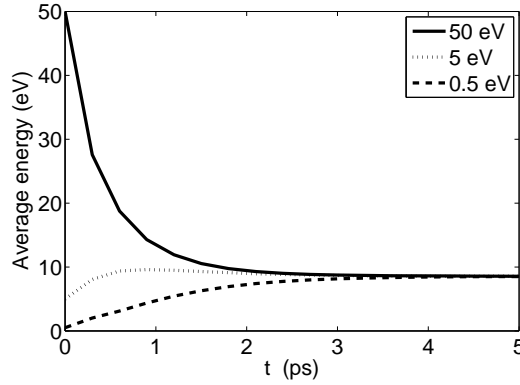
Figure 2.2: *Average electron energy as a function of time for three different electron swarms in a field of* 100 *kV/cm. Starting with electron swarms moving into the drift direction with an identical kinetic energy of 50 eV (solid), 5 eV (dotted) and 0.5 eV (dashed), all electron swarms approach a mean electron energy characteristic for the applied field within 2 to 3 ps.*

Particle swarm kinetics: approach to steady state

Particle swarm experiments can be used to determine transport coefficients, but also to study the particle kinetics. We will first study the second issue, namely the relaxation of electrons to a steady state velocity distribution and the velocity distribution itself. Indeed the electron swarm will rapidly "equilibrate" to the applied field. In such a balanced state, the electrons on average gain as much energy from the electric field as they loose in inelastic and ionizing collisions; this is how they reach an energy and velocity distribution specific for the electric field. The time that the electrons need to get in balance with the local electric field is an important indication for the validity of the local field approximation. We therefore test it here within a particle swarm experiment.

Fig. 2.2 shows how different electron swarms converge to the same mean energy within a field of 100 kV/cm. The experiment starts with a group of electrons of identical velocity directed in the electron drift direction; their kinetic energy is 50, 5 and 0.5 eV, respectively. When the swarms start to drift, their average energies converge to the same constant value within at most 3 ps in all three cases. Here the average energy is used as the simplest indication of their energy and velocity distribution function.

After reaching steady state motion, swarms demonstrate a steady state distribution of electron velocities and energies in a given electric field. Fig. 2.3 shows the distribution of the longitudinal electron velocity v_z in an electric field of 50, 100,
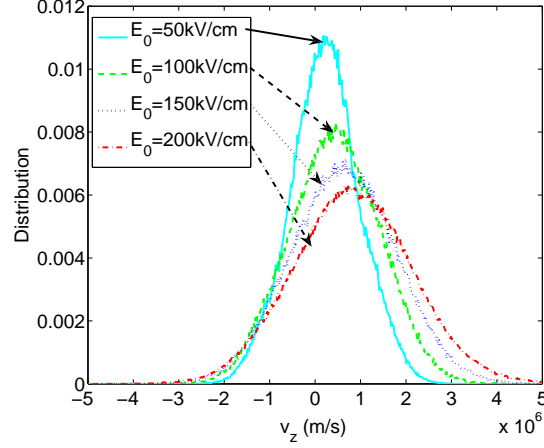
Figure 2.3: *Distribution of the electron velocity v_z in the longitudinal direction in particle swarm experiments in fields of 50, 100, 150, and 200 kV/cm. The higher the field, the more the distribution deviates from Maxwellian and from symmetry about velocity $v_z = 0$.*

150, and 200 kV/cm. The figure shows that with increasing field, the electron velocity distribution deviates more and more from the Maxwellian profile and therefore from symmetry about velocity $v_z = 0$; rather an increasing number of electrons flies in the direction of the field and a decreasing umber against it, and the number of electrons with high kinetic energy increases.

Gaussian swarm profiles and transport coefficients

Swarm experiments are used as well to determine mobilities, reaction rates and diffusion constants experimentally [109]. An electron swarm drifts, broadens and grows under the influence of a constant electric field. The same experiment is performed here for this purpose, but now numerically with the particle model.

We here recall the essentials: A single electron will generically evolve into a swarm that has a Gaussian profile in space. In terms of the fluid model (2.6)–(2.9), this Gaussian distribution is given by

$$
\begin{aligned}
n_e(x, y, z, t) \quad \propto \quad & e^{\,\mu E \alpha(E)\, t}\ \frac{e^{-(x^2 + y^2)/(4\pi D_T(t - t_0))}}{4\pi D_T(t - t_0)} \\
& \cdot \frac{e^{-(z - z_0 - \mu E t)^2/(4\pi D_L(t - t_0))}}{\sqrt{4\pi D_L(t - t_0)}},
\end{aligned}
\tag{2.11}
$$

(The discharge specific context of this solution can be found in [204, 161].) Here the center of the package is at $(x, y, z) = (0, 0, z_0)$ at time $t = 0$, and the field is in the z-direction. The longitudinal and transversal components of the diffusion matrix are denoted as D_L and D_T.

The transport and reaction coefficients can be determined from this equation by

$$\mu(E)|E| = \frac{\langle z(t_2) \rangle - \langle z(t_1) \rangle}{t_2 - t_1}, \tag{2.12}$$

$$\alpha(E) = \frac{1}{\mu(E)|E|} \frac{\ln N_e(t_2) - \ln N_e(t_1)}{t_2 - t_1}, \tag{2.13}$$

$$D_T(E) = \frac{\langle x^2(t_2) + y^2(t_2) \rangle - \langle x^2(t_1) + y^2(t_1) \rangle}{4(t_2 - t_1)}, \tag{2.14}$$

$$D_L(E) = \frac{\langle [z(t_2) - \langle z(t_2) \rangle]^2 \rangle - \langle [z(t_1) - \langle z(t_1) \rangle]^2 \rangle}{2(t_2 - t_1)}, \tag{2.15}$$

where $N_e(t)$ is the total number of electrons at time t, and $\langle \cdots \rangle$ denotes the average over all particles.

Fluid parameters determined from particle swarms

We have determined $\mu(E)$, $D_T(E)$, $D_L(E)$, and $\alpha(E)$, and also the average electron energy $\epsilon(E)$ in particle swarm experiments for 42 different background electric fields ranging from 2 kV/cm to 205 kV/cm.

To obtain the transport coefficients and mean values with satisfactory statistics, one needs a sufficient number of electrons that have experienced an adequate number of collisions. The experiments start from a number of electrons at the same position (i.e. located in a single point, which is, a Gaussian with zero width), and end with a swarm of electrons with a Gaussian distribution as described in equation (2.11). Because the ionization rate depends strongly on the electric field strength, the number of initial electrons and the simulation time is chosen according to the fields. For example, the simulation starts with 10^6 electrons at 2 kV/cm and lasts for 1500 ps, but for 205 kV/cm, the simulation starts with 10^2 electrons and ends with 4×10^6 electrons after 30 ps.

As there is some initial transient during which the electrons "equilibrate" to the field and approach a Gaussian density profile, the transport and reaction coefficients are evaluated according to equations (2.12)–(2.15) at appropriate times $t_{1,2}$. We choose t_2 as the end of a swarm experiment, and $t_1 = t_2/2$ in the middle of an experiment. In view of the relaxation times below 3 ps evaluated above, this choice of t_1 is on the very safe side.

Mobility $\mu(E)$

Ionization rate $\alpha(E)$

Transversal diffusion $D_T(E)$

Longitudinal diffusion $D_L(E)$
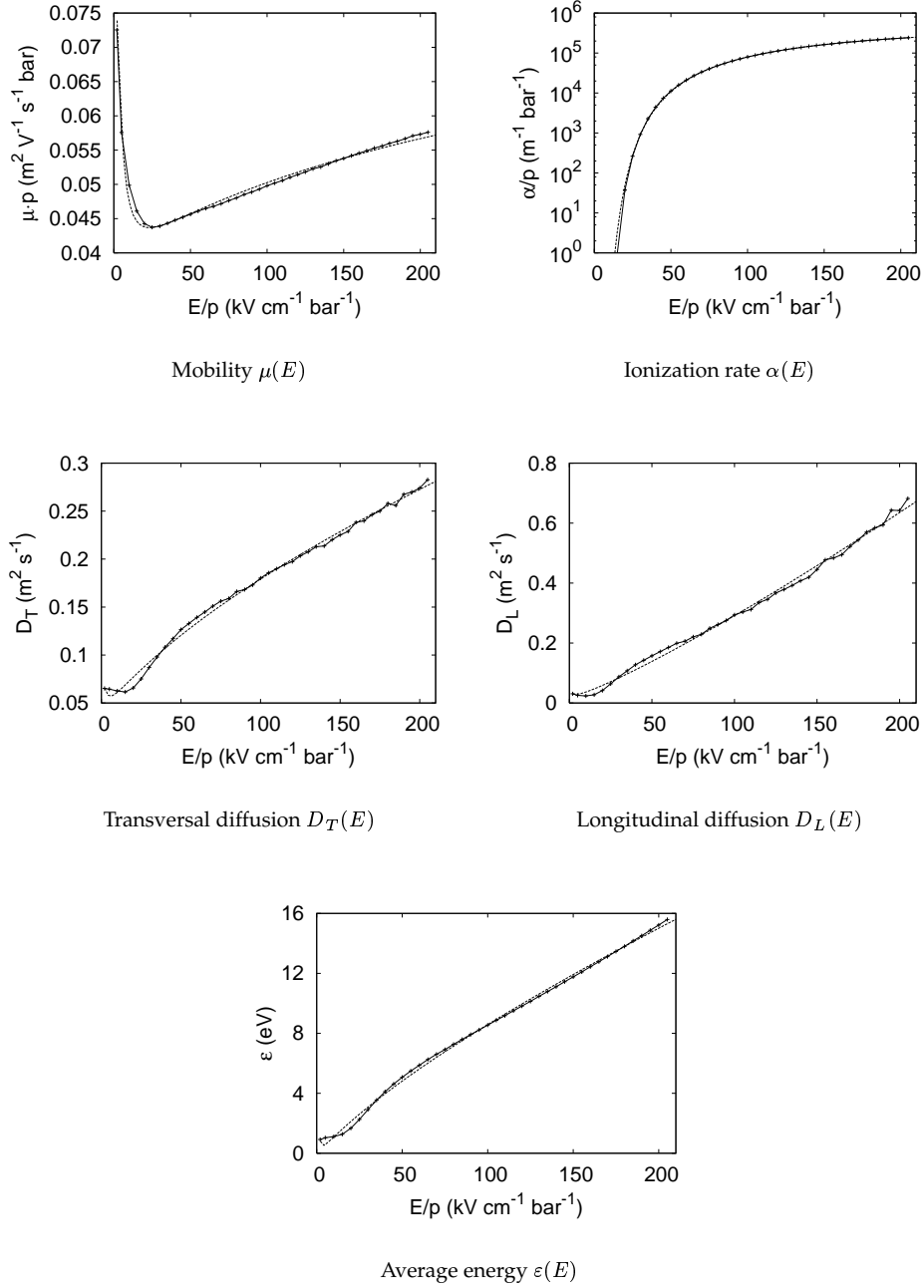
Average energy $\varepsilon(E)$

Figure 2.4: *Electron mobility, diffusion rates, ionization rate and average electron energy in nitrogen. Plotted are the reduced coefficients μp, α/p, D_T, D_L and ε as a function of reduced field E/p at room temperature. Our units are related to other commonly used units like 100 $kV\,cm^{-1}\,bar^{-1} = 131.6\ V\,cm^{-1}\,torr^{-1} = 372$ Townsend at T=300 K.*

function	Unit	a	b	c	d
μ	$\mathrm{m}^2/(\mathrm{V} \cdot \mathrm{s})$	-4.02	0.21	5.44	2.42
α	$1/\mathrm{m}$	12.5	0.16	-200	19.2
D_T	m^2/s	-4.71	0.64	4.80	1.84
D_L	m^2/s	-6.75	1.18	7.89	2.49
ε	eV	-1.37	0.78	-4.44	3.46

Table 2.1: *The units and parameters in the empirical fit formula Eq. (2.16) for reduced coefficients and average energy.*

The numerical results for μ, D_T, D_L, α and ϵ for different electric fields $E = |\mathbf{E}|$ are presented in Fig. 2.4 together with empirical fit formulas. These formulas are in the form of

$$\mathrm{function}(E) = \mathrm{Unit} \cdot \exp\left[a + b \cdot \ln \frac{E}{\mathrm{kV/cm}} + \frac{c \cdot \mathrm{kV/cm}}{E} \pm \left(\frac{d \cdot \mathrm{kV/cm}}{E}\right)^2 \right], \quad (2.16)$$

where "$\pm$" is "$+$" for α and ε, and "$-$" for μ, D_T, and D_L. Their units and parameters a, b, c, and d are listed in Tab. 2.2.3.

These coefficients will be used in the fluid model (2.6)–(2.9) to reach optimal agreement between particle and fluid model.

2.3 Simulations of planar fronts

2.3.1 Concepts and set-up of planar ionization fronts

The role of planar fronts in the inner analysis of the streamer structure

Fluid model simulations of streamers within the past 20 years (see e.g., [64, 249, 163, 150]) have shown that the streamer head is surrounded and preceded by an ionization front that propagates into the non-ionized gas. Within the ionization front, ionization grows until space charge effects set in. The formed space charge layer is much thinner than the radius of the streamer, it leads to a screening of the electric field in the interior of the streamer head and to a field enhancement ahead of it. Therefore the field dependent ionization reaction coefficient $\alpha(E)$ is enhanced ahead of the space charge layer and suppressed behind it. The space charge layer around the streamer is shown in Fig. 2.1, for a further discussion of the three-dimensional structure and growth of streamers, we refer to the literature, see, e.g., [73].

It is clear that the full configuration of the electric field can only be analyzed within a two- or three-dimensional setting. On the other hand, within the inner structure of ionization front and space charge layer, the electric field does not deviate

much from a planar configuration. To analyze the processes within the ionization front in detail, it is therefore advisable to study the inner structure of a planar front. This will be done here. The results can be put in further physical context through a separate analysis on the inner and the outer scale of the structure as commonly done in hydrodynamic boundary layer analysis, reaction-diffusion systems etc. [21, 81, 74].

Construction of planar fronts in the particle model

The construction of a planar front is straight forward in the fluid model: gradients ∇ are simply evaluated in one spatial direction. We choose this direction to be the z direction. In the particle model, on the other hand, electrons move in all three spatial dimensions. Therefore a three-dimensional setting has to be retained. An essentially one-dimensional setting is achieved by considering only a small transversal area A of the front and by imposing periodic boundary conditions at the lateral boundaries. Furthermore, the electric field is calculated only in the forward direction z through

$$E_z(z,t) = E_z(z_0,t) + \int_{z_0}^{z} dz' \int_A \frac{dx\,dy}{A} \frac{\mathrm{e}(n_p - n_e)(x,y,z',t)}{\epsilon_0} \qquad (2.17)$$

where E_z is the electric field in the z-direction, and z_0 can be any arbitrary position. This means that fluctuations of the transversal field due to density fluctuations in the transversal direction are not included. In fact, the numerical implementation of (2.17) is performed on a grid in the forward direction only as discussed in Sect. 2.2.1.

The density fluctuations projected onto the forward direction depend on the transversal area A over which the averages are taken. When A increases, the total number of electrons in the simulation increases proportionally to A, while the relative density fluctuations decrease like $1/\sqrt{A}$. Therefore some intermediate value of the area A has to be chosen: On the one hand, there should be a sufficient number of electrons to reach a satisfactory statistics, but on the other hand, there shouldn't be so many electrons that the computer runs out of memory within the time interval of interest. In the simulation, we use a small A for high electric field and a large A for low electric field. For example, we choose the transversal averaging area as $A = 6\,\Delta\ell \times 6\,\Delta\ell$ for -100 kV/cm, but for -50 kV/cm, the transversal averaging area is $A = 20\,\Delta\ell \times 20\,\Delta\ell$, here $\Delta\ell = 2.3\,\mu$m.

In the z direction, the system length is $500\,\Delta\ell$ which allows the front to propagate freely for all runs reported in this paper. The electric field in the non-ionized region at large z is specified by $\mathbf{E} = E^+\,\hat{\mathbf{z}}$, where $E^+ < 0$ and $\hat{\mathbf{z}}$ is the unit vector in the z direction.

In the simulations, two different initial conditions are used. In the first, N_e electrons are evenly distributed in a thin layer of area A with an extension of $19.5\,\Delta\ell <$
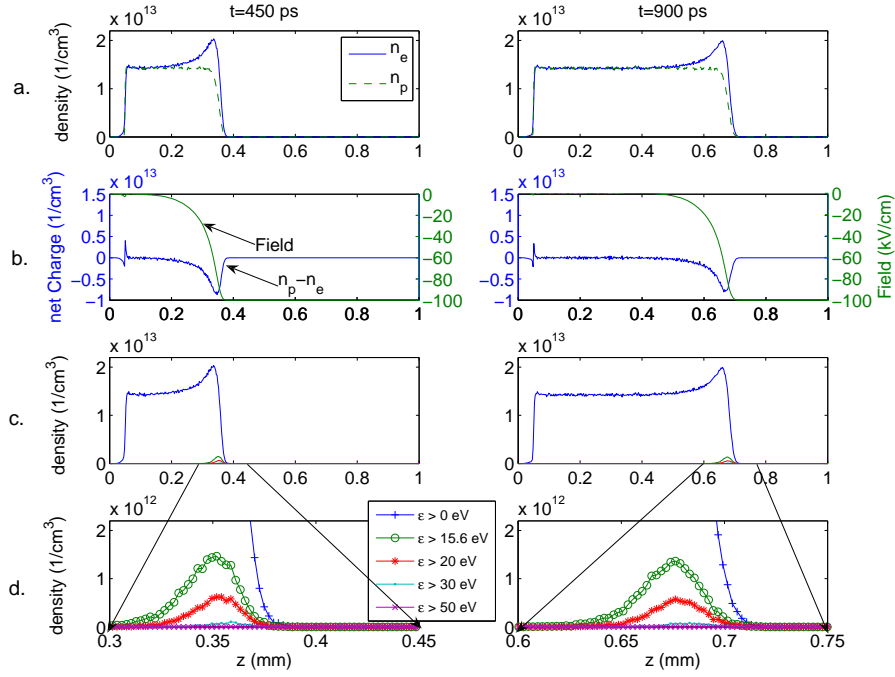
Figure 2.5: *Spatial profile of a particle front within a field of* -100 *kV/cm at time* $t_1 = 450$ *ps (left) and* $t_2 = 900$ *ps (right). (a) Electron density (solid) and ion density (dashed), (b) electric field (dashed) and net charge (solid), (c) density of electrons with energy above 0 eV, 15.6 eV, 20 eV, 30 eV and 50 eV, (d) zoom into the front region with high electron energies, same quantities as in (c).*

$z < 20.5 \, \Delta\ell$ in the field direction. Choosing

$$N_e/A = |E^+| \cdot \epsilon_0/e; \tag{2.18}$$

the field behind the layer is screened according to (2.17). Another choice is to begin with a few seed electrons which will create an ionization avalanche and form a charge layer later.

2.3.2   Planar fronts in the particle model

Qualitative discussion of typical results

We first present results in a field of $E^+ = -100$ kV/cm. The initial condition is a thin electron layer with total electron number N_e as in (2.18), screening the electric field behind the layer. Fig. 2.5 presents the evolution at times $t_1 = 450$ ps (left) and $t_2 = 900$ ps (right). Panel (a) shows the density distribution of the electrons (solid) and the ions (dashed). Panel (b) shows the net negative charge distribution (solid) and the electric field (dashed). Panel (c) shows the total charge density of electrons and the charge density of electrons with an energy higher than 0, 15.6, 20, 30, and 50 eV, where 15.6 eV is the ionization energy. Panel (d) zooms into panel (c), both in space and in electron densities.

The figure shows an ionization front propagating to the right; up to fluctuations, the spatial profiles are essentially unchanged, therefore the front velocity v is essentially constant as well. The front carries an overshoot of electrons, generating a thin space charge layer that screens the electric field behind the front. In this screened interior region, the electron and ion density reach an equal constant density $n_e^- = n_p^-$. (Upper indices "$\pm$" indicate quantities before "$+$" and behind "$-$" the ionization front.) The qualitative features of the front are the same as those in the fluid model [77].

Electrons with energies above the ionization threshold of 15.6 eV are shown in the lower two panels in Fig. 2.5; they exist essentially only in the high field region. Electrons with energies above 30 eV are so rare that they are hardly seen even on the scale of panel (d). Electrons with energy above 50 eV exist, but cannot be distinguished within this plot. The profiles of high energy electrons also move with the whole front without change of shape, up to fluctuations.

Following the track of single electrons of high energy, we found that they gain and loose energy in few collisions within a few ps and do not run away. In that sense they are in a fast dynamic equilibrium with the electrons at lower energies. This observation agrees with the fast relaxation of 50 eV electrons travelling in the forward direction whose energy relaxation is shown in Fig. 2.2.

Quantitative results in different fields

The ionization front in a given field E^+ is characterized by a velocity v, a degree of ionization $n_e^- = n_p^-$ behind the front and an electron energy distribution in the high field region. We now present these quantities in detail.

We define the front position as the position of the maximal electron density. Table 2.2 summarizes our numerical results on the front velocity v as well as on the

E^+ (kV/cm)	v (m/s)	n_e^- (1/cm^3)
50	$(2.773 \pm 0.007) \times 10^5$	$(5.923 \pm 0.031) \times 10^{11}$
75	$(4.845 \pm 0.023) \times 10^5$	$(4.372 \pm 0.011) \times 10^{12}$
100	$(7.258 \pm 0.062) \times 10^5$	$(1.422 \pm 0.003) \times 10^{13}$
125	$(1.012 \pm 0.010) \times 10^6$	$(3.233 \pm 0.007) \times 10^{13}$
150	$(1.365 \pm 0.008) \times 10^6$	$(6.014 \pm 0.006) \times 10^{13}$
175	$(1.745 \pm 0.027) \times 10^6$	$(9.875 \pm 0.020) \times 10^{13}$
200	$(2.262 \pm 0.063) \times 10^6$	$(1.486 \pm 0.004) \times 10^{14}$

Table 2.2: *Numerical results on planar fronts in the particle model: front velocity v and ionization level n_e^- behind the front as a function of the electric field E^+ ahead of the front.*

saturated electron density n_e^- behind the front as a function of the electric field E^+ immediately ahead of the front.

2.3.3 Planar fronts in the fluid model

For planar fronts in the fluid model, there are not only numerical, but also analytical results, both agree within the numerical accuracy. First, the velocity of the front in a field E^+ is given by

$$v^* = \mu(E^+) \, |E^+| + 2\sqrt{D_L(E^+) \, \mu(E^+) \, |E^+| \, \alpha(E^+)}, \qquad (2.19)$$

according to [77, 132] with a slight generalization along the general lines discussed in [74]. Note that for the initial conditions treated in this paper, the velocity v^* is approached from below after an algebraically slow relaxation [74].

The electron and ion densities decay exponentially like e^{-z/ℓ^*} in the leading edge of the front where the electric field is approximately E^+ [77, 74]. The decay length is

$$\ell^* = \sqrt{\frac{D_L(E^+)}{\mu(E^+) \, |E^+| \, \alpha(E^+)}}. \qquad (2.20)$$

These analytical results are summarized in Table 2.3.

For the degree of ionization behind the front n_e^-, there is no closed analytical solution. The ionization behind the front can be derived numerically. Furthermore, in the appendix, we derive an analytical upper bound for this quantity, namely

$$n_e^- \lesssim n_{e,bound}^- = \frac{\epsilon_0}{e} \int_0^{|E^+|} \alpha(e) \, de. \qquad (2.21)$$

Numerical result and analytical bound are summarized in table 2.4.

E^+	v^*	ℓ^*
(kV/cm)	(m/s)	(m)
50	2.68×10^5	7.83×10^{-6}
75	4.70×10^5	3.91×10^{-6}
100	7.14×10^5	2.72×10^{-6}
125	9.88×10^5	2.15×10^{-6}
150	1.29×10^6	1.84×10^{-6}
175	1.63×10^6	1.66×10^{-6}
200	1.98×10^6	1.54×10^{-6}

Table 2.3: *Exact analytical results for planar fronts in the fluid model, evaluated with the transport coefficients from Fig. 2.4– 2.4: front velocity v^* and electron density decay length ℓ^* as a function of the electric field E^+.*

E^+	n_e^-	$n_{e,bound}^-$
(kV/cm)	(1/cm^3)	(1/cm^3)
50	5.43×10^{11}	5.80×10^{11}
75	3.83×10^{12}	3.98×10^{12}
100	1.17×10^{13}	1.22×10^{13}
125	2.49×10^{13}	2.61×10^{13}
150	4.35×10^{13}	4.58×10^{13}
175	6.70×10^{13}	7.09×10^{13}
200	9.50×10^{13}	10.1×10^{13}

Table 2.4: *The degree of ionization n_e^- behind the front in the fluid model as a function of field E^+: numerical result n_e^- and analytical upper bound $n_{e,bound}^-$ as derived in the appendix.*

2.3.4   Comparison of planar fronts in particle and fluid model

Detailed investigation in a field of $-100\,\mathrm{kV/cm}$

Now the stage is set to compare planar fronts in the particle model to those in the fluid model, The comparison is first done in detail for a planar front propagating into a field of $-100\,\mathrm{kV/cm}$. Both fluid and particle simulations are carried out in the same setup starting from the same initial conditions, i.e., from an electrically neutral group of 100 electrons and ions evenly distributed within the thin layer $19.5\,\Delta\ell < z < 20.5\,\Delta\ell$ and within the transversal area $A = 6\,\Delta\ell \times 6\,\Delta\ell$.

Fig. 2.6 shows the temporal evolution of the planar front. We compare the spatial profile of the electron density (solid line) and ion density (dotted) in a particle simulation with the electron density (dashed) and ion density (dot-dashed) in a fluid simulation. Two features are clearly visible: First, the particle and the fluid
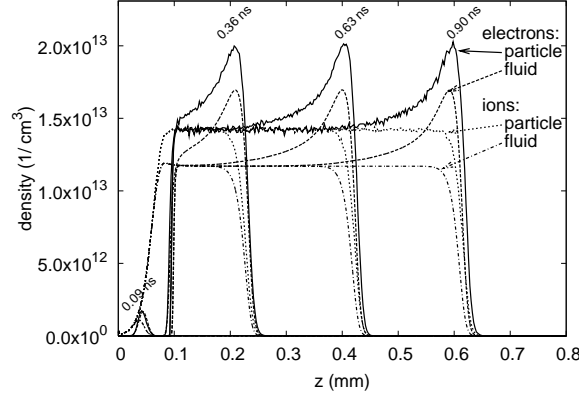
Figure 2.6: *Temporal evolution of the electron and ion densities in a planar front in a field of E^+=-100 kV/cm. Shown are the spatial profiles of electron and ion densities derived with the particle or the fluid model at time steps $t = 0.09$ ns, 0.36 ns, 0.63 ns, and 0.9 ns (solid lines: $n_{e,part}$, dashed: $n_{e,fluid}$, dotted: $n_{p,part}$, dot-dashed: $n_{p,fluid}$).*

front move with approximately the same velocity and the same density profile in the leading edge of the front where the electric field does not vary yet. Second, the maximal electron density in the front and the saturation level of the ionization behind the front in the particle model are about 20 % higher than in the fluid model. These results of visual inspection agree with those of tables I and III for a field of -100 kV/cm.

As we have excluded other reasons of the discrepancy like numerical discretization errors or inconsistent transport and reaction coefficients, deviations must be due to the approximations in the fluid model, and a closer inspection shows that we should focus on the electron energies.

Fig. 2.7 zooms into the ionization front shown in Fig. 2.6 at time $t = 0.63$ ns. Here we show the electron density (solid line) and electric field (dot-dashed line) in the particle model. Furthermore the local mean energy of the electrons in the particle model is indicated with a dotted line. Finally, the mean electron energy according to the local field approximation $\epsilon(E)$ is derived from the local field E and equation (2.16) for $\epsilon(E)$; it is indicated with a dashed line. It can be seen that the average electron energy nicely follows the local field approximation in the interior of the ionized region while it is considerably higher in the region where the electric field is large and the electron density decreases rapidly.

This deviation is analyzed in more detail in Fig. 2.8 where the full electron energy distribution is shown. This is done for the particular spatial region of the front
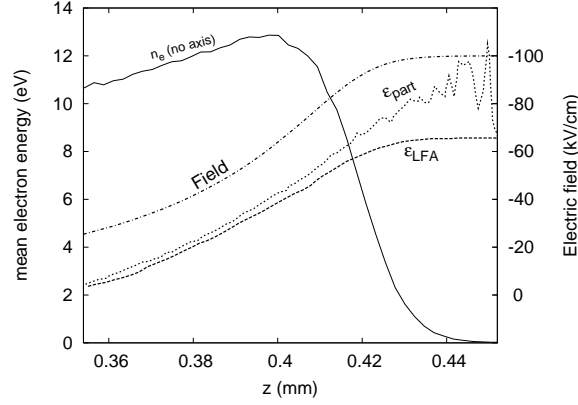
Figure 2.7: *Zoom into the particle ionization front of Fig. 2.6 in a field of -100 kV/cm at time 0.63 ns: shown are electron density distribution n_e (solid line), local average electron energy $\varepsilon_{\mathrm{part}}$ (dotted line), local average electron energy $\varepsilon_{\mathrm{LFA}}$ according to the local field approximation (dashed line), and electric field strength E (dot-dashed line).*
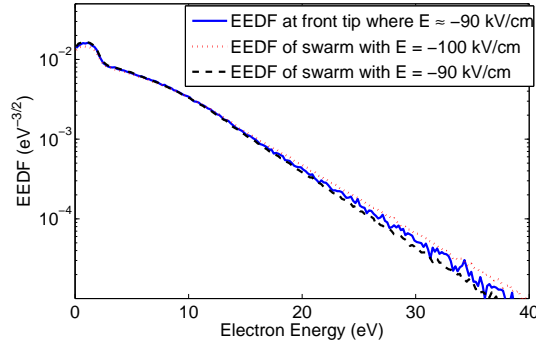
Figure 2.8: *The electron energy distribution function is measured as $P(\varepsilon)/\sqrt{\varepsilon}$, where $P(\varepsilon)$ is the probability of electron energy ε. Here we show the electron energy distribution at the front region of Fig. 2.7 where $E \approx -90$ kV/cm (solid line) and in the swarm experiments in constant fields of -90 kV/cm (dashed line) and -100 kV/cm (dotted line).*

where the electric field has decreased by 10% to a value of -90 kV/cm. More precisely, electrons are collected from the first cell where $|E| > 90$ kV/cm, searching with increasing z. The average field in these cells is about $E = -91.47$ kV/cm. To reach a satisfactory statistics, the electrons are collected from 10 different instants of time with a temporal distance of 30 ps between the two consecutive sampling
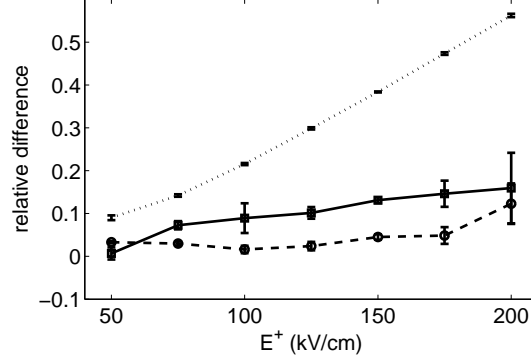
Figure 2.9: *Relative difference of ionization level behind the front (2.22) (dotted, above), front velocity (2.23) (dashed, below), and mean electron energy in the leading edge (2.24) (solid, middle) between particle and fluid model as a function of the electric field E^+ ahead of the front.*

times to ensure statistical independence. While these data are plotted as a solid line, for comparison the electron energy distributions in the swarm experiments in a constant field of -90 and -100 kV/cm are plotted as a dashed or dotted line, respectively. Analyzing the electron energy distribution at low energies $\varepsilon < 10$ eV, the ionization front at a local field around -90kV/cm and the swarm experiment in a constant field of -90 kV/cm are quite similar while the distribution for a swarm in a field of -100 kV/cm is clearly lower. On the other hand, for electron energies above 20 eV, the energy distribution in the ionization front at a local field of -90 kV/cm actually lies closer to the distribution of the swarm at -100 kV/cm than to that at -90 kV/cm. This observation not only confirms that the average electron energy in the leading edge of the ionization front is higher than in the local field approximation, as is consistent with Fig. 2.7, but it indicates that the higher mean energies correspond to a higher population of electron energy states above the ionization threshold. We therefore expect that also the ionization rates are higher in the particle model than in the local field approximation.

Results for other fields

Having analyzed the front propagating into a field of $E^+ = -100$ kV/cm in detail, we now summarize equivalent results for fields ranging from -50 to -200 kV/cm

in Fig. 2.9. The figure shows the relative difference

$$\frac{n_{e,\text{ part.}}^- - n_{e,\text{ fluid}}^-}{n_{e,\text{ fluid}}^-} \tag{2.22}$$

of the saturated electron density behind the front between the particle and the fluid model, the relative difference

$$\frac{v_{\text{part}} - v_{\text{fluid}}}{v_{\text{fluid}}} \tag{2.23}$$

of the front velocity and the relative difference

$$\frac{\langle \varepsilon_{\text{part}} \rangle - \langle \varepsilon_{\text{LFA}} \rangle}{\langle \varepsilon_{\text{LFA}} \rangle} \tag{2.24}$$

of the mean electron energy between the particle model and the local field approximation at a point in the ionization front where electron densities are low and the electric field is just slightly screened to the value $E = 0.98\ E^+$. All differences increase with increasing field.

2.3.5   Interpretation of results

Electric field gradient, electron motion in the front and electron energy overshoot

A few authors have dealt with particle discharge models with strong gradients both in the electric field and in the particle density. They analyzed deviations between particle models and the fluid model in local approximation by means of the Boltzmann equation, as treated in Sect. 2.2.2. They analyzed the case of stationary gradients of the electric field [212, 8] and the case of positive streamer ionization fronts [173]. They suggested corrections to the fluid model both due to field gradients and to density gradients.

   The situation in negative streamer ionization fronts is somewhat different: a negative ionization front in nitrogen moves approximately with the electron drift velocity determined by the electric field in the leading edge of the ionization front. This means that the electrons in this leading edge region on average move within a stationary electric field. More precisely, the front velocity $v^*(E^+)$ from (2.19) is slightly larger than the electron drift velocity $\mu(E^+)\ |E^+|$ in the electric field ahead of the front. This is because the front is not carried by electron drift only, but also by diffusion and creation of new free electrons. In a coordinate system moving with the ionization front, the existing electrons therefore on average move backwards. This motion is the faster, the further they are behind.

   Fig. 2.8 shows that the high energy tail of the electron energy distribution in the ionization front at the position where the field is -91.47 kV/cm, is closer to the

swarm experiment at $-100\,\mathrm{kV/cm}$ than to that at $-90\,\mathrm{kV/cm}$. One could interpret these results by assuming that the electrons have gained their energy distribution in a field of close to $-100\,\mathrm{kV/cm}$ and then are transported backwards to where the field is only $-90\,\mathrm{kV/cm}$.

However, Fig. 2.7 shows that this interpretation cannot be true. If the electron energy distribution would first "equilibrate" to a field of $-100\,\mathrm{kV/cm}$ and then partially be transported backwards, then the mean electron energy $\langle \epsilon_{\mathrm{part}} \rangle$ would everywhere be below the mean electron energy $\langle \epsilon_{\mathrm{LFA}} \rangle$ at $-100\,\mathrm{kV/cm}$ in local field approximation. But clearly there is an electron energy overshoot in the leading edge of the ionization front. So the most prominent deviation from the fluid model visible in Fig. 2.7 occurs in the region were the electric field is almost constant; furthermore, if it would be a consequence of the local field approximation, the deviation would have the opposite sign.

Density gradient and relation between front and swarm experiments

We conclude that the electron energy overshoot in the leading edge of the ionization front has to be due to the electron density gradient rather than to the field gradient. The effect of density gradients can be tested in swarm experiments (cf. Sect. 2.2.3) in a constant electric field as well. It turns out that such a test goes beyond qualitative results and actually allows for a quantitative comparison of fronts and swarms as will be explained below.

The key to the quantitative comparison is based on two closely related facts: (i) the density profiles in the leading edge of a swarm or avalanche in a constant field and in the leading edge of an ionization front penetrating the same field are both given by

$$n_e \sim e^{-z/\ell^*},\tag{2.25}$$

where ℓ^* is given by (2.20) and in table II. (ii) Also the velocities of swarm and front have the same value v^* from (2.19) and table II.

This relation between velocities and decay rates of swarms and fronts holds generally for any so-called pulled front whose velocity is determined in the linearly unstable region ahead of the front, as is discussed in a general setting in [74], specifically in Sect. 2.5.1. The statement can be verified on the explicit form of the Gaussian profile (2.11): in the coordinate

$$\xi = z - z_0 - v^* t\tag{2.26}$$

moving with velocity v^*, the Gaussian swarm distribution (2.11) can be written as

$$n_e \propto e^{\,\mu|E|\alpha t}\,\frac{e^{-(z-z_0-\mu E t)^2/(4D_L t)}}{\sqrt{4\pi D_L t}} = e^{-\xi/\ell^*}\,\frac{e^{-\xi^2/(4D_L t)}}{\sqrt{4\pi D_L t}}.\tag{2.27}$$
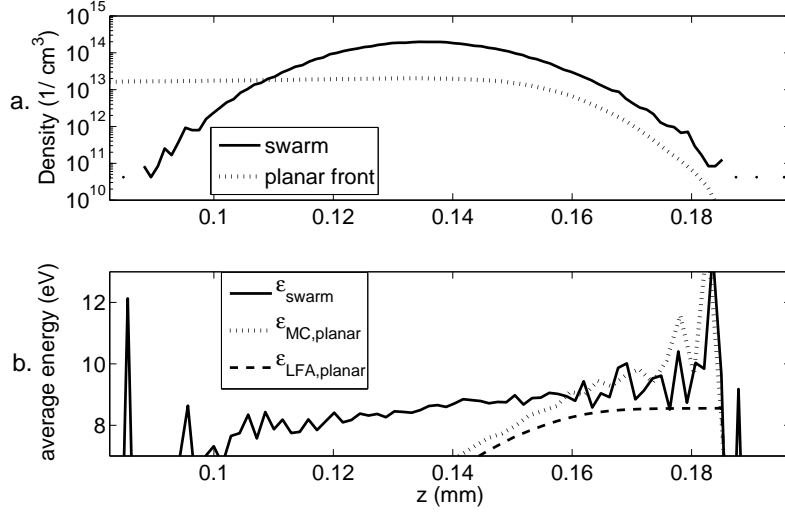
Figure 2.10: *Comparison of an electron swarm and a planar ionization front, both in the particle model and in a field of −100 kV/cm. (a) Electron density on a logarithmic scale for swarm (solid) and front (dotted) as a function of z. (b) Mean electron energy in swarm (solid) and front (dotted) and in the front assuming the local field approximation (dashed) as a function of z.*

We now test the above theoretical predictions on the particle model for a swarm and a planar front in a field of −100 kV/cm. The results are shown in Fig. 2.10. It should be remarked that our electron swarm has a Gaussian density distribution both in the longitudinal and in the transversal direction. To focus on the profile in the longitudinal direction, the density in the swarm in Fig. 2.10(a) is taken as the density on the longitudinal axis. Fig. 2.10(a) shows the electron density profile of the swarm decaying at both edges and the profile of the planar front that grows and saturates to a constant level. As the densities are plotted on a logarithmic scale, an exponential decay like in (2.25) amounts to a straight line with slope $−1/\ell^*$ in the plot. Despite density fluctuations and slow transients in the buildup of the profile [74], Fig. 2.10(a) indeed shows that swarm and front have a similar decay profile on the right hand side.

This sets the stage to compare now the electron energies of swarm and front in Fig. 2.10(b). The dotted and the dashed line reproduce lines from Fig. 2.7 for the planar particle front, they show the actual mean electron energy $\langle \varepsilon_{\mathrm{part}} \rangle$ (dotted) and the mean electron energy according to the local field approximation $\langle \varepsilon_{\mathrm{LFA}} \rangle$ (dashed). For the electron swarm, the mean electron energy along the swarm axis is indicated

as a solid line in Fig. 2.10(b). It is remarkable that this energy within the swarm is not constant in space though the electric field has a constant value. Rather the energy increases almost linearly along the axis. While the average energy of the swarm is around 8.5 eV, producing the respective value for the local field approximation $\varepsilon(E)$ in Fig. 2.4, the average energy at the leading edge of the swarm reaches values above 10 eV.

Now the leading edge regions of swarm and front need a closer inspection. The leading edge is defined as the region where the electric field is (almost) constant and where the electron densities both approach the profile (2.25). It is in this region where the electrons attain the highest mean energies, and Fig. 2.10(b) shows that the mean energy profiles of swarm and front in this region are virtually identical up to fluctuations. We conclude that the high electron energies within the leading edge of the ionization front that are shown in figures 2.7 and 2.8, are due to the electron density gradient, and can be studied in the leading edge of a swarm experiment as well.

The ionization density behind the front

The discussion above shows that within the electron density gradient, the fast electrons are on average a bit ahead of the slower electrons as they have a higher average velocity in the forward direction. This is understandable since on the one hand, each single fast electron looses its energy over a length of ~ 1.5 μm (which is the electron drift velocity $\mu(E)E$ times the relaxation time ~ 2 ps from Fig. 2.2), but on the other hand, the gradient length $\ell^* \approx 2.7$ μm of the density profile is of the same order. Clearly, this effect becomes the more pronounced, the higher the field.

Now the electron energies in the leading edge substantially exceed the local field approximation and indicate the presence of a larger fraction of electrons with energies above the ionization threshold. This leads also to higher ionization rates than estimated by the local field approximation $\alpha(E)$. As the ionization level behind the front $n_e^- = n_p^-$ is well approximated by the effective ionization rate α integrated over the fields within the front (2.21) (recall also the argument in the appendix), it is clear that the ionization level behind the front is higher in the particle model than in the fluid model.

2.4   Conclusion

Negative streamer ionization fronts in pure nitrogen were investigated in planar approximation, both following the kinetics of single electrons in a particle model, and in a fluid model in local field approximation. As parameter functions for the fluid

model were derived from swarm experiments in the particle model and numerical errors are under strong control, a discrepancy between results of particle and fluid model must be attributed to the approximations made in the fluid model.

For electric fields immediately ahead of the front of 50 kV/cm or lower — the statements hold for nitrogen under normal condition, they are easily extended to other densities by introducing the reduced electric field E/N —, particle and fluid model essentially agree in front speed, profile and ionization level behind the front. When the field increases, the velocity does not vary much between both models, but the ionization level behind the front is substantially larger, as is demonstrated for a field of 100 kV/cm in Fig. 2.6. In Fig. 2.9 the differences between particle and fluid model are summarized for the full field region investigated.

Can the discrepancy between the models be attributed to a particular physical mechanism and to a particular part of the front region? In Fig. 2.7 we find the largest discrepancy between fluid and particle model in the leading edge of the front where the electron density is very low and where the electric field is hardly screened. Here the electrons have an average energy considerably higher than estimated by the local electric field. This effect can only be explained by an effect of the electron density gradient, not of the electric field gradient. Indeed, an electron swarm or avalanche in a constant electric field has the same velocity and the same density gradients in its leading edge and shows the same electron energy overshoot in its front part, as is illustrated in Fig. 2.10. In essence, in high fields the gradient length of front and avalanche ℓ^* becomes of the order of the electron energy relaxation length, therefore the fast and energetic electrons can get ahead of the slower ones.

These higher electron energies in the leading edge of the front lead to higher ionization rates than the ionization rate $\alpha(E)$ in local field approximation — indeed, $\alpha(E)$ is the total effective ionization rate of a complete electron swarm (as derived in Sect. 2.2.3) while the electrons in the leading edge of the swarm have higher ionization rates.

Now the ionization level behind the front can be approximated by integrating the effective ionization rate $\alpha(E)$ over the electric field strength E, independently of the precise spatial structure of the front. This result is derived in the appendix. This implies that higher electron energies and higher effective ionization rates in the leading edge of the front directly lead to higher ionization levels behind the front, even though only very few electrons are involved in this dynamics in the low density region.

The effect of few electrons of high energy is much more severe for the ionization rates α than for the average drift velocity μE, therefore the most pronounced effect is seen in the ionization levels behind the front, and less in the front velocities.

We finally remark that next to explicit predictions, our work has delivered two

useful insights: (i) the physical discrepancies between particle and fluid model lie in the leading edge of the front, though the effect is not so much seen in the velocity, but much more in the ionization level behind the front. This gives a clue for a numerical strategy combining efficient features of fluid and particle model. (ii) The essential features in the leading edge of the front are equally present in the leading edge of an electron swarm or avalanche in a constant field, where it can be studied much easier.

Chapter 3

Spatial coupling of particle and fluid models for streamers: where nonlocality matters

The question is not what you look at, but what you see.

Henry David Thoreau

Particle models for streamer ionization fronts contain correct electron energy distributions, runaway effects and single electron statistics. Conventional fluid models are computationally much more efficient for large particle numbers, but create too low ionization densities in high fields. To combine their respective advantages, we here show how to couple both models in space. We confirm that the discrepancies between particle and fluid fronts arise from the steep electron density gradients in the leading edge of the fronts. We find the optimal position for the interface between models that minimizes computational effort and reproduces the results of a pure particle model.

3.1 Coupling concept

Streamers generically occur in the initial electric breakdown of long gaps. They are growing filaments of weakly ionized nonstationary plasma; they are produced by a sharp ionization front that propagates into non-ionized matter within a self-enhanced electric field. Streamers are used in industrial applications such as lighting [23], gas and water purification [260, 98] or combustion control [229], and they occur in natural processes as well such as lightning [205, 257] or transient luminous events in the upper atmosphere [216, 188]. Important recent questions concern (i) propagation and branching of streamers [73] and the role of avalanches created by single electrons, (ii) the electron energy distribution in the streamer head and the subsequent gas chemistry that is used in the above applications, as well as (iii) runaway electrons and X-ray generation, possibly in the streamer zone of lightning leaders [72, 188]. The present paper deals with the efficient simulation of these problems.

Monte Carlo particle simulations [43, 56] model these effects as they contain the full microscopic physics; the deterministic electron motion between collisions is calculated and collisions of electrons with neutrals are treated through a Monte Carlo process with appropriate statistical weights. The particle model includes the complete electron velocity and energy distribution as well as the discrete nature of particles. However, a drawback of such models is that the required computation resources grow with the number of particles and eventually exceed the CPU space of any computer. This difficulty is counteracted by using superparticles carrying the charge and the mass of many physical particles, but superparticles in turn create unphysical fluctuations and stochastic heating.

Streamers are therefore mostly modeled as fluids (see e.g. [163, 215, 168, 143, 150]) since a fluid model is computationally much more efficient. In the case of a negative discharge in a pure non-attaching gas like nitrogen, it consists of continuity equations for the densities of electrons n_e and positive ions n_p coupled to the Poisson equation for the electric field $\mathbf{E}$. The electron mobility μ and diffusion matrix $\mathbf{D}$ and the impact ionization rate α are calculated from microscopic scattering and transport models like the Boltzmann equation [103] or directly from Monte Carlo simulations as, e.g., in Chap. 2. In streamer calculations, it is generally assumed that these transport and reaction coefficients are functions of the local electric field.

We have compared the properties of streamer ionization fronts of particle models and conventional fluid models, see Chap. 2 for negative planar fronts in nitrogen; the transport coefficients for the fluid model were generated from swarm experiments in the particle model. We found that the models agree reasonably for fields up to 50 kV/cm at standard temperature and pressure, but that differences increase
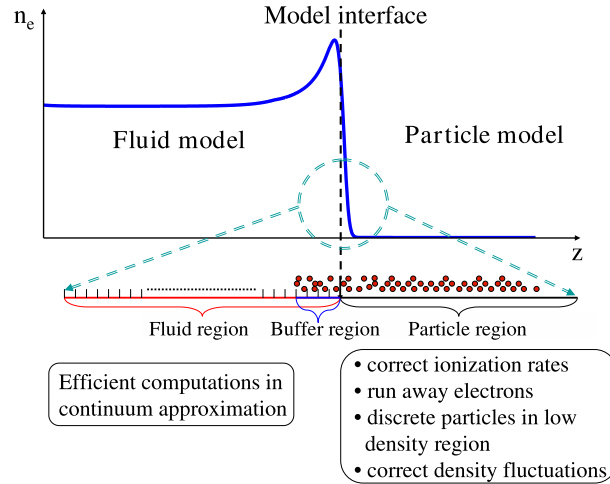
Figure 3.1: *The streamer ionization front, that here is indicated by the electron density $n_e(z)$, and its presentation by particle or fluid model in different spatial regions.*

with increasing electric field. For example, in a field of 200 kV/cm, the ionization level behind the front is 60% higher in the particle model than in the fluid model. We have related this to the fact that the electron energies and, consecutively, the ionization rates in the leading edge of the front are considerably higher in the particle than in the fluid model; they are actually at the edge of runaway. We found that this effect is due to the strong density gradients in the front, and not due to field gradients. So for high fields and consecutively strong density gradients at the streamer tip, there is a clear need for particle simulations, and particles, rather than super-particles, should be used to get physically realistic density fluctuations when modeling, e.g., the branching process of a streamer.

The basic idea of the present paper is demonstrated in Fig. 3.1, namely to follow the single electron dynamics in the high field region of the streamer where the electron density gradient is steep, and to present the interior region with large numbers of slower electrons through a fluid model with appropriate transport coefficients. As in Chap. 2, we study negative streamers in nitrogen, and we simplify the notation by refering to standard temperature and pressure though the model trivially scales with gas density. The particle and the fluid model by themselves are taken as described in detail in Chap. 2. But how should particle and fluid model be coupled in space? And where should the interface between the models be located to get fast, but reliable results? The answers to these questions will be given below. They required us to identify correctly the spatial region where particle and fluid model
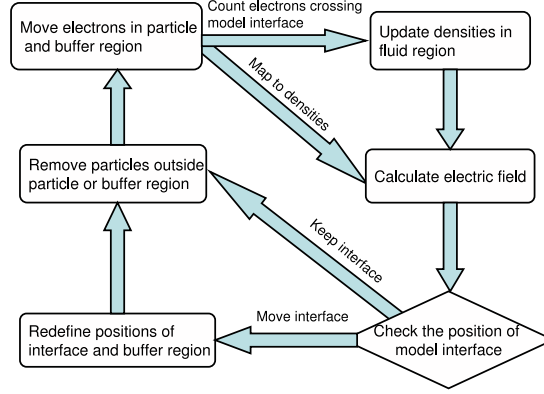
Figure 3.2: *Flow chart for one time step from t_n to t_{n+1} in the complete hybrid calculation.*

deviate, and this allowed us to then compute the full electron physics efficiently in the relevant region.

When coupling the models, the model interface should move with the ionization front; this keeps the total number of electrons limited and super-particles need not be introduced. The position of the interface can be chosen either according to the electron densities or to the electric field. As the electron densities fluctuate stronger than the electric field, we relate the position of the model interface to the electric field. More precisely, the interface is placed where the local field E is a given fraction x of the maximal field E^+: $E_{\text{interface}} = x\, E^+$. By varying x, the region modeled by particles can be varied.

To properly handle the interaction of two models, we introduced a so called "buffer region" where a particle model coexists with a fluid model. The separation of the full computational region into fluid, particle and buffer region is indicated in Fig. 1. Buffer regions have been introduced in [86, 9, 10] for rarefied gases coupling a direct simulation Monte Carlo (DSMC) scheme to the Navier-Stokes equations, and in other applications [63, 6]. Physical observables are evaluated from the fluid model in its whole definition region up to the model interface. Beyond that point, the particle model is used. The particle model extends back beyond the model interface into the buffer region where particle and fluid model coexist; it supplies particle fluxes to the fluid model on the model interface. However, correct particle fluxes require correct particle statistics within the buffer region whose length should be as small as possible to reduce computation costs, but larger than the electron energy relaxation length (see Chap. 2). In many cases, new particles need to be introduced into the buffer region, that have to be drawn from appropriate distributions in con-
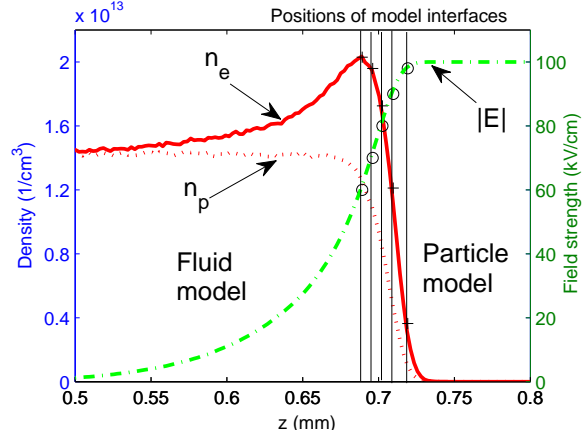
Figure 3.3: *Electron density n_e and ion density n_p (solid and dotted line) and electric field strength $|E|$ (dash-dotted line) in a streamer ionization front in nitrogen in a field of $E^+ = -100$ kV/cm at standard temperature and pressure within a pure particle model. Our units are related to other commonly used units like 1 kV cm^{-1} bar^{-1} = 1.316 V cm^{-1} torr^{-1} = 3.72 Townsend at T=300 K. Below we will model the leading edge of the front by a particle model and the streamer interior by a fluid model where the model interfaces are located at $E_{\text{interface}} = x\ E^+$ with $x = 0.6, 0.7, 0.8, 0.9,$ and 0.98. These interface positions for Figs. 2 and 3 are marked by vertical lines, with "o" for the fields and with "+" for the densities.*

figuration space. This would pose a particular problem since a Boltzmann or even a Druyvesteyn distribution can be inaccurate. But for negative streamers, where electrons on average move somewhat slower than the ionization front, the electron loss at the end of a sufficiently long buffer region does not affect the calculation of particle fluxes at the model interface. Therefore the particle loss at the end of the buffer region can be ignored and new electrons do not need be created artificially.

In more detail, the calculation is performed as follows. One hybrid computation step from t_n to t_{n+1} is described in the flow chart in Fig. 3.2. The electric field E, the electron and ion densities n_e and n_p in the fluid region and the kinetic information of particles in the particle and buffer region are given at time step t_n. First, the positions and velocities of all old and the newly generated particles are updated to time step t_{n+1} in the particle and in the buffer region. Their collisions during this time step are treated stochastically and their new velocities and positions are calculated by solving the equation of motion. The number of electrons crossing the model interface during this time step is recorded. This particle flux across the interface provides the required boundary condition for calculating the evolution

of the densities in the fluid region up to the same time t_{n+1}. The particles are at arbitrary positions, but densities and field are calculated here on the same numerical grid. Therefore the particles in the particle region are averaged to densities on the numerical grid, and then the electric field at time t_{n+1} is calculated from the Poisson equation everywhere. (The charge density in the buffer region is taken from the fluid model, and the particles in the buffer region only serve to generate correct fluxes for the fluid region.) Finally, the position of the model interface is updated to its new position at time t_{n+1}; it can stay where it was or move one grid size forward. The buffer region moves with it. All particles that now are neither in the particle nor in the buffer region, are removed from the particle list.

In the particle model, a standard PIC/MCC (Particle in Cell/Monte Carlo collision) method is implemented. At each time step of length $\Delta t = 0.3$ ps, particles in the particle regions are mapped to densities on a uniform grid with mesh size $\Delta \ell = 2.3$ μm. Meanwhile, the fluid equations are solved in the fluid region of the same grid; discretization and grid dependence of the fluid model are discussed in detail in [163]. The charge density $n_p - n_e$ then can be obtained everywhere and the electric field is calculated on this grid. The size of the time step and the grid size are chosen such that the ionization front need several time steps to move over one $\Delta \ell$, e.g., 10 Δt at 100 kV/cm and 3 Δt at 200 kV/cm.

The length of the buffer region is another crucial factor in the hybrid computation. A buffer region with length of 32 $\Delta \ell$ has been used in the present simulations, which ensure a reliable flux around the model interface and stable results of hybrid simulations. The length of the buffer region is much larger than the energy relaxation length found in Chap. 2. The long buffer region does not bring a heavy burden to the simulation of the planar front system but will considerably reduce the computational efficiency in a more complex geometry. Therefore, the minimal length of the buffer region as well as other features of fluid and particle models shall be investigated in more detail in a future paper.

3.2   Hybrid calculated planar front

We first show the simulation results of this coupled model for a front propagating into a field of $E^+ = -100$ kV/cm, and with the model interface located at $x = 0.6$, 0.9, and 0.98; the positions of these interfaces are indicated in Fig. 3.3. The field ahead of the front is fixed, and the system is always taken long enough that effects at the outer boundaries are not felt. The coupled model generates different electron and ion densities behind the ionization front as shown in Fig. 3.4; for $x = 0.6$, the density is as in the particle model; for $x = 0.98$, it is as in the fluid model; and for
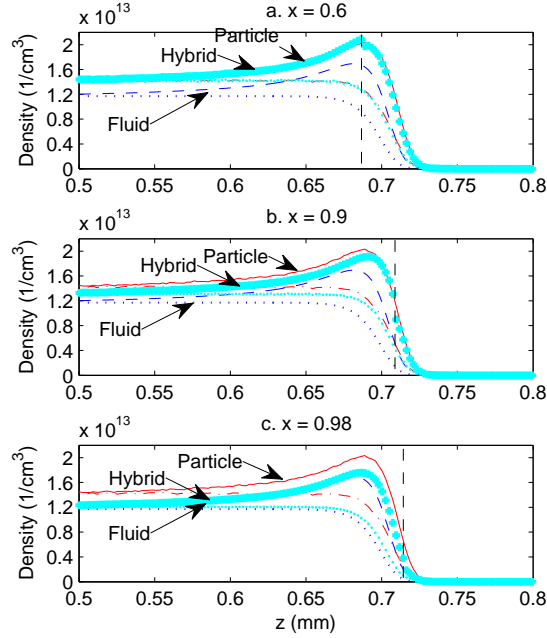
Figure 3.4: *Electron and ion densities in the coupled model (thick lines) in a field of $E^+ = -100$ kV/cm with model interfaces at $E_{\mathrm{interface}} = x \, E^+$ with (a) $x = 0.6$, (b) $x = 0.9$, and (c) $x = 0.98$; these interface positions are indicated by vertical dashed lines. The densities in the particle model (electrons: solid, ions: dot-dashed) and in the fluid model (electrons: dashed, ions: dotted) are shown as well; they are discussed in Chap. 2.*

$x = 0.9$, it takes some intermediate value. We conclude that the solution of the pure particle model can be replaced by the coupled model, if a sufficiently large region of the ionization front with its steep gradients is covered by the particle model, and that the coupling to the fluid model behind that region does not cause numerical artifacts. This confirms the discussion in Chap. 2; it is indeed the high electron density gradient that causes an electron energy overshoot and a higher ionization rate in the leading edge of the particle front. The coupled model also confirms that the field gradients do not play a role in causing the density discrepancy between the fluid and the particle model as the field keeps varying across the model interface in the coupled model.

Having analyzed the ionization front propagating into a field of $E^+ = -100$ kV/cm, we now summarize the results for fields ranging from -50 to -200 kV/cm.
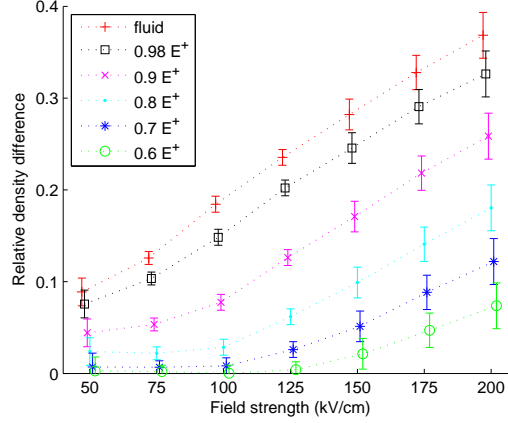
Figure 3.5: *Relative density difference behind the front $(n^-_{e,part} - n^-_{e,coup})/n^-_{e,part}$ between the particle model and the coupled model as a function of the applied electric field E^+ and of the position of the model interface $E_{\mathrm{interface}} = x \cdot E^+$ with $x = 0.6$ (□), 0.7 (x), 0.8 (·), 0.9 (*), 0.98 (o) and 1.0 (+). The last case corresponds to the fluid model. (Note that a density difference of 60% relative to the fluid model corresponds to a density difference of 37.5% relative to the particle model.)*

Fig. 3.5 shows the discrepancy between particle and coupled model on the most sensitive observable (see Chap. 2), namely on the relative difference $\left(n^-_{e,part} - n^-_{e,coup}\right)/n^-_{e,part}$ of the saturated electron density n^-_e behind the ionization front. This quantity is shown as a function of the electric field E^+ and of the position of the model interface parameterized again by x. The figure shows that for higher E^+, the parameter x needs to be smaller. This shift of required interface position relative to E^+ corresponds to a shift of the maximal electron density relative to E: both for $E^+ = -50$ kV/cm and for $E^+ = -200$ kV/cm, the particle and the coupled model agree well, if the model interface lies at the maximum of the electron density and therefore covers the complete steep gradient region; this is the case at $E = 0.8\ E^+$ for $E^+ = -50$ kV/cm and at $E = 0.35\ E^+$ for $E^+ = -200$ kV/cm.

Coupling particle and fluid models in space with varying interface positions confirms our prediction (see Chap. 2) that the density discrepancies between particle and fluid model are due to the strong density gradients in the leading edge of the front. This investigation also lays the basis for constructing a fully 3D coupled particle-fluid model where the fields ahead the ionization front are changing in space and time.

Chapter 4

Spatially hybrid computations for streamers — a thorough analysis in 1D

The inconsistency of the electron flux at the model interface in our first hybrid attempt leads us to an extended fluid model which includes a density gradient expansion term to approximate the nonlocal ionization rate at the ionization front. Compared to the classical fluid model, the extended fluid model not only reduces the density difference between fluid and particle simulation, but also supplies a consistent flux at the model interface in the hybrid computation. Therefore, instead of the classical fluid model, the hybrid model couples the extended fluid model with the particle model. In this chapter, the coupling algorithms and the numerical implementations are given in detail. The important questions arising from the coupling, such as how to apply the two models in suitable regions adaptively and how to ensure a correct interaction between the two models, are also discussed. A set of recommendations is given that can be used directly in the future 3D hybrid simulation.

4.1   Introduction

The classical fluid model for streamers as used by many authors [64, 99, 249, 126, 127, 14, 77, 13, 209, 163, 215, 150] can be derived from the Boltzmann equation with the assumption that the transport and reaction coefficients depend only on local quantities, i.e., on local field and densities. Frequently it is believed that the most crucial assumption is the local field approximation, i.e., the assumption that the electron mobility, diffusion rate and ionization rate are functions only of the local electric field. However, in our article [137] (reproduced in Chap. 2), we have shown that the local field approximation is not problematic as the field varies relatively slowly compared to the mean free path of the electrons. And we have found that strong electron density gradients have to be taken into account. This accounts for the fact that relatively more energetic particles move rapidly and predominantly in the electron drift direction (see Fig. 2.3), and that they are therefore ahead of the less energetic particles. Within the density gradient in the propagating front, there are therefore relatively more energetic electrons. To include this nonlocal effect, the classical fluid model will here be extended by a density gradient expansion in the ionization term.

The spatially hybrid scheme in 1D for planar fronts has been presented in Figure 3.1. The first attempt of coupling is reported in Chap. 3, where the position of the model interface has been briefly discussed. Instead of the classical fluid model, we introduce an extended fluid model to incorporate (approximately) these nonlocal effects. The extended fluid model is compared with the classical fluid model and the particle model both in swarm experiments and for a planar front. After having verified its advantages, we couple this extended fluid model (instead of the classical fluid model) with the particle model.

We have shown in Chap. 3 that at -100 kV/cm, the hybrid model which couples the classical fluid model with the particle model, can generate similar results as the pure particle simulation when the whole density decay region of the ionization front is included in the particle region, and similar results as the fluid model when only the very leading part of the ionization front is included. Compared to the old hybrid simulation, the new hybrid model generates results closer to the pure particle simulation when the same position of the model interface is used.

The essential problems in coupling; namely i) where to put the model interface and ii) how to realize a reasonable interaction between the two models, are investigated for a range of electric fields. the position of the model interface varies at the ionization front in the hybrid model, The relative density differences between the pure particle simulation and the hybrid simulation are evaluated depending on the position of the model interface in the hybrid model. To obtain a stable interaction

between two models in a hybrid computation, different lengths of the buffer region have been tested. The position of the model interface and the length of the buffer region have been studied for a range of electric fields, which gives a reference for the 3D coupling where fields ahead of the ionization front vary in time and space.

4.2 The extended fluid model

Here we will first have a look at swarm experiments both in the particle and in the classical fluid model and explain why we need the extension. Then we present the equations of the extended fluid model. The definitions of transport coefficients are reviewed and discussed for both the classical fluid model and the extended fluid model. We compare the extended fluid model with the particle model in both the swarm experiment and the planar front. Finally we discuss the limitations of the extended fluid model.

4.2.1 Why the fluid model needs an extension

Discontinuities in the hybrid model described in Chap. 3

We have shown first results of a hybrid computation which couples the classical fluid model with the particle model in chapter 3. To ensure a stable and correct interaction between the two models, we investigated the electron flux densities on the model interface, and the mean electron energies and velocities around the model interface.

However, we found a disagreement of the local electron flux between the two models. When the particle and the classical fluid model are applied in the same region of the ionization front, the mean electron flux density is lower in the particle simulation than in the classical fluid simulation. If one puts the model interface near the maximum of the electron density, a density jump can appear near the model interface. This is shown in Fig. 4.1 where the model interface is at $E = -60 \, \text{kV/cm}$ with the field ahead of the front being $E^+ = -100 \, \text{kV/cm}$; here the local fluxes differ at both sides of the model interface, and this results in the visible density jump. The numerical discretization and other details of this experiment can be found in Chap. 3.

The effect appears although the transport coefficients generated in the particle swarm experiments were used in the fluid model, and the two models therefore should be consistent. To understand the underlying problem, we review the conceptual differences between the two models and compare them in a swarm experiment.
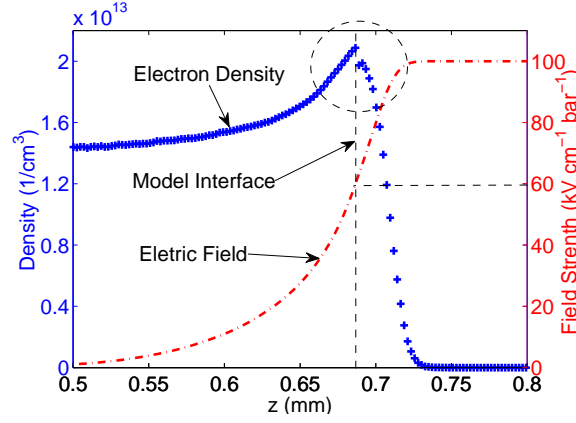
Figure 4.1: *Hybrid simulation of a planar front propagating in $E^+ = -100$ kV/cm with the model interface at -60 kV/cm with the method described in Chap. 3. Electron density ("+") and electric field (dot-dashed line) are plotted.*
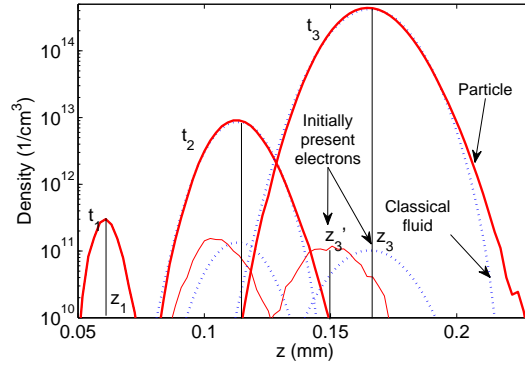
Figure 4.2: *Evolution of electron swarms at three consecutive time steps t_1, t_2, t_3 in a field of -100 kV/cm, where t_1, t_2, and t_3 are 20, 130, 240 ps when the simulation starts from 100 pairs of electrons and ions. Shown are the spatial profiles of the total swarm in the 1D particle model (solid line) and in the 1D classical fluid model (dotted line). Also shown are the spatial profiles of those electrons that were already present at time t_1 (at the same three time steps).*

Swarm simulations in particle and fluid model - a reinvestigation

Fig. 4.2 shows simulated electron swarms propagating in a uniform constant field of -100 kV/cm. The simulations have been carried out both with the particle model

(solid lines) and with the classical fluid model (dotted lines) in 1D starting from the same initial conditions.

Here and in all later comparisons of particle or fluid results, the initial distributions of electrons and ions is generated in the following manner. An electrically neutral group of 100 electrons and ions is inserted at one point in space. Their temporal evolution is calculated with the particle model. After a short time that depends on the electric field, e.g., after $t_1 = 20$ ps in a field of 100 kV/cm, a small swarm forms in which the electron density profile is well approximated by a Gaussian distribution. This distribution of electrons and ions is used as an initial condition for all simulations, particle and fluid.

In the particle model, the standard Monte Carlo technique in a constant electric field is applied. For the fluid model, the equations of the particle densities are discretized in space with a finite volume method. The particle densities are updated in time using a third order upwind-biased advection scheme combined with a two-stage Runge-Kutta method. The same time step and cell size were used in the particle and the classical fluid calculation, i.e., $\Delta t = 0.3$ ps and $\Delta z = 2.3$ μm. More details of the numerical implementation of particle and fluid model can be found in Sect. 2.2.1.

In the swarm experiment, we let both the particle model and the classical fluid model follow the swarm from $t_1 = 20$ ps to $t_3 = 240$ ps, and the electrons in the particle simulation are mapped to densities on the same grid as used in the fluid simulation. During the simulation, we follow the growth of the swarm of electrons, and pay specially attention to the group of electrons which are initially (at time t_1) present as seed electrons. In Fig. 4.2, we show the electron density profiles of the swarm at t_1 and at the later stages t_2 and t_3, and we also show the density distributions of those electrons existing at time t_1, at all three time steps t_1, t_2 and t_3, neglecting all electrons generated later. These distributions directly show the true electron mobility.

Fig. 4.2 shows that the profiles of the total swarm are nearly the same in the classical fluid model and in the particle model. This was to be expected as we just derived the transport and reaction coefficients μ, $\mathbf{D}$, and α for the fluid model through this condition in Sect. 2.2.3; these coefficients from here on will be referred to as μ_l, $\mathbf{D}_l$, and α_l (where the lower index l refers to the local model).

However, when we average the local electron flux $\mathbf{j}_e$ over the simulation domain and over a short time interval τ, we find a higher mean flux density per electron

$$\frac{\bar{\mathbf{j}}_e}{N_e} = \int_t^{t+\tau} \frac{dt}{\tau} \int_V dV \, \frac{\mathbf{j}_e}{N_e} \tag{4.1}$$

in the fluid than in the particle swarm simulation (here V is the volume of the sim-

ulation domain and N_e is the number of electrons). The mean flux density per electron equals the mean electron drift $\mu\mathbf{E}$, as the diffusive flux vanishes if all electrons are inside the integration volume, see Eq. (4.5). These different fluxes at the model interface of the hybrid streamer simulation are therefore consistent with the different fluxes in the swarm experiment in fluid or particle simulation.

Another closely related observation in Fig. 4.2 is that the swarms grow in different ways in particle and fluid simulations. In the fluid simulation, the electron swarm grows homogeneously, i.e., the center of mass of the initially present electrons moves with the same speed as the center of the mass of total electron swarm. However, in the particle simulation the mean displacement of the whole swarm is larger than that of the initially present particles. This shows that the classical fluid model is based on approximations that here become inaccurate.

Discussion: validity of the local density approximation

The two discrepancies between particle and fluid swarms, namely in the mean flux density (4.1) and in the swarm growth characteristics (Fig. 4.2), are actually due to the same reason: the local density approximation. As the electric field is constant in the swarm experiment, it cannot be the local field approximation. In Chap. 2, it was already shown that the local electron energy distribution depends on the local electron density gradients both in planar fronts and in swarm experiments. It indicates that even in a uniform constant field, the ionization rates increase from the tail to the head of the electron swarm. Therefore there are two contributions to the speed of the swarm: i) the electron drift in the local field as a main contribution and ii) the unequal growth of the swarm due to the unequal electron energy distribution.

The classical fluid model assumes that the local mean energies and local mean reaction rates are functions of the reduced electric field and ignores the fact that within the same electric field, the ionization rate can be different. At the front of the swarm, this leads to a lower reaction rate in the fluid simulation than in the particle model. But by overestimating the ionization rate at the tail, the swarm in the classical fluid model generates the same amount of electrons as in the particle swarm. And by overestimating the mobility of electrons, the swarm nevertheless propagates with the same speed. Or in another words, the classical fluid model approximates the swarm density profile rather well, but at the price of wrong local fluxes and wrong local reaction rates. In simulations with non-uniform fields, such as streamers in which the density profiles are determined only by the front while the tail doesn't play a role in the propagation at all, the classical fluid model pays the price with a lower density than in the particle model.

Therefore the fluid model has to be extended to include the non-homogeneous

ionization rate under non-uniform electron density conditions. And by introducing a nonlocal term, we expect the fluid model to supply the same electron flux as the particle model within the same field.

4.2.2 Gradient expansion and extended fluid model

The electron ionization rates for non-uniform fields and electron densities are discussed in [8, 173]. There perturbation theory is used to obtain the rate coefficients, and it is shown that they can be represented by a gradient expansion about the local values

$$k = k_0[1 + k_1 e \nabla \ln n_e + k_2 N/E \nabla \cdot (\mathbf{E}/N) + k_3 e \nabla \ln(E/N)], \qquad (4.2)$$

where n_e is the electron density, $\mathbf{E}$ and E are the field and the field strength, N is the molecule density of the background gas, k is the ionization rate and k_0, k_1, k_2, k_3 are parameters depending on E/N that have to be determined.

In our previous studies [137, 139] reproduced in Chapters 2 and 3 and in the previous section 4.2.1, we have shown that the local density approximation is insufficient while the local field approximation is not problematic. Therefore, we neglect the field gradient terms and focus on the density gradient in Eq. (4.2).

Our extended fluid model contains two continuity equations for electron and ion densities

$$\frac{\partial n_e}{\partial t} + \nabla \cdot \mathbf{j}_e = \mathcal{S}, \qquad (4.3)$$

$$\frac{\partial n_p}{\partial t} = \mathcal{S}, \qquad (4.4)$$

$$\mathbf{j}_e = -\mu_n(\mathbf{E})\mathbf{E}n_e - \mathbf{D}_n(\mathbf{E})\nabla n_e, \qquad (4.5)$$

where n_e and n_p are electron and ion density, respectively, $\mathbf{j}_e$ is the electron flux and $\mathcal{S}$ is the source of electrons due to impact ionization, μ_n represents the mobility and $\mathbf{D}_n$ is the diffusion matrix (The subscript "n" stands for "nonlocal", which will be further explained in Sect. 4.2.3). The densities are coupled to the Poisson equation for the electric field

$$\nabla \cdot \mathbf{E} = \frac{e\,(n_p - n_e)}{\epsilon_0}. \qquad (4.6)$$

The difference to the classical fluid model is that the source term now contains a density gradient expansion term

$$\mathcal{S} = |n_e\,\mu_n(E)\,\mathbf{E}|\,\alpha_n(E)(1 + k_1(E)e\nabla \ln n_e), \qquad (4.7)$$

where the function $k_1(E)$ and other transport and reaction rates will be determined in the next section.

4.2.3   Transport coefficients and ionization rate

The consistency of the fluid model with swarm results has been known to be an important issue for a long time. Robson *et al.* [208] recently discussed this issue and emphasized that the consistency requirement actually applies to the transport coefficients and reaction rates. In Chap. 2, we have achieved optimal consistency between particle and fluid model by determining the transport coefficients $\mu(E)$, matrix $\mathbf{D}(E)$, and ionization rate $\alpha(E)$ from the particle swarm experiments.

Electron mobility μ

When the classical fluid model is extended with a density gradient term, the transport and ionization coefficients may also change, and these coefficients should be redefined in the swarm experiments. For instance, the mobilities can be determined from the mean displacement of electron swarms in a uniform constant field, but through two different definitions: i) by mean displacement of the swarm and ii) by mean displacement of the initially present particles. The second definition represents the real motion of electrons while the first definition actually is the sum of the local electron fluxes under the influence of the electric field plus the nonlocal growth of the swarm. Averaging the local flux rate as in (4.1) to obtain the electron mobilities gives essentially the same result as the second definition.

The difference between the two definitions of the mobility are illustrated in Fig. 4.2. The mobility is either defined as

$$\mu_l(E)E = \frac{z_3 - z_1}{t_3 - t_1}$$

or as

$$\mu_n(E)E = \frac{z_3' - z_1}{t_3 - t_1},$$

where z_1 and z_3 are the centers of mass of the swarms at times t_1 and t_3, and z_3' is the center of mass of those electrons at time t_3 that were also present at time t_1. These mobilities μ_l or μ_n are presented in Fig. 4.3. Here μ_l is the electron mobility in the classical fluid model and μ_n is the one in the extended fluid model. They are almost the same for fields E below 30 kV/cm when impact ionization is small or even completely negligible, but the difference increases as the field strength increases.

It can be noted that the curves in Fig. 4.3 are not completely smooth. This is due to stochastic fluctuations within the Monte Carlo simulations. However, it has been checked that these small fluctuations have a negligible influence on the final results.
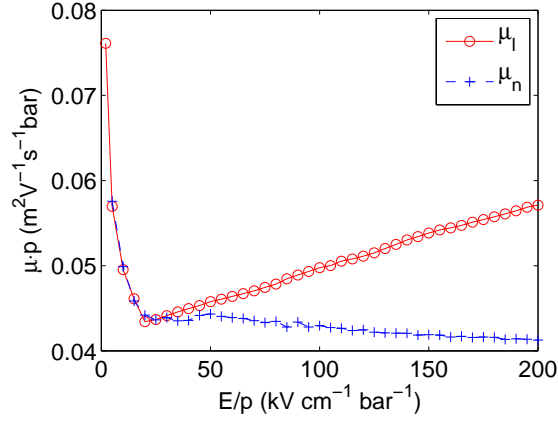
Figure 4.3: μ_l and μ_n as functions of the electric field strength E.

Impact ionization rate α

The reaction rate is derived from the growth rate of the total electron number $N_e(t)$ in the swarm in a particle simulation. Within a time t, the swarm propagates a distance $\mu(E)Et$, and the reaction rate is determined by

$$\alpha(E) = \frac{\ln N_e(t_2) - \ln N_e(t_1)}{\mu(E)E\,(t_2 - t_1)}. \tag{4.8}$$

When μ_n is used instead of μ_l, the ionization rate changes correspondingly from α_l to

$$\alpha_n(E) = \alpha_l(E)\,\frac{\mu_l(E)}{\mu_n(E)} \tag{4.9}$$

as the simulation fixes the product $\mu_l\alpha_l = \mu_n\alpha_n$.

Diffusion tensor D

The diffusion rates can also be obtained according to two different definitions: the diffusion of the electron swarms $\mathbf{D}_l$ or diffusion of the initially present electrons $\mathbf{D}_n$. The results turn out the same

$$\mathbf{D}_l(\mathbf{E}) = \mathbf{D}_n(\mathbf{E}). \tag{4.10}$$
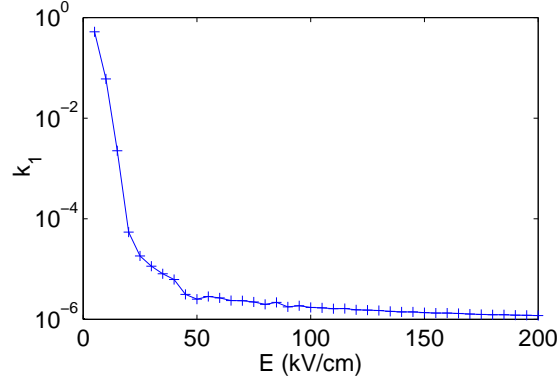
Figure 4.4: *The parameter function k_1 as a function of the electric field.*

The parameter function k_1 of the gradient expansion

In the extended fluid model, the function k_1 in Eq. (4.7) has to be found. The rates k_1, k_2, and k_3 in Eq. (4.2) were calculated by Aleksandrov and Kochetov [8] by solving the Boltzmann equation in a two-term approximation. But to stay consistent with the approach above, all parameter functions in the fluid model are derived from the particle swarm simulations. Since we neglect the field gradient term in the source term, only the k_1 needs to be calculated.

In fact, k_1 can be calculated by simply comparing Eqs. (2.7) and (4.3) for the classical and the extended fluid model. As both fluid models can properly describe the swarm when appropriate parameters are applied, we have

$$\nabla \mu_l(\mathbf{E})\mathbf{E}n_e + \nabla \mathbf{D}_l(\mathbf{E})\nabla n_e + |n_e\ \mu_l(E)\ \mathbf{E}|\ \alpha_l(E)$$
$$= \nabla \mu_n(\mathbf{E})\mathbf{E}n_e + \nabla \mathbf{D}_n(\mathbf{E})\nabla n_e + |n_e\ \mu_n(E)\ \mathbf{E}|\ \alpha_n(E) + k_1(E)\mu_n(E)\mathbf{E}\alpha_n(E)\nabla n_e.$$

In a constant uniform electric field such as in the swarm experiment, $\mu_l(E)$, $\mu_n(E)$ and E are constant and $\nabla \mu_l(\mathbf{E})\mathbf{E}n_e = \mu_l(\mathbf{E})\mathbf{E}\nabla n_e$. Removing identical terms on both sides of the equation, we get $\mu_l(E) = \mu_n(E)(1 + k_1(E)\alpha_n(E))$ or

$$k_1(E) = \frac{\mu_l(E) - \mu_n(E)}{\alpha_n(E)\ \mu_n(E)} \tag{4.11}$$

where μ_l, μ_n and α_n were derived above from the particle swarm experiments. k_1 as a function of the field is shown in Fig 4.4.
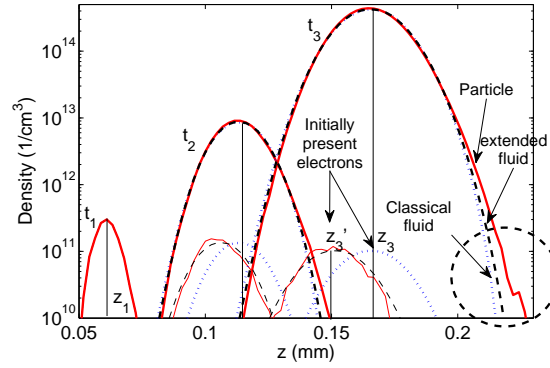
Figure 4.5: *The density profiles of electron swarms and the initial electrons in a field of* $-100\ kV/cm$ *are shown at times* t_1, t_2 *and* t_3. *The plot is the same as in Fig. 4.2, but now the extended fluid simulation is added as a dashed line.*

4.2.4 Comparison of the extended fluid model with the particle model

Now the stage is set to compare the extended fluid model with the particle model both in swarms and in planar ionization fronts. The extended fluid equations are discretized in the same manner as the classical fluid model, and the particle densities are updated with the same scheme as before (see Chap. 2). The same time step and cell size are used in the extended fluid calculation as in the particle and the classical fluid calculation (see Sect. 4.2.1).

Swarm simulations

In Fig 4.5, we show electron swarms at times t_1, t_2, and t_3 in a constant field of $-100\,\text{kV/cm}$; the swarms were followed by particle simulation (solid line), classical fluid simulation (dotted line) and extended fluid simulation (dashed line). For the whole swarm, all three models give similar results, but the extended fluid model follows the evolution of the initially present electrons much better than the classical fluid model.

However, the figure also shows that in the leading edge of the swarm (marked with a large dashed circle) neither the extended fluid model nor the classical fluid model describe the electron density distribution of the particle model precisely. As described in Chapter 2, individual electrons with high energies dominate this region, and neither the fluid models nor any other macroscopic approach can de-
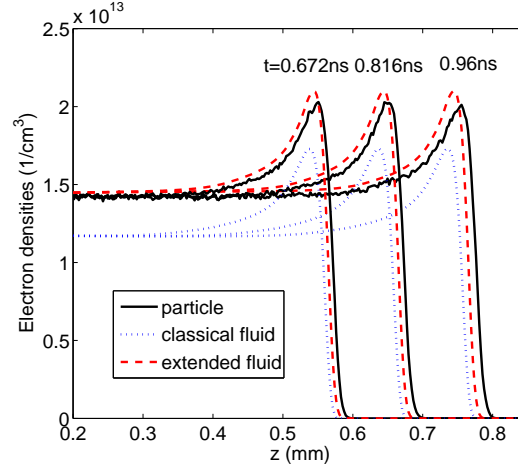
Figure 4.6: *Temporal evolution of the electron densities in a planar front in a field of $E^+ = -100 \ kV/cm$. Shown are the spatial profiles of electron densities derived with the particle, classical fluid or the extended fluid model at time levels t=0.672 ns, 0.816 ns and 0.96 ns (particle simulation: solid line, fluid simulation: dotted line, and extended fluid simulation: dashed line).*

scribe this microscopic behavior. The densities in this region are 3 to 5 orders lower than the maximum density. But as streamer ionization fronts are so-called "pulled" fronts, the behavior in the leading edge of the front actually determines the front velocity. From this point of view, the hybrid model that uses the particle model in the leading edge of the ionization front, is the method of choice.

Front simulations

Fig. 4.6 shows the temporal evolution of the planar front in a field of $E^+ = -100$ kV/cm in the particle simulation (solid line), classical fluid simulation (dotted line), and extended fluid simulation (dashed line). Compared to the classical fluid model, where the maximal electron density in the front and the saturation level of the ionization behind the front are about 20% lower than in the particle model, the densities in the extended fluid model are much closer to the particle model. The particle and fluid front move with approximately the same velocity, but the particle front moves slightly faster than the extended fluid front, and the extended fluid front moves slightly faster than the classical fluid front, in agreement with Fig. 4.5. (We recall from Chapter 2 that the leading edge of a swarm and of a pulled front in the same
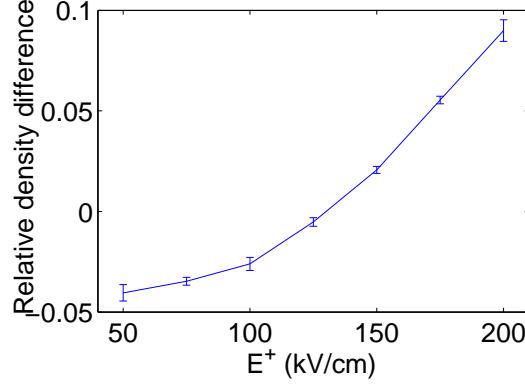
Figure 4.7: *The relative density difference (4.12) of extended fluid model and particle model.*

field have the same spatial profile and create the same velocity.)

Having analyzed planar fronts at -100 kV/cm, we now summarize the front results for fields ranging from -50 to -200 kV/cm in Fig. 4.7. The figure shows the relative difference

$$\frac{n_{e,part}^- - n_{e,e.fluid}^-}{n_{e,part}^-}. \tag{4.12}$$

of the saturated electron density behind the front in the particle model ($n_{e,part}^-$) and the extended fluid model ($n_{e,e.fluid}^-$). Compared to the relative difference between the particle model and the classical fluid model discussed in Chap. 2, which increases from 10% at 50 kV/cm to 40% at 200 kV/cm, we now find that the relative density difference in the extended fluid model never exceeds 10% within this range of fields.

4.2.5 The drawbacks of the extended fluid model

By approximating the nonlocal ionization rate by a density gradient expansion, the extended fluid model reproduces the ionization level behind the front much better than the classical fluid model. However, Fig. 4.7 shows that this ionization level in the extended fluid model exceeds the one in the particle model when the field E is below 125 kV/cm. This will not harm its coupling with the particle model, but the reason for this unexpected behavior is briefly discussed here, because it could lead to further improvements of the fluid model.

Several possible reasons have been examined, for example, the quality of the parameters (μ, $\mathbf{D}$, α and k_1) used in the extended fluid model, the discretization of the gradient expansion term, and the relative ionization rate in the very leading
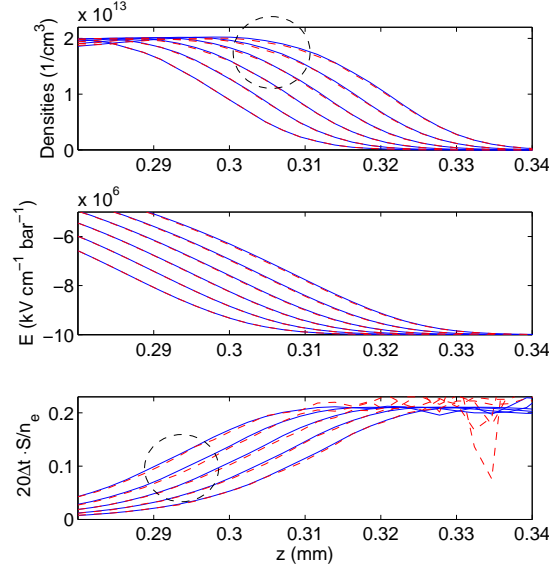
Figure 4.8: *The ionization front propagates into -100 kV/cm in both particle model (dashed) and extend fluid model (solid). The two simulations start from the same front which is pre-produced by a particle simulation, and follow the front propagation for 100 Δt where $\Delta t = 0.3$ ps. We present the electron density (first panel), the electric field (second panel), and the ionization rate (third panel) in time steps of 20 Δt.*

edge where the electron density simply vanishes in the particle model, but remains nonzero in the fluid model due to electron diffusion. The answer was found by comparing the ionization rates within the front between both models.

The simulation is done as follows. We first let the particle model follow the evolution of an ionization front until it is fairly smooth. This creates an initial condition that now is run further both with the extended fluid model and with the particle model. The two models are followed for a time of 100 Δt where $\Delta t = 0.3$ ps in a field of $E^+ = -100$ kV/cm. The result is shown in Fig. 4.8. In the first panel we plot the electron density profile in steps of 20 Δt in the particle model (dashed) and in the extended fluid model (solid). Of course, the curves are identical initially, and a difference builds up in time in the high density region of the front (marked with a dashed circle). In the second panel, we show the electric field which does not vary much between the two models during 100 Δt. In the third panel, we show the relative growth of the ion density $\partial_t n_p / n_e$ integrated over a time of 20 Δt, which is

identical to the local ionization rate S/n_e within this time according to Eq. (4.4). The figure shows that the ionization rate is slightly higher in the extended fluid model in the region of large n_e (marked with dashed circle), and lower in the region of small n_e. Note that these differences appear while the electric fields are the same.

The analysis shows that the extended fluid model does not completely reproduce the particle model. This is understandable. The actual ionization rates S/n_e depend on the energy distribution of the local electrons. The gradient expansion in the ionization rate relates this energy distribution to the local field and to the electron density gradient. The single adjustable function $k_1(E)$ in this gradient expansion is chosen in such a way that an electron swarm in this field is well fitted. But an electron swarm has a characteristic profile in a given field. Regions inside the front might combine a given field with a different density gradient for which the model has not been adjusted. The solution would be to allow for more adjustable functions inside the fluid model by expanding in higher order gradients, or to allow the local ionization rate to depend on the local mean electron energy or even more characteristics of the electron energy distribution. This would require us to calculate these energies. In the end, only a fluid model with infinitely many adjustable functions would appropriately describe the averaged behavior of the particle model. We therefore conclude that the density gradient expansion is a substantial improvement of the fluid model, but that it does not contain the full physics of the particle model. We therefore now proceed to the hybrid model where the extended fluid model will be used only in the less critical inner region of the streamer.

4.3   The hybrid model

Our goal is to build a fully 3D hybrid model for streamer channels, which couples the particle model with the extended fluid model in space as shown in Fig. 3.1. With the experiments carried out for planar fronts, we would like to test our hybrid concept, and find out how to apply the different models in suitable regions adaptively and how to realize a reasonable coupling of those models. Since most of the electrons will be approximated as densities in the hybrid simulation, the problem of the enormous number of electrons in a 3D particle streamer simulation can be reduced. Following the particles can still be a heavy burden for a hybrid model. Therefore the hybrid simulation will let the fluid model approximate most of the electrons as densities and leave as few electrons as possible for the particle model, under the constraint of producing similar results as the pure particle simulation.

In this section, we present the algorithm for the 1D hybrid calculation and discuss the numerical details. Two important issues of the 1D coupling are discussed

in detail: where particle and fluid model are to be applied, and how they should interact with each other.

4.3.1   The hybrid algorithm

In our hybrid model, the particle model is used in the leading part of the ionization front and the fluid model in the rest of the domain. Between them, we have a model interface. The position of the model interface can be chosen either according to the electron densities or according to the electric field. This means that the model interface is either located at some electron density level $n_e = x\, n_{e,max}$ ahead of the electron density peak $n_{e,max}$, or at some electric field level $E = y\, E^+$ where E^+ is the electric field ahead the front. In both cases, the real numbers $x,\ y$ have to be chosen appropriately within the interval $[0, 1]$. We discuss this choice and the corresponding position of the model interface in detail in Sect. 4.3.3.

Suppose that the position of the model interface is located somewhere as shown in Fig. 3.1. As the streamer propagates forward, because the electric field moves with the front, the model interface moves with the ionization front because we keep it at $n_e = x\, n_{e,max}$ or $E = y\, E^+$. In this way, the particle model at any moment of the simulation follows only a limited number of electrons in the low density region of the ionization front. Because the computational costs of the fluid model are small compared to the particle model, it is clear from Fig. 3.1 that we gain much efficiency in the hybrid model as compared to a pure particle simulation.

The actual gain due to the hybrid method will be even more pronounced in the case of fully three dimensional simulations. With this moving model interface algorithm, the hybrid model may simulate the full streamer dynamics in 3D without using super-particles while remaining computationally efficient.

Once the position of the model interface is set, the interaction of the two models around the model interface needs to be established. To simulate the electron flux crossing the interface between the two models, we introduced a so called "buffer region" which is created by extending the particle region one or a few cells into the fluid region. It has been used in [86, 9, 10] for rarefied gases by coupling a direct simulation Monte Carlo (DSMC) scheme to the Navier-Stokes equations, and for other applications [63, 6] as well. The buffer region helps to build a pure particle description around the model interface, such that the local particle flux in this region can be obtained as in a pure particle simulation. The particle flux across the model interface influences the total number of particles in the particle model, and it will lead to a corresponding increase or decrease of the density in the fluid model.

In this way, around the area where the two models are coupled, the electron flux in a pure particle simulation is maintained in the hybrid computation, while global
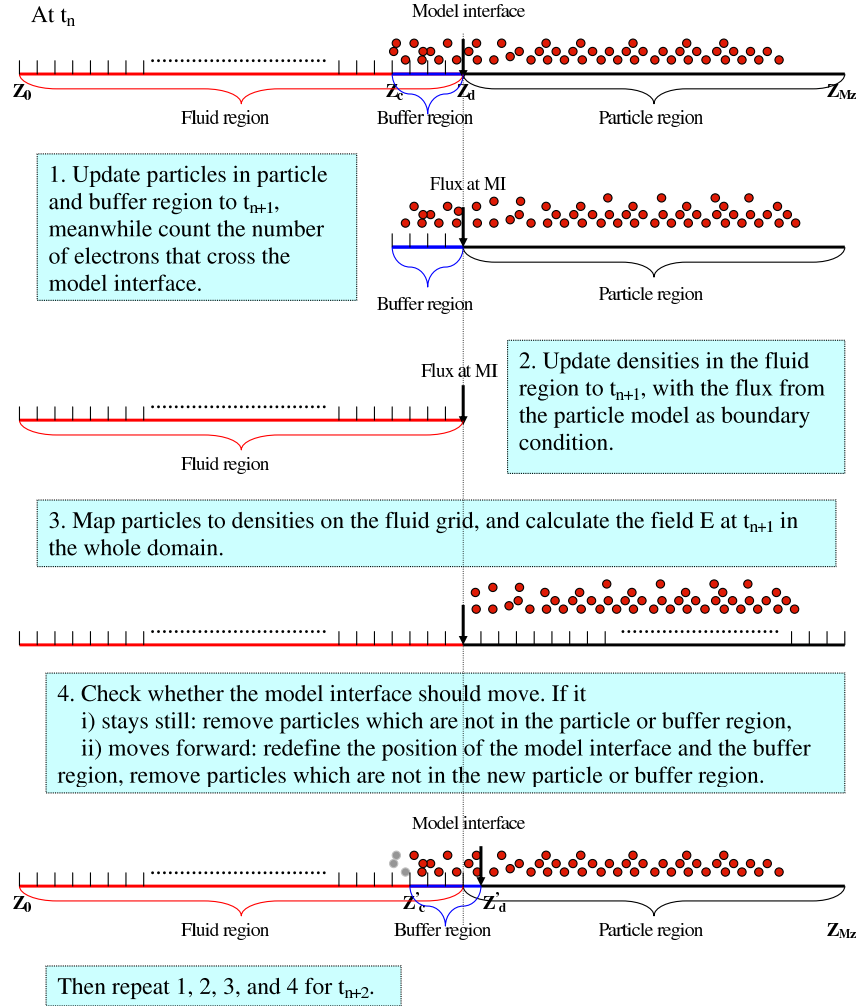
Figure 4.9: *The flow chart of one hybrid computational step from t_n to t_{n+1}.*

mass conservation holds. However, to obtain an accurate flux at this interface, the electrons in the buffer region near the interface should maintain a correct density profile and velocity distribution. In many cases [86, 9, 10] the buffer region or a part of the buffer region at each time step have to be refilled or reconstructed with a large number of electrons with artificial distributions in energy and space. Such a filling or reconstruction on the one hand ensures a stable flux at the model interface, but

on the other hand, it can create non-physical artifacts, which might cause wrong results. In our approach, the generation of electrons from a kinetic prediction can be avoided. The details are presented in Sect. 4.3.4.

Fig. 4.9 shows the flow chart of the hybrid computations. At the beginning of each time step, the particle density is known in the fluid region and the individual particle information is known in the particle region and the buffer region. To update them to the next time step, we first move the particles in the particle and buffer region one step further. The number of electrons crossing the model interface is recorded during the updating. This counted flux is used as a boundary condition to update the densities in the fluid region. To calculate the electric field, the particles in the particle region are mapped to the fluid grid as densities. In the end, we check whether the model interface has to be moved. A more detailed explanation is given in the following section.

4.3.2   Numerical implementation

In the particle model, the positions and the velocities of the electrons are updated with the leap-frog method. The electric field is solved on a uniform grid G (the fluid equations are discretized on the same grid) with cells

$$C_i = \left[z_i - \frac{1}{2}\Delta z, z_i + \frac{1}{2}\Delta z \right], \ i = 1, 2, \cdots M_z, \tag{4.13}$$

where M_z are the number of grid points with cell centers at $z_i = (i - 1/2)\Delta z$ in the z direction, and Δz is the cell size.

The simulation begins with a few electron and ion pairs with a Gaussian density distribution. These initial particles are followed only by the particle model in the beginning of the simulation. As new electrons are generated, the number of particles eventually reaches a given threshold, after which the simulation switches to the hybrid approach. If the computation time is not a concern, the threshold number can be set as the maximum allowed by a real particle simulation. The threshold in our simulation is normally set to be several million electrons to ensure a satisfactory statistics. With proper transversal area A of the system, the simulation with such number of electrons is already in the streamer stage, which means that a steady moving ionization front has been developed and the charge layer at the streamer head totally screens the field inside the channel. In Table 4.1, we summarized the transversal areas ($l_r \times l_r$) and the length of the system in front propagation direction l_z for varying fields, and we also list threshold numbers N_T and the time (T_T) for the particle simulation generating N_T electrons when starting from 100 pairs of electrons and ions.

E (kV/cm)	50	75	100	125	150	175	200
l_r (μm)	55.2	41.4	27.6	23	18.4	13.8	9.2
l_z (mm)	6.9	3.45	2.76	2.3	1.84	1.38	1.15
N_T (10^6)	3	3.2	3.5	3.8	4	5	7
T_T (ns)	$\sim$6.6	$\sim$1.2	$\sim$0.3	$\sim$0.18	$\sim$0.15	$\sim$0.12	$\sim$0.12

Table 4.1: *List of the transversal length l_r (the transversal area is $l_r \times l_r$), the longitudinal length of the system l_z, the threshold number N_T, and the time T_T for the particle simulation generating N_T electrons for a number of electric fields.*

For the transfer from particle to hybrid simulation, we first determine the position of the model interface and the length of the buffer region, which depends on the field ahead of the ionization front as we will see later. Suppose the model interface is chosen at $z_d = d * \Delta z$ and the buffer region is on the interval $[z_c, z_d]$ as shown in Fig. 4.9, where $c, d \in \{1, 2, \cdots, M_z\}$ and $c \leq d$. The particles in the fluid region in the interval $[z_0, z_d]$ are then averaged to the densities on the grid G, while the particles outside the particle region and buffer region on the interval $[z_0, z_c]$ are removed from the particle list. Note that in the buffer region $[z_c, z_d]$, the electron and ion densities are calculated on the underlying continuum grid while the spatial and kinetic information of the individual particles is also maintained.

At the beginning of a time step lasting from t_n to t_{n+1}, we have the electric field $\mathbf{E}_n$, the electron and ion densities n_e, n_p in the fluid region and the positions of the particles in the particle and buffer region at time t_n, and the velocities of these particles at time $t_{n+1/2}$ (since with the leap-frog algorithm, in the beginning of the time step, the positions $\mathbf{x}$ are known at t_n and the velocities $\mathbf{v}$ at $t_{n+1/2}$). In step 1 (as shown in Fig. 4.9), the particles in the particle region and the buffer region are first moved to t_{n+1} taking the stochastic collisions into account through the Monte Carlo algorithm. While updating the particle positions, the number of electrons crossing the model interface is recorded.

Once all particle positions are updated to the next time step, in step 2 we also update the densities in the fluid model. The continuum equations for the particle densities are discretized with a finite volume method, based on mass balances for all cells in the fluid region on the grid G. Eq. (4.5) is used to compute the density fluxes on the face of each cell in the fluid region, except the one at the model interface z_d where the flux from the particle model is used. The ionization rate can be calculated with Eq. (4.7). Given the fluxes on the cell faces and the ionization rate, particle densities at each cell in the fluid region can be updated to the next step using Eq. (4.3) and Eq. (4.4). Since updating the fluid densities needs the particle flux across the model interface as an input for the boundary condition, the two-stage Runge-Kutta method is replaced by the simpler forward Euler method, but with small enough

time step. The densities are calculated using the third order upwind-biased advection scheme. For computations with large time step Δt, the two-stage Runge-Kutta method could be used with the given particle flux (which is an average flux over $[t_n,\ t_{n+1}]$), but this will require two updates of the fluid densities and electric fields per time step.

Now both the particle positions and the densities are known in the respective regions at time t_{n+1}. In step 3, the densities in the particle region $[z_d,\ z_{M_z}]$ are obtained by mapping particles to the grid G. How this is done, is discussed further below. The particle densities are then known everywhere on the grid G and the electric field E_z at time t_{n+1} can be calculated.

In step 4, the position of the model interface is determined either from the particle density or from the electric field criterion. While the density profile and the electric field are updated from t_n to t_{n+1}, the model interface may have to move one cell forward or to stay still. To compare with results of other models, time step and grid size are chosen in the same way as before, i.e., as $\Delta z = 2.3\,\mu$m and $\Delta t = 0.3$ps. With $E^+ = -50$ to -200 kV/cm, the ionization front needs about 30 to 3 time steps to cross one cell. That is, the model interface will on average stay at one cell face for 3 to 30 time steps before it moves to the next cell face. If it stays still, the particles which fly out of the particle and buffer regions are removed from the particle list. If the model interface moves one cell forward, the fluid region is extended one cell into the particle region. Meanwhile, the buffer region also moves one cell forward and the region from z_c to z_c' becomes part of the fluid region, and particles there will be removed from the particle list.

Finally we use E_z at t_{n+1} to update the electron velocities inside the particle and buffer region to $t_{n+3/2}$. This finishes one hybrid time step.

We would like to remark here that one should be careful about the technique of mapping the particles to the densities in the particle region. One can use zero-order weighting by simply counting the number of particles within one cell, or first-order weighting (PIC), which linearly interpolates charges to the neighboring cells, or some higher-order weighting techniques like quadratic or cubic splines. The particle model has been tested with various sizes of time steps and cell sizes. The numerical discretization errors converge to zero as time step and cell size decrease when using either the zero-order weighting or the first-order weighting, but the convergence was faster with first-order weighting. The first-order mapping is the most used technique in particle simulations for plasmas because: "As a cloud moves through the grid, the first-order weighting contributes to density much more smoothly than zero-order weighting; hence, the resultant plasma density and field will have much less noise and be more acceptable for most plasma simulation problems." [24]. However, in the hybrid computation, the zero-order weighting guarantees total charge

Old hybrid model · New hybrid model
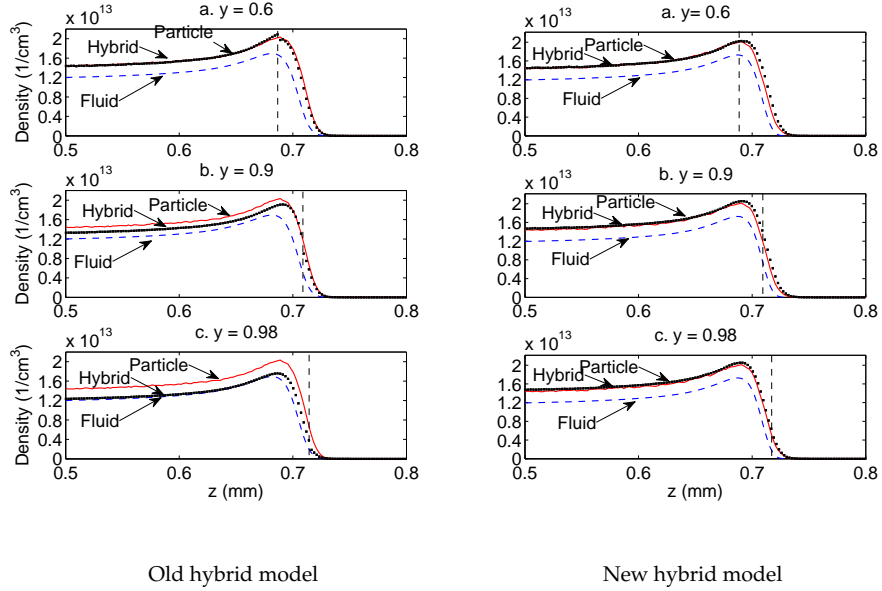
Figure 4.10: *The hybrid model (dotted) coupled with the classical fluid model (left column) or the extended fluid model (right column) is compared with the classical fluid model (dashed) and the particle model (solid) for a front propagating into a field of $E^+ = -100\,\mathrm{kV/cm}$. The model interface is located at three different levels of the field $E = yE^+$ with $y = 0.6, 0.9,$ and 0.98 shown in the upper, middle and lower panel, respectively.*

conservation in the system, while the first-order weighting may cause charge loss or gain near the model interface when it is applied in a non-uniform density region. Therefore, zero-order weighting is implemented in our hybrid model.

4.3.3 The position of the model interface

We have discussed the suitable position of the model interface in Chap. 3 where the particle model and the classical fluid model were coupled in space. It was shown that in the front part of the ionization front, the mean electron energies in the classical fluid model where lower than in the particle model, while behind the front the electron energies in both models are in good agreement. Therefore for a good agreement between hybrid and particle simulation, in the hybrid model the fluid model can be used behind the front, and a sufficiently large part of the density decay region should be covered by the particle model.

Now within the hybrid model, the classical fluid model is replaced by the extended fluid model. Since an extra non-local term was introduced, such that the fluid simulation results are now closer to the particle results, we expect that a smaller region needs to be covered by the particle model without changing the result of the hybrid model.

Fig. 4.10 shows the simulation results of an ionization front propagating into a field of $E^+ = -100\,\text{kV/cm}$; the left column shows results of the old hybrid model and the right column those of the new hybrid model. The model interface is located at three different positions: $E = y\,E^+$ where $y = 0.6$, 0.9, and 0.98, corresponding to the upper, middle and lower panel, respectively. Both in the old and the new hybrid simulation, a long buffer region of $32\,\Delta z$ has been used to ensure the stable interaction of the models at the model interface. On the left, the old hybrid model for $y = 0.6$ generates the same electron density behind the front as the particle model, for $y = 0.98$ the same density as in the classical fluid model, and for $y = 0.9$ some intermediate density; we recall that the density difference between particle and classical fluid model is 20 % for this field. On the right where the extended fluid model is used, the new hybrid model produces similar results as the particle model in all three cases $y = 0.6$, $y = 0.9$ and $y = 0.98$.

The comparison shows that when the extended fluid model is used instead of the classical fluid model, the performance of the hybrid model is largely improved. Using the extended fluid model in the hybrid computation, the particle model can focus on a smaller portion of the front where the electron density is much lower while the electron density behind the front is still calculated with high accuracy. This greatly reduces the number of electrons that need to be followed in the particle region. It will give a substantial improvement of computational efficiency in a 3D simulation where millions of electrons will be pushed into the fluid region when the fluid model can be applied further ahead within the front.

To determine the proper position of the model interface, different positions have been tested in planar front simulations. Fig. 4.11 shows the relative density differences Eq. (4.12) between the hybrid simulation and the particle simulation as a function of the position of the model interface; here the field ahead of the ionization front is $E^+ = -100$ kV/cm. The model interface is placed at an electron density level $n_e = x\,n_{e,max}$ where x varies. For $x = 1$, the model interface is at the density peak $n_{e,max}$ of the ionization front. From $x = 1.0$ to 0.1, the model interface moves forward within the front, and $x = 0$ corresponds to a full fluid simulation. The full particle simulation is denoted as $x = 1.1$.
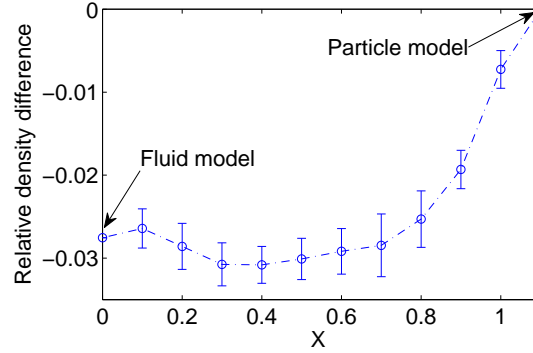
Figure 4.11: *The relative density differences Eq. (4.12) between the hybrid simulation and the particle simulation as a function of the position of the model interface $n_e = x\, n_{e,max}$ for $E^+ = -100\ kV/cm$, The value $x = 0$ accounts for the extended fluid model. The full particle simulation is denoted as $x = 1.1$.*

4.3.4 The buffer region

The particle model extends backward, beyond the model interface, into the buffer region where particle and fluid model coexist; it supplies particle fluxes for the fluid model at the model interface, as illustrated in Fig 4.9. However, correct particle fluxes require correct particle statistics within the buffer region whose length should be as small as possible to reduce computation costs, but larger than the electron energy relaxation length [137].

Adding particles in the buffer region

As we have mentioned, to ensure a stable electron flux at the model interface, in general new particles need to be introduced into the buffer region, that have to be drawn from appropriate distributions in configuration space. This would pose a particular problem for the streamer simulation, since Maxwellian or even Druyvesteyn [66] distributions are inaccurate. However, even for negative streamers, the electrons on average move somewhat slower than the whole ionization front, which means that the electrons on average are moving from the particle region into the fluid region.

Suppose that when the computation is changing from the pure particle regime to the hybrid regime, we create a buffer region which is long enough to relax most of the fast electrons. The particles in the buffer region are the heritage of the pure particle simulation and will keep being followed by the particle model. Around one end of the buffer region, the model interface at z_d, particles can fly freely. But

around the other end of the buffer region at z_c, there are electrons flying out of the buffer cells but no electrons enter, i.e., when the model interface stays still, the buffer cells are losing particles. If we add electrons in the buffer region near z_c to create a flux from the fluid cell z_{c-1} into the buffer region z_c, although the particle loss is compensated, these inflowing particles have hardly any influence on the flux across the model interface when $z_d - z_c$ is sufficient long. Once the model interface moves forward, those added particles near z_c will fall into the fluid region and be removed again.

This hypothesis has been tested in hybrid simulations with two kind of fluxes used at $z_{c-1/2}$:

- No influx: electrons can only fly out over $z_{c-1/2}$, but not fly back.

- Reflected influx: electrons that fly out over $z_{c-1/2}$ fly back immediately with inverted velocity.

The hybrid simulation has been carried out for a planar front at -100 kV/cm with the model interface at $E = 0.6$, 0.8, 0.9 E$^+$. With a long buffer region of 10 Δz, there is no influence of the inflowing particles. We even tested the artificial case of "double reflection influx", where twice as many electrons fly back with doubled energies. Even then, there was no notable influence.

So we conclude that if electrons move on average more slowly than the front, the electron loss at the end of a sufficiently long buffer region does not affect the calculation of particle fluxes at the model interface. Therefore the particles lost at the end of the buffer region can be ignored and new electrons do not need be created artificially. This actually leads to a simpler technique of model coupling in which the correct energy distribution of particles is not a concern any more. This technique is not only suitable for streamer simulations, but for all two phase problems where the front speed is higher than the speed of the individual particles, as is generally the case in "pulled front" problems [75, 246]. For example, bacterial growth and transport, or wound healing as a front propagation problem can be treated this way.

The length of the buffer region

A reasonable particle flux can be obtained without artificially adding new electrons in a sufficiently long buffer region. But how long is enough long? Although electrons on average propagate slower than the model interface, the high energy electrons at the tail of the energy distribution may move faster than the ionization front in a short time interval. The buffer region should be long enough that most of the fast electrons can relax to mean energies within this short time. The relaxation length of the fast electrons at the ionization front was discussed in Sect. 2.2.3. It shows that
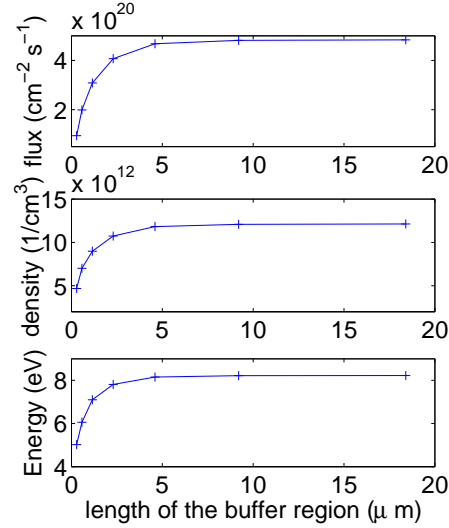
Figure 4.12: *Hybrid calculation of an ionization front propagating into the field of* -100 *kV/cm with the model interface placed at 0.9 E^+. The plots show the average of electron flux (first panel) at the model interface, and densities (second panel) and mean energies (third panel) of the electrons around the model interface as a function of the buffer length region. It shows that all the quantities converge when buffer length increases.*

electrons with 50 eV (as shown in Fig. 2.2 where swarm with identical energy of 0.5, 5, and 50 eV are tested) rapidly (within 2 ps) equilibrate as they lose their energy in collisions. If the buffer region is very short, high energy electrons might enter from the fluid region and contribute to the flux on the model interface, but since they are not be included in the buffer region, such short buffer region will result in a lower flux on the model interface.

A stable flux can be obtained only when the buffer region is long enough to relax most high energy electrons to the local energies within the buffer region. An upper-bound of mean forward velocity (v_z) of local electrons, the front velocity of $v_f \approx 7 \times 10^5$ m/s at -100 kV/cm. When an electron with 50 eV and with very small radial velocity components, i.e. $v_z \gg v_r$, relaxes to the local electron energy, its velocity in the forward direction v_z' decreases from $\sim 4 \times 10^6$ m/s to v_f within 2 ps, and it propagates $2 \times 10^{-12} \cdot (v_z' + v_f)/2 = 4.7$ μm, which is approximately 2 cells.

Experiments with different lengths of the buffer region are shown in Fig. 4.12. Here we plot average flux, density and energy of the electrons around the model interface for buffer regions of different lengths. The field ahead the front is $E^+ =$

E^+	50	75	100	125	150	175	200
x	0.5-0.9	0.55-1.0	0.6-1.0	0.65-1.0	0.7-1.0	0.8-1.0	0.9-1.0
tested x	0.5	0.55	0.6	0.65	0.7	0.8	0.9
buffer cells	1	1	2	2	2	3	3

Table 4.2: *The proper position of the model interfaces for different fields, where $n_e = x\, n_{e,max}$.*

$-100\,$kV/cm and the position of the model interface is at $E = 0.9E^+$. It is clear that as the length of the buffer region increases, not only the flux densities, but also the electron density and the mean electron energy converge to their limit values. Our computational cells are 2.3μm long, and a buffer region with the length of 2 cells can already give a reasonable flux at the model interface.

4.4   Simulation results in different fields

Having presented our hybrid simulations of the front propagating into a field of $E^+ = -100$ kV/cm in detail, we now summarize results for fields ranging from -50 to $-200\,$kV/cm.

In Fig. 4.13, we present the relative density discrepancies $\left(n^-_{e,part} - n^-_{e,hybr} \right) / n^-_{e,part}$ of the saturated electron density n^-_e behind the ionization front for different fields; here $hybr$ denotes hybrid simulation and $part$ particle simulations. For each field, the model interface has been placed at electron density levels $n_e = x\, n_{e,max}$, with $x = 1.0, 0.9, \ldots, 0.1$. A long buffer region with 32 cells was used in the hybrid calculation to ensure a stable flux at the model interface. Two horizontal dashed lines have been added at $\pm 5\%$ to assist the choice of the proper position of the model interface. For example for a field of $E^+ = -125$ kV/cm, the relative density difference is limited to $\pm 2\%$ even if only a very small part of the front $x = 0.1$ is covered by the particle model. But due to the flux convergence problem discussed in Sect. 4.3.4, the model interface will be put slightly more backwards to have a stable flux in our actual hybrid computational model, as the computational costs are actually determined by the position of the back end of the buffer region.

We summarize the proper positions of the model interfaces for different fields in Table. 4.2. With the positions chosen from this table, we have tested different lengths of buffer regions. For the buffer lengths given, the electron flux, density and mean energy lie not more than 2% off the limit of a very long buffer region.
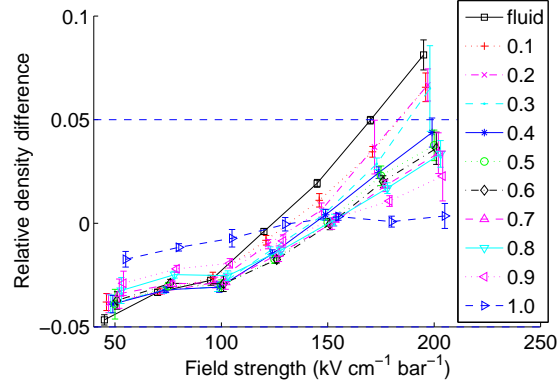
Figure 4.13: *The relative density differences between the hybrid simulation and the particle simulation as a function of the position of the model interface in a range of fields. The model interface is at the position where the electron density level is $n_e = x\, n_{e,max}$.*

4.5 Conclusion

The particle model contains all the essential microscopic physical mechanisms that are thought to be relevant for the propagation of an ionization front. The fluid model is much more efficient since the particles are approximated as continuous densities. To combine the computational efficiency of the fluid model and the full physics of the particle model, a spatially hybrid model has been implemented for the planar front. The hybrid model uses a particle model in the leading part of the ionization front and an extended fluid model for the rest.

The extended fluid model has been introduced as an alternative to the classical fluid model; it maintains an electron flux that is consistent with the particle model. Comparing particle and fluid models both in swarm and in planar front experiments, we decided to use the extended fluid model rather than the classical fluid model in the hybrid computation.

The hybrid model concept fulfills the efficiency requirement for large scale computations, and it minimizes the influence of the non-physical assumptions made in the fluid model. Moreover, since the ionization front corresponds to the region generating electrons with high energy and since a kinetic description is used in this region, the interesting physical phenomena such as jumping and branching of an ionization front, and energetic electrons causing radiation, can now to be studied within a fully simulated streamer without having to rely on super-particle simulations with their erroneous statistics.

We discussed the hybrid algorithms and our numerical implementation in detail.

After testing the hybrid model at $-100 \,\mathrm{kV/cm}$, we also presented the hybrid simulation results for other fields. And a set of recommendations on the position of the model interface and the length of the buffer region are also given for 3D simulations.

Although the spatially hybrid model is discussed in the context of streamer simulations, we would like to emphasize a particular point that is generic for pulled front problems. As the electrons on average move backward in a frame moving with the average front velocity, the problem of creating particles with proper statistics in the buffer region does not need to be solved. This problem here would be particular severe, as the distribution of electron energies and velocities are far from thermal and not even in equilibrium with the local electric field. But in many other cases, the distribution of inflowing particles is unavailable or difficult to obtain as well. The simplified coupling approach here offers an alternative for those problems without having to consider the influx on the back end of the buffer region.

Chapter 5

3D particle model and fluid model

As a building block for the 3D hybrid model, particle model and fluid model are developed in 3D. We compare transport coefficients, ionization rate and mean energy of the electrons generated in our particle model with a Boltzmann solver, BOLSIG, where the same electron-nitrogen collision cross sections are used. They agree very well when the same scattering method is applied. To study possible numerical artifacts in a super-particle simulation method, we compare simulation results for either real particles or super-particles during the avalanche to streamer transition. The fluid model uses the parameters generated by particle swarm experiments. The calculation of the electron flux needs extra care since the diffusion is a tensor in our model. The electric field is calculated with a 3D FISHPACK subroutine and the numerical error is estimated in a test problem.

5.1   Introduction

The 3D particle model and the 3D fluid model are the fundamental building blocks of the 3D hybrid model. We have explained our 1D particle and fluid model in detail for the planar front in Chap. 2, here we will extend it into 3D.

After the 1D [254] and 1.5D [62] density simulations of the gas discharge up to today, and after various 2D [64, 99, 14] fluid descriptions developed in the last 20 years, only recently 3D models become available [183, 149]. While from 1D to 2D, the nonuniformity of particle densities over a transversal cross section and space charge enhanced fields are included in the fluid description, the 3D model allows streamers to branch in a more realistic way than in 2D [209, 142, 164], and their interactions can be studied as well.

Most particle simulations are carried out using a particle-in-cell/Monte Carlo collision (PIC/MCC), where normally super-particles are used. Due to the already heavy computational cost for a large amount of particles, a full 3D description is very hard to realize. Positions and velocities of the particles are defined in 3D in the standard PIC/MCC procedure, while the electric field is normally calculated in 1D [128, 130] or 2D [56, 65].

The cross section and the differential cross sections of the electron-neutral collisions are crucial for the particle model. While many experimental measurements and analytical descriptions for various collision processes are available in the literature, most of them are not in the form ready to be used in the Monte Carlo procedure. As a part of the effort to improve our particle model, we reviewed the literature for suitable cross sections and differential cross sections for electron-nitrogen collisions. While the cross sections and differential cross sections used in our present model is presented in this chapter, the review is summarized in Appendix B.

To test the performance of our particle model, the transport coefficients, reaction rates and the average electron energies generated in the particle swarm experiments are compared with a Boltzmann solver (BOLSIG) when the same scattering method is used. The comparison gives a good agreement except for the diffusion rate.

The particle model is normally used for the simulation of the avalanche or the avalanche-streamer transition phase. Instead of real particles, super-particles where one computational particle stands for the mass and charge of many real particles, are normally employed to reduce the computational cost. However the super-particles have their own drawbacks, not only with lower resolution of the studied particles (which is important for the study of run-away electrons), but more importantly, the super-particles cause numerical heating and stochastic errors as we will show below.

In our fluid model, the transport coefficients and the ionization rate are parameters generated from the particle swarm experiments. As the particle swarms show
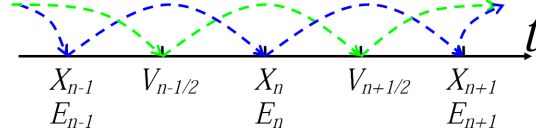
Figure 5.1: *The Leapfrog scheme*

different diffusion rates in the longitudinal and transversal direction of the electric field, the diffusion is implemented as a tensor in the fluid model.

In both particle and fluid model, the electric field needs to be calculated and it needs to be solved in the most efficient way. A fast 3D subroutine of the FISHPACK is chosen to do this job and the error and the computational time are evaluated with a test problem.

5.2 3D Particle model

In the particle model, electrons are accelerated and advanced sequentially by solving the equation of motion $\ddot{X} = qE/m$ in each time step.

In the temporal scheme shown in Fig. 5.2, electron positions and velocities are offset in time by $\Delta t/2$, which allows for the leapfrog difference method,

$$\mathbf{X}_{n+1} = \mathbf{X}_n + \Delta t \mathbf{V}_{n+\frac{1}{2}} \tag{5.1}$$

$$\mathbf{V}_{n+\frac{1}{2}} = \mathbf{V}_{n-\frac{1}{2}} + \Delta t \frac{q}{m} \mathbf{E}(\mathbf{X}_n, t_n) \tag{5.2}$$

where q and m are electron charge and mass, $\mathbf{X}_n = (x, y, z)_n$ is the vector of electron position in 3D at time t_n, and $\mathbf{V}_{n+\frac{1}{2}} = (v_x, v_y, v_z)_{n+\frac{1}{2}}$ is the electron velocity in 3D at time $t_{n+\frac{1}{2}}$.

The electron-neutral collisions happen randomly within a probability, which is normally a function of the electron energy. The collisions have no time duration and change the velocity and possibly the energy of electrons. Though collisions are dealt with stochastically, on average the collision time of an electron with energy ϵ is determined by its cross sections (CS) and its scattering angle is determined by the differential cross sections (DCS). The cross sections and differential cross sections are the core of the particle model and have direct influence on simulation results [129].

The Monte Carlo method samples the collision probabilities to set the next collision time of each electron by using random numbers. If the next collision time is obtained by calculating the collision frequency for each electron after each collision,
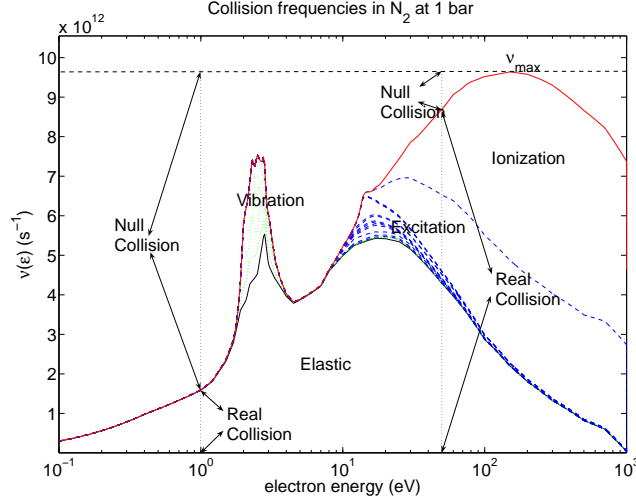
Figure 5.2: *Total Collision frequencies in N_2 at 1 bar, including null collisions.*

the simulation can be computationally very expensive. And such frequent calcula-
tion gives the correct physical meaning only when the electron energy has changed
very little during the free flight. For example, two groups of electrons with the same
energy in a strong field have the same average of the next collision time t. But if one
group advances in the direction of the electric field and the other marches in the op-
posite direction, then one group is losing energy and the other is gaining energy, and
their collision probability changes correspondingly. The sampling of next collision
times based on their energy at the starting point can not represent the probability
changing during the free flight.

Without knowing the incident energy of the next collision, the sampling results
may give a wrong distribution of collision times. This can be avoided by introduc-
ing a collision which is called "null collision", which is actually a pseudo collision
because nothing changes in this collision process. With the null collision technique,
the next collision time is calculated right after the previous collision, but whether the
collision will happen or not can only be determined at the moment when the next
collision happens. In Fig 5.2, we show the total collision frequency as a function of
electron energy. Once a collision is set to happen, the incident energy ϵ_c is first cal-
culated. Another random number is drawn to determine the collision process based
on the cross section of the electron with ϵ_c.

5.2.1 Collision processes

Here we will only discuss the electron collisions with nitrogen molecules. N_2 is the most abundant species in air and is also one of the best studied molecules. Hayashi has build a bibliography which includes 2240 original and review reports of experiments or theories of electron and photon cross sections and electron swarm data for the nitrogen molecule [104].

The electron-N_2 molecule collisions include the elastic, rotationally exciting, vibrationally exciting, electronically exciting, and ionizing collisions. A list of possible collision processes included in our particle code is given in Table 5.1, in which the threshold energies are taken from the BOLSIG package [165].

Total cross section (CS)

The CS data can be obtained through either one or more of the following means: (1) measurement from single-scattering beam experiments [46], (2) theoretical calculations [195, 167] or (3) inversion of swarm experimental data [59]. And different CS data have been used by different authors for different purposes, for example, the National Institute of Standards and Technology (NIST) electron impact cross section [124] was used in the particle avalanche model [65], the evaluated electron data library (EEDL) was used for the simulation of high energy electron avalanches [16], and the Siglo database is used in avalanche [140] and streamer simulations [56]. None of the CS data mentioned above includes the CS for electrons in the energy range from low energy (less than 1 eV) to very high energy (above 1 MeV). Simulations that study how high energy electrons emerge from low energy electrons, normally combine different compilations [244, 168].

Only a few benchmark studies have been done to compare the simulation results generated from those CS data with experimental swarms. The cross sections [195] derived by Phelps and Pitchford have been tested by comparing the results of Monte Carlo (MC) simulations with experimental data for electron swarms for N_2 [231]. The cross sections in our model are taken from their work.

Differential cross section (DCS)

The DCS determines the probability of the impact electron flying into a certain angle after the collision, which is extremely important for the study of run-away electrons from the streamer. In Fig. 5.2.1 we compared the differential cross sections for electrons with energies 0.01, 0.1, 1, 10, 20, and 50 eV in an elastic collision by four different scattering methods from Born approximation (upper left), Okhrimovskyy *et al.* (upper right), Phelps and Pitchford (lower left) and Surendra *et al.* (lower

Collision process	Reaction	Threshold energy (eV)
elastic	$e + N_2 \rightarrow e + N_2$	$\cdots$
rotational	$e + N_2 \rightarrow e + N_2^*$	0.02
vibrational	$e + N_2 \rightarrow e + N_2^* \ (X^1\Sigma_g^+, \nu'' = 0)$	0.29
	$e + N_2 \rightarrow e + N_2^* \ (X^1\Sigma, \nu' = 1)$	0.291
	$e + N_2 \rightarrow e + N_2^* \ (X^1\Sigma, \nu' = 2)$	0.59
	$e + N_2 \rightarrow e + N_2^* \ (X^1\Sigma, \nu' = 3)$	0.88
	$e + N_2 \rightarrow e + N_2^* \ (X^1\Sigma, \nu' = 4)$	1.17
	$e + N_2 \rightarrow e + N_2^* \ (X^1\Sigma, \nu' = 5)$	1.47
	$e + N_2 \rightarrow e + N_2^* \ (X^1\Sigma, \nu' = 6)$	1.76
	$e + N_2 \rightarrow e + N_2^* \ (X^1\Sigma, \nu' = 7)$	2.06
	$e + N_2 \rightarrow e + N_2^* \ (X^1\Sigma, \nu' = 8)$	2.35
electronic	$e + N_2 \rightarrow e + N_2^* \ (A^3\Sigma_u^+, \nu' = 1 \rightarrow 4)$	6.17
	$e + N_2 \rightarrow e + N_2^* \ (A^3\Sigma_u^+, \nu' = 5 \rightarrow 9)$	7.00
	$e + N_2 \rightarrow e + N_2^* \ (B^3\Pi_g)$	7.35
	$e + N_2 \rightarrow e + N_2^* \ (W^3\Delta_u)$	7.36
	$e + N_2 \rightarrow e + N_2^* \ (A^3\Sigma_u^+, \nu' = 10)$	7.80
	$e + N_2 \rightarrow e + N_2^* \ (B'^3\Sigma_u^-)$	8.16
	$e + N_2 \rightarrow e + N_2^* \ (a'^1\Sigma_u^-)$	8.40
	$e + N_2 \rightarrow e + N_2^* \ (a^1\Pi_g)$	8.55
	$e + N_2 \rightarrow e + N_2^* \ (w^1\Delta_u)$	8.89
	$e + N_2 \rightarrow e + N_2^* \ (C^3\Pi_u)$	11.03
	$e + N_2 \rightarrow e + N_2^* \ (E^3\Sigma_g^+)$	11.88
	$e + N_2 \rightarrow e + N_2^* \ (a''^1\Sigma_g^+)$	12.25
singlet	$e + N_2 \rightarrow e + N_2^* \ (c'^1\Sigma_u^+)$	15.8
	$e + N_2 \rightarrow e + N_2^* \ (b'^1\Sigma_u^+)$	17.3
ionization	$e + N_2 \rightarrow e + e + N_2^+$	15.60

Table 5.1: *Electron-molecular collision processes in nitrogen (Phelps and Pitchford)*

right). With all four scattering methods tested, electrons tend to scatter isotropically or even lightly back when the electron energy is low, and forward when the energy is high. For details of these differential methods and their formulas, we refer to Appendix B. In our model, the formula derived by Okhrimovskyy *et al.* has been implemented for elastic collisions.

The electron scattering from the rotational, vibrational and electronic excitations have been assumed to have the same scattering probabilities as from the elastic collisions. The experiment has shown that the electron scattering is different for different collisions [46]. A more realistic particle model can be obtained by including different
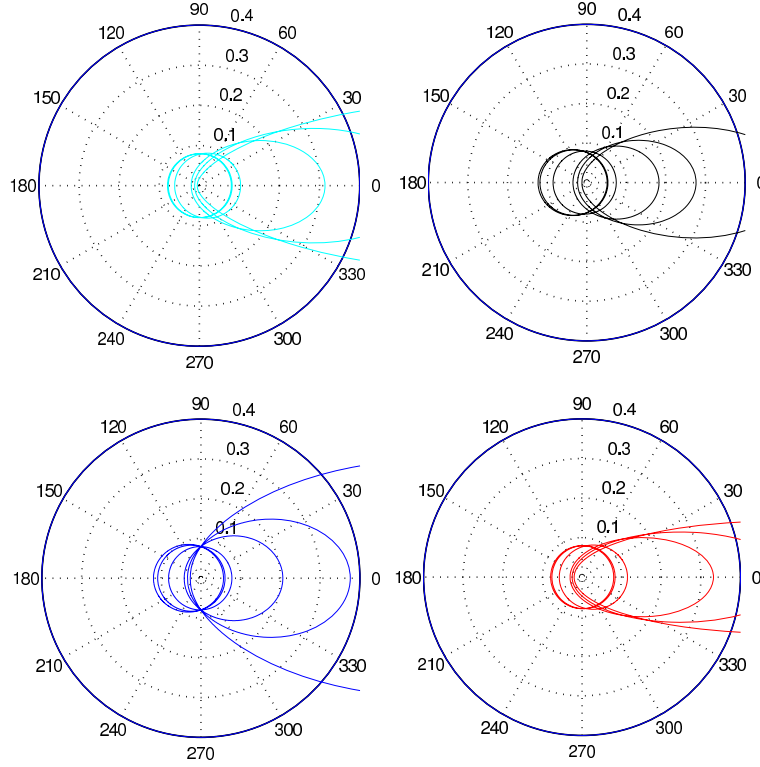
Figure 5.3: *The normalized differential cross section of electrons with energies $\epsilon =$ (0.01, 0.1, 1, 10, 20, 50) eV for 4 different scattering methods from Born approximation (upper left), Okhrimovskyy et al. (upper right), Phelps and Pitchford (lower left) and Surendra et al. (lower right).*

differential cross sections for different excitational collision process. In Appendix B, we summarize the cross sections and differential cross sections for different collision processes in the literature, but this is not sufficient since many measured data are only for a few discrete energies and in the form of tables, which is not yet ready to be implemented in the particle model without finding empirical fits and extrapolating to other energies.

In an ionizing collision, the incident electron loses energy and a new electron will be ejected. Since Opal reported his measurements of the secondary electron spectra [182], most particle models follow his empirical fit for the ejected electron energy. In Fig. 5.4, we show the secondary electron energy for a given random
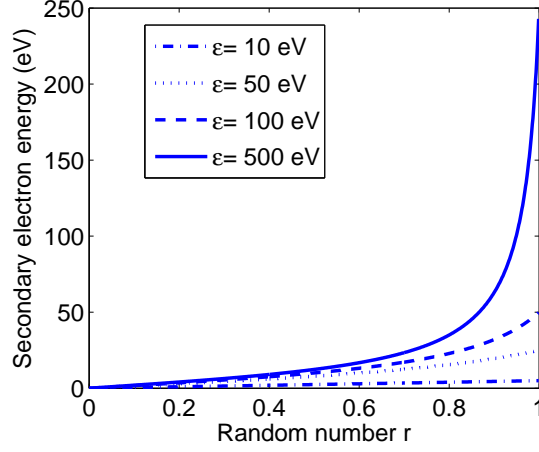
Figure 5.4: *Opal's empirical fit for the ejected electron energy with given incident electron energy ϵ = 10, 50, 100, 500 eV.*

number $R \in [0, 1]$. For an incident electron of 500 eV (the top curve), the maximum energy of the ejected electron is less than 250eV and can have an energy below 40eV with 80% probability. That is, the high energy incident electron is likely to keep most of its energy. The scattering angle of both primary and ejected electron can be determined from their energy splitting [29].

5.2.2   Comparison with BOLSIG

The particle model has been tested and compared with the BOLSIG+ package [165]. BOLSIG+ is a Boltzmann solver to calculate electron transport coefficients in gases or gas mixtures. It is based on the two-term Legendre expansion solution of the Boltzmann equations [196] with the assumption of isotropic scattering.

Both the particle model and the BOLSIG+ package use the same cross section (SIGLO [165] database) with the same assumption of isotropic scattering . The energy splitting between the primary and the secondary electrons during an ionization has two different modes in BOLSIG+, "equal sharing" or "primary electron takes all". In both BOLSIG+ and our particle model, we used "equal sharing".

With the cross section and differential cross sections, the electron transport coefficients and reaction rates obtained from the particle simulations or Boltzmann solver should be comparable.

In Fig. 5.5, we show the electron mobility μ, electron diffusion D_T, mean en-
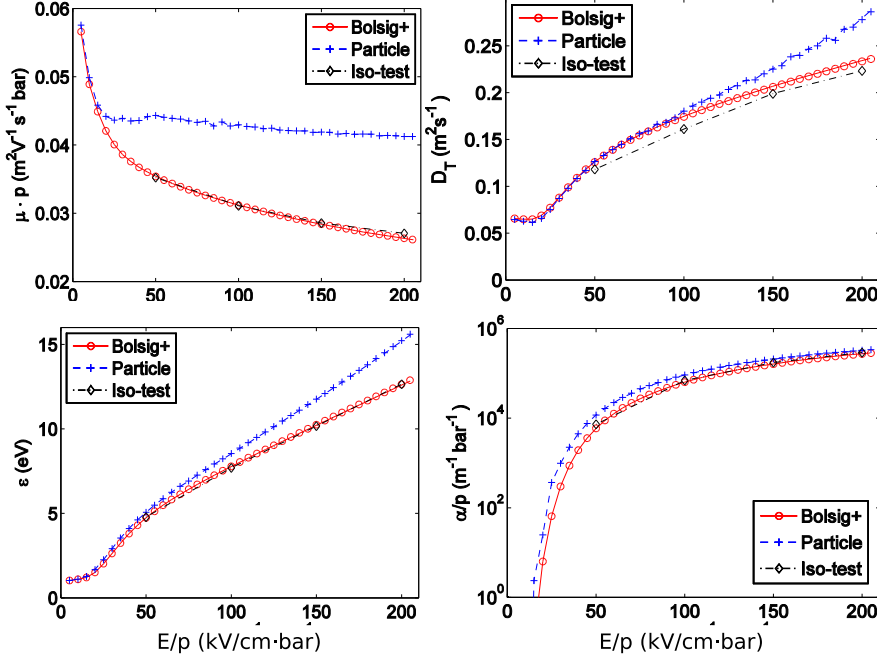
Figure 5.5: *Comparison of the transport coefficients, ionization rate and the mean energy of electrons in a swarm with the results of* BOLSIG+ *[165, 103].*

ergies and the ionization rate α of electron ensembles as a function of the electric field. The results are generated by BOLSIG+ (solid line, "o", noted as "Bolsig+"), by the particle simulation with isotropic scattering and with equal energy sharing in an ionization collision (dash dotted, "$\diamond$", noted as "Iso-test"), and by the particle simulation with anisotropic scattering and uneven energy sharing (dashed line, "+", noted as "Particle").

It shows that with the same differential cross sections, the particle model generated μ, $\bar{\epsilon}$ and α agree well with the results of BOLSIG+. A discrepancy appears in the comparison of D_T.

When the anisotropic scattering and Opal's empirical fitting function are used in an ionizing collision, the properties compared in Fig. 5.5 show a good agreement for low fields, and differences build up and increase as the fields increase (except for the ionization rate).

The choice of the differential cross sections and the energy splitting in an ionizing event have direct influence on the electron energy distribution function (EEDF). In Fig. 5.6, we show the EEDF in a particle simulation with both isotropic ("$\diamond$") and
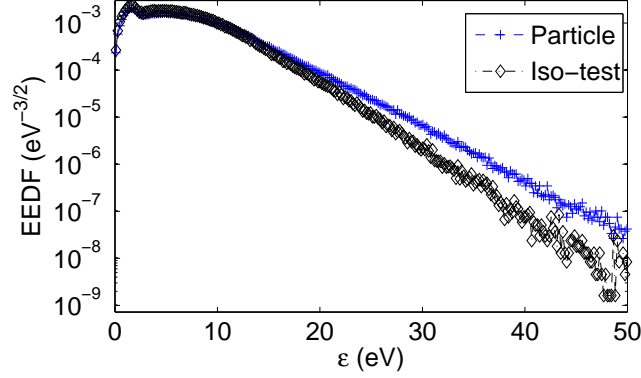
Figure 5.6: *The electron spectrum in the swarm experiments at 100 kV/cm. The "+" marked curve shows the particle simulation results with anisotropic scattering and uneven energy splitting in ionization collisions. The "◇" marked curve is obtained from the particle simulation with isotropic scattering and equal energy sharing in ionizing collisions.*

anisotropic ("+") scattering. It shows that high energy electrons are easier to produce with the anisotropic scattering, which will effect the μ, **D**, and α. For example, the mobility μ and mean energy $\bar{\epsilon}$ are higher in the case of anisotropic scattering. Since the collision frequency increases as electron energy increase from 0 to about 150 eV, a higher collision frequency leads to higher diffusion rates as $\bar{\epsilon}$ is higher. The influence on the ionization rate is complicated. While particles with higher energy create more ionization events, they also propagate faster. Therefore the ionization coefficient may either increase or decrease.

5.2.3   Super-particle induced numerical error

A fully kinetic treatment for all the individual particles is ideal but in general not feasible. The electron density inside a streamer channel is about $10^{14}/\mathrm{cm}^3$ at ground pressure. Recent laboratory observations [37] and computer simulations [151] show a minimal streamer radius $p \cdot r = 0.1$ mm·bar at a wide pressure range. The simulation of a streamer propagation for $l = 1$cm with the minimal radius will create $n_{\min} = V n_e = \pi r^2 l n_e \approx 3 \times 10^{10}$ electrons.

For each electron, the 6 components of position and velocity vector, and the next collision time, etc., are usually represented as double precision in Fortran or as double variable in C++, which occupies 64 bits or 8-bytes of computer memory. The storage of 3×10^{10} electrons requires $8 \times 7 \times 3 \times 10^{10}$ bytes, approximately 1500 GB (Giga byte) memory which is too much and it would take a long time for the computer

to move all electrons one time step forward. With the growing particle number, eventually the limits of any computer are exceeded. This difficulty can be counteracted by using super-particles carrying the charge and the mass of many physical particles, but super-particles in turn create unphysical fluctuations and stochastic heating as we will demonstrate below.

Here we show how a streamer emerges in a particle model from few seed electrons and a consecutive avalanche. The system is pure nitrogen at standard temperature and pressure in a constant high field of 100 kV/cm (equivalent to 372 Td). We assume that the electrodes are far away or don't exist as in many natural discharges. Qualitatively similar results in a fluid model are shown in Fig. 1 of [161].

The simulation starts from 100 pairs of electrons and ions at one point and follows the initial particles and their offspring up to time 0.306 ns. In Fig. 5.7, the simulated streamer is presented at two different times: t = 0.18 ns with real particles (first row), t = 0.306 ns with real particles (second row) and once again t = 0.306 ns, now in a super-particle simulation (third row). At time t = 0.18 ns (first row), we have approximately 10^5 electrons, and the maximal field enhancement is 1%. Therefore the discharge is still in the avalanche phase. For the second row, the computation is continued with real particles, while for the third row, super-particles are introduced as follows: if a specified number of particles, in our case 10^5, is reached, a particle remapping is applied to reduce the number of computational particles; in this step, half of them are thrown away at random and the weight of the remaining computational particles is doubled. At t = 0.306 ns, the total number of electrons is roughly 1.5×10^7 within the real particle simulation. The space charge layer has clearly formed. The maximal field enhancement is 50%. At t = 0.306 ns within the super-particle simulation, the total number of super-particles is about 7×10^4, each representing 256 real electrons. No charge layer has formed, but the charge density is noisy with a maximum inside the discharge. Clearly super-particles here are not appropriate to deal computationally with large electron numbers. In the following chapters , we will describe how to circumvent the unwieldy runtime of real particle models by using a hybrid model in 3D which couples particle and fluid model in different spatial regions.

5.3   3D Fluid model

As in the planar front simulation (Sect. 2.2.2), the electron and ion densities are discretized in space with a finite volume method based on the mass balances for all cells, and the electron density is updated in time using the third order upwind-biased advection scheme combined with a two-stage Runge-Kutta method. For the
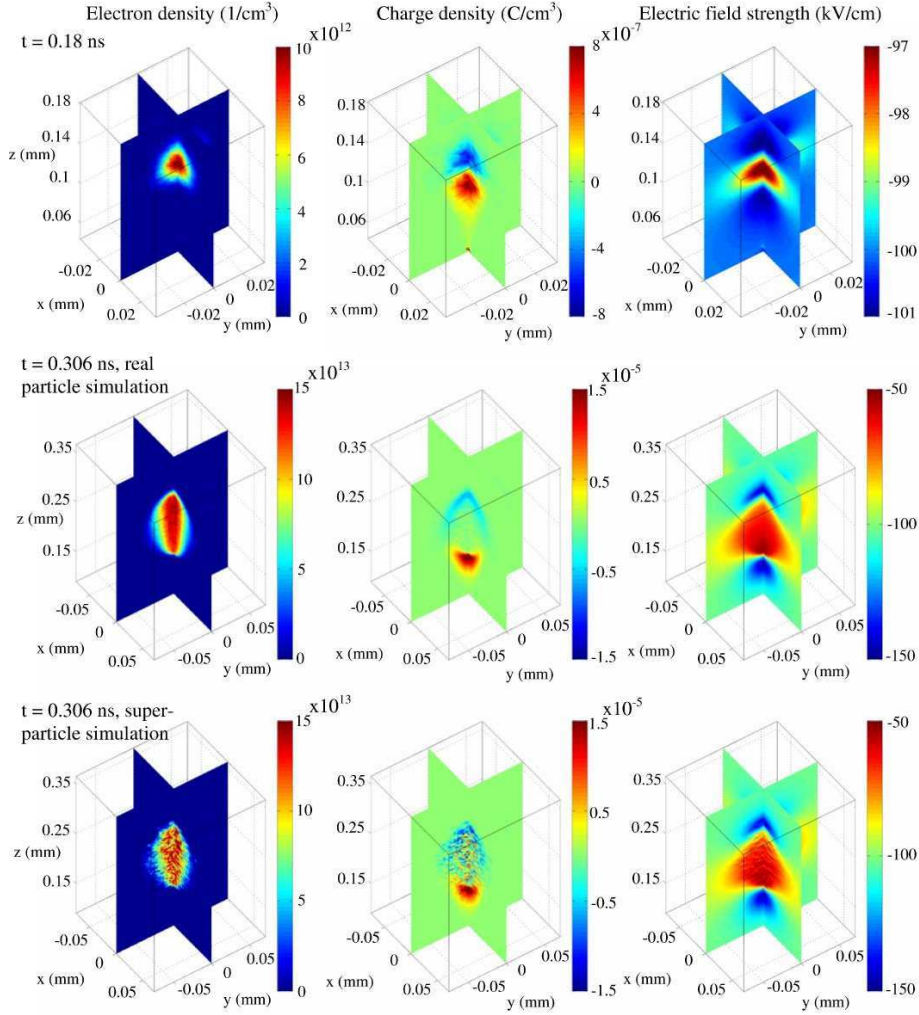
Figure 5.7: *Avalanche to streamer transition in nitrogen at standard temperature and pressure. A constant background electric field of 100 kV/cm points downwards. First row: avalanche of real particles at t = 0.18 ns, second row: streamer formed by real particles at t = 0.306 ns, third row: the same system at the same time t = 0.306 ns, but using super-particles with the mass of 256 real particles. The columns show from left to right: electron density, charge density, and electric field strength. Particle densities and fields are represented on two orthogonal planes that intersect with the 3-dimensional structure.*

details of the method, we refer to [163]. Here we discuss two problems which have not been covered in 1D calculations and which are important in 3D: the calculation of the electric field and the electron flux.

5.3.1 3D FISHPACK

FISHPACK is a collection of FORTRAN subprograms for the Poisson equation in Cartesian, polar, cylindrical, and spherical coordinates as well as solvers for more general separable elliptic equations. It uses the cyclic reduction method for the linear system [214] and has been proven to be one of the fastest Poisson solver in both 2D and 3D [33].

The FISHPACK 2D Poisson solver in cylindrical coordinates has been tested in [163] and used in [164, 151] for the calculation of the electric field. One major limitation found in the 2D test is that it does not deal accurately with very many grid points, which is due to numerical instabilities with respect to round-off errors. The same test is carried out below for the FISHPACK 3D Poisson solver in Cartesian coordinates.

The solver is tested with a Laplace equation in a 3D system $(x, y, z) \in (0, L_x) \times (0, L_y) \times (0, L_z)$,

$$
\begin{aligned}
\triangle \phi \;\; = \;\; & \{-6A + 4A^2[(x - L_x/2)^2 + (y - L_y/2)^2 + (z - L_z/2)^2]\} \\
& e^{-A[(x-L_x/2)^2 + (y-L_y/2)^2 + (z-L_z/2)^2]}
\end{aligned}
\tag{5.3}
$$

where $L_x = L_y = L_z = 1.0$. An inhomogeneous Dirichlet boundary condition is set in such a way that the exact solution is

$$
\phi = e^{-A[(x-L_x/2)^2 + (y-L_y/2)^2 + (z-L_z/2)^2]}.
$$

Depending on the value of A, the charge distribution on the r.h.s. of Eq. (5.3) can be either smooth or sharply peaked. Here we have tested two cases, $A = 1$ and $A = 100$. The tests have been done with both single and double precision.

The test is carried out on a desktop computer with 1GB memory, allowing calculation up to approximately $500 \times 500 \times 500$ or 10^8 grid points. The accuracy of the FISHPACK routine can be characterized by the discrete L_1, L_2, and L_∞ -norms of the errors. For a grid function

$$
v = (v_{i,j,k})
$$

double precision with A=1   double precision with A=100

single precision with A=1   single precision with A=100.
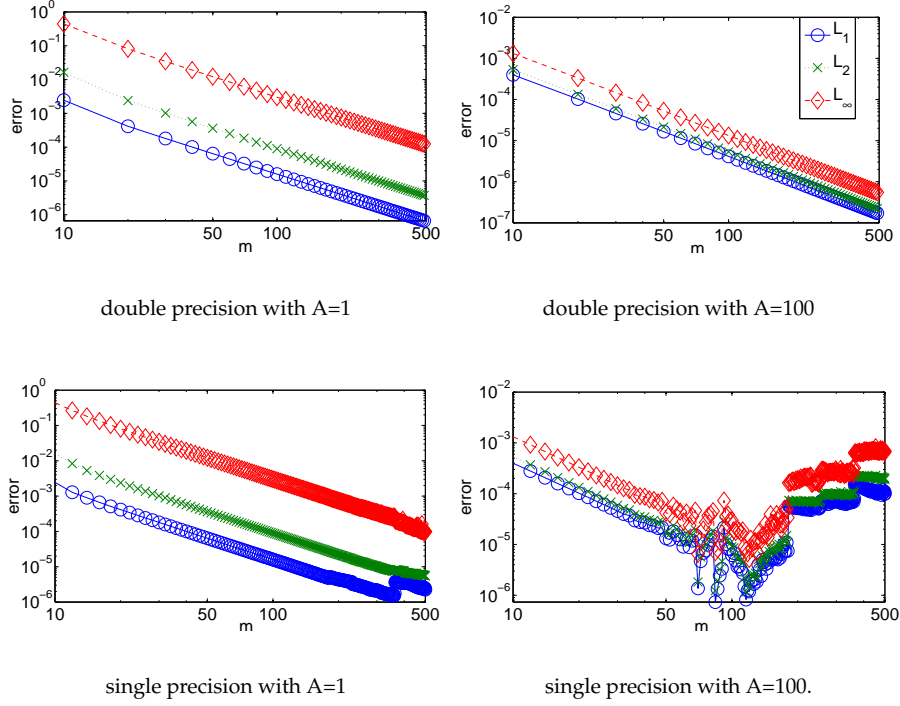
Figure 5.8: *The* FISHPACK *3D Poisson solver in Cartesian coordinates tested for a Laplace equation. The L_1-errors(solid), L_2-errors(dotted), and L_∞-errors(dashed) are displayed as a function of m. The upper and lower panel show the test results with single precision and double precision. The left and the right column show the test results with a smoothly distributed charge density and a sharply peaked Gaussian distributed charge density.*

on a $m \times m \times m$ uniform grid these norms are defined as

$$
\begin{aligned}
\|v\|_1 &= \sum_{i,j,k=1}^{m} \triangle x \triangle y \triangle z |v_{i,j,k}| \\
\|v\|_2 &= \sqrt{\sum_{i,j,k=1}^{m} \triangle x \triangle y \triangle z |v_{i,j,k}|^2} \\
\|v\|_\infty &= \max_{i,j,k}(|v_{i,j,k}|).
\end{aligned}
\tag{5.4}
$$

In Fig. 5.8, we show the L_p norms of the numerical errors obtained with the FISH-PACK routine on a $(m \times m \times m)$-grid, as a function of m. The upper and lower panel show the error of the double or single precision computations respectively, the left
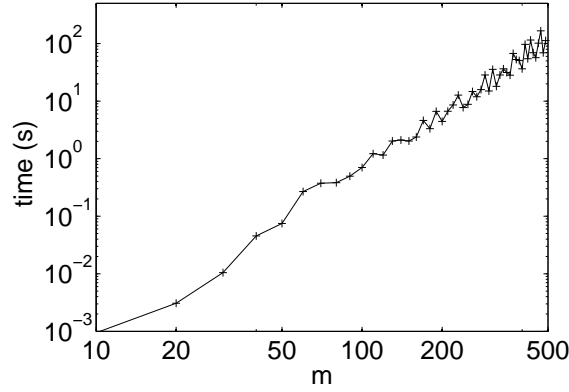
Figure 5.9: *The computation time of the* FISHPACK *3D Poisson solver on* $m \times m \times m$ *grids, as a function of* m. *The test is carried out on a desktop computer with* AMD *Athlon 1.6GHz CPU and 1G memory.*

and the right column show the error for A=1 and A=100 in the test.

Up to the number of grid points allowed by the memory limits, the errors obtained from double precision calculations are of second order, in agreement with the discretization. For the very peaked charge density with A=100, errors obtained from the single precision calculation are decreasing with the discretization till $m = 50$, and then become irregular. The single precision works better in the smoothed problem A=1, but the errors also start to fluctuate when $m = 350$. In our 3D simulation, the FISHPACK uses double precision to solve the Poisson equation.

The time consumption is one of our major concerns in 3D simulations. In Fig 5.9, we plot the computation time of the FISHPACK 3D Poisson solver on a desktop computer with AMD Athlon 1.6GHz CPU and 1G memory, as a function of m, when double precision is used.

The FISHPACK 3D Poisson solver is using the Fourier Transform in the third direction, therefore the computation time is not a linear function of m^3. As m increases from 10 to 500, the computation time increases from 7.66×10^{-4} s to 159.89 s.

5.3.2 Flux calculation

The free diffusion of electrons in electrostatic fields in gases is usually assumed to be isotropic in fluid simulations [64, 127, 14, 76, 13, 164]. However, electron diffusion generally is anisotropic [252, 147].

In the fluid model described here, the mobility μ, diffusion rate $\mathbf{D}$ and ionization rate α of electrons are averaged quantities of many particles obtained from particle

swarm experiments in a rather large spatial and temporal range. The diffusion rate in the longitudinal D_L and transversal D_T direction of the electric field are different due to the anisotropic collision process in the particle model: $D_L < D_T$ at low field $E < 30$ kV/cm, and $D_L > D_T$ when the field strength is above 30 kV/cm (see Chap. 2).

Continuity equations are solved on uniform grids with the electron and ion densities calculated at cell centers, which can also be viewed as cell averages. The electric potential ϕ and the field strength E are taken also in the cell centers, where E determines the electron and ion growth in the cell. The electric field components $\mathbf{E} = (E_x, E_y, E_z)$ are taken on the cell vertices, where they determine the mass fluxes.

In the swarm experiment, electrons propagate under a uniform and constant field $\mathbf{E}$ with mobility $\mu(E)$ and diffuse with rate $D_L(E)$ in the direction of the field and $D_T(E)$ perpendicular to the field. When μ and $\mathbf{D}$ are applied locally in each computational cell within the fluid model, each computational cell is considered as a small swarm and the definition of the μ and $\mathbf{D}$ shall be kept consistent.

Flux formulation in 2D

The numerical algorithm and the spatial discretizations of the continuity equations in a 2D radially symmetric system have been discussed in [163, 160]. The discretization of the flux terms requires extra care when the diffusion tensor is anisotropic [79]. For the flux of electrons, we have

$$\mathbf{j}_e = -\mathbf{F}^a - \mathbf{F}^d = -\mu(E)\mathbf{E}n_e - \mathbf{D}(\mathbf{E})\nabla n_e,$$

where the $\mathbf{F}^a$ and $\mathbf{F}^d$ denote the advective and diffusive electron fluxes through the cell boundaries, and $\mathbf{D}$ is a tensor in the form of

$$\mathbf{D}(\mathbf{E}) = D_L(E)\frac{\mathbf{E}\mathbf{E}^T}{E^2} + D_T(E)\left(\mathbf{I} - \frac{\mathbf{E}\mathbf{E}^T}{E^2}\right) \tag{5.5}$$

where $\mathbf{I}$ is the identity matrix. The equations for the particle densities are discretized with a finite volume method, based on mass balances for all cells.

We take the 2D example to explain how the electron flux is numerically discretized. As shown in Fig. 5.3.2, we have a uniform grid with the properties f evaluated in the centers of the grid cells. (f can be n_e, ϕ or E here.) Consider the flux on the boundary between cell (i, j) and $(i + 1, j)$. $F^a_{(i+\frac{1}{2},j),x}$ can be written as

$$F^a_{x,(i+\frac{1}{2},j)} = \mathbf{n}^T \mu(E)\mathbf{E}n_e \tag{5.6}$$
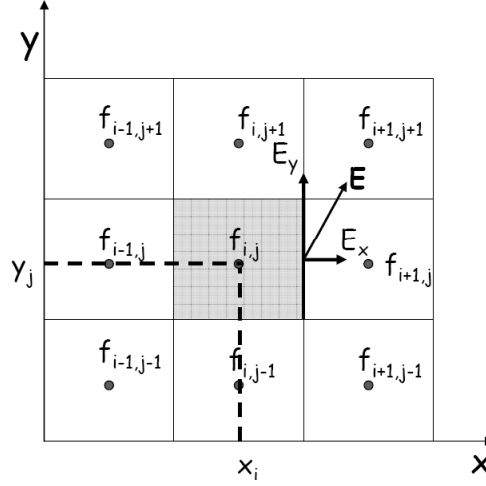
Figure 5.10: *Evaluation of the electric flux on the boundary between two cells.*

where $\mathbf{n}^T = (1, 0)$, and $\mathbf{E}^T = (E_{x,(i+\frac{1}{2},j)}, E_{y,(i+\frac{1}{2},j)})$ which is given as Eq. (5.7).

To obtain the electron diffusive flux at the cell boundary $(x_{i+\frac{1}{2}}, y_j)$, we need the electric field and the electron density gradients at the boundary. One of the possible choices for the electric field is

$$
\begin{aligned}
E_{x,(i+\frac{1}{2},j)} &= \frac{1}{\triangle x}\left(\phi_{(i,j)} - \phi_{(i+1,j)}\right) &\text{(5.7)}\\
E_{y,(i+\frac{1}{2},j)} &= \frac{1}{2}\left[\frac{1}{2\triangle y}\left(\phi_{(i,j-1)} - \phi_{(i,j+1)}\right) + \frac{1}{2\triangle y}\left(\phi_{(i+1,j-1)} - \phi_{(i+1,j+1)}\right)\right].
\end{aligned}
$$

The diffusive flux F^d is calculated as:

$$
F^d_{x,(i+\frac{1}{2},j)} = \mathbf{n}^T\left[D_L(E)\frac{\mathbf{E}\mathbf{E}^T}{E^2} + D_T(E)\left(\mathbf{I} - \frac{\mathbf{E}\mathbf{E}^T}{E^2}\right)\right]\nabla n_e \qquad \text{(5.8)}
$$

in which

$$
\begin{aligned}
\mathbf{E}^T &= \left(E_{x,(i+\frac{1}{2},j)}, E_{y,(i+\frac{1}{2},j)}\right)\\
E &= \sqrt{E^2_{x,(i+\frac{1}{2},j)} + E^2_{y,(i+\frac{1}{2},j)}}
\end{aligned}
$$

and $\nabla n_e = \begin{pmatrix} \partial n_e/\partial x \\ \partial n_e/\partial y \end{pmatrix}$ at cell face $(i + \frac{1}{2}, j)$

$$
\begin{aligned}
\frac{\partial n_e}{\partial x}_{(i+\frac{1}{2},j)} &= \frac{1}{\triangle x}\left(n_{e,(i,j)} - n_{e,(i+1,j)}\right) \\
\frac{\partial n_e}{\partial y}_{(i+\frac{1}{2},j)} &= \frac{1}{2}\left[\frac{1}{2\triangle y}\left(n_{e,(i,j-1)} - n_{e,(i,j+1)}\right) + \frac{1}{2\triangle y}\left(n_{e,(i+1,j-1)} - n_{e,(i+1,j+1)}\right)\right].
\end{aligned}
$$
(5.9)

The flux in the -x direction in 2D therefore can be written as

$$
j_{e,x} = -F_x^a - F_x^d = \mathbf{n}^T \cdot \left(-\mu(E)\mathbf{E}n_e - \mathbf{D}(\mathbf{E})\nabla n_e\right).
$$
(5.10)

Flux formulation and discretization in 3D

In 3D, the electron flux on one cell face can be written in the same way as Eq. (5.10) in 2D, where $\mathbf{D}$ is a tensor defined in Eq. (5.5), $\mathbf{n}$ is a vector normal to the cell face, $\mathbf{E}^T = (E_x, E_y, E_z)$ and $(\nabla n_e)^T = (\partial n_e/\partial x, \partial n_e/\partial y, \partial n_e/\partial z)$ at the concerned cell face.

An upwind-biased scheme with flux limiting is used to discretize the advective term. "This gives mass conservation and monotone solutions without introducing too much numerical diffusion" [160]. For the limiter we take the Koren limiter function. Denote $E^L = \max(-E, 0)$ and $E^R = \min(-E, 0)$ to distinguish the direction of the upwind for the field components, the F^a at cell face $(x_{i+\frac{1}{2}}, y_j, z_k)$ then can be rewritten as:

$$
\begin{aligned}
F_{x,(i+\frac{1}{2},j,k)}^a &= \mu(E_x)E_{x,(i+\frac{1}{2},j,k)}^L[n_{e,(i,j,k)} + \psi(p_{i,j,k})(n_{e,(i+1,j,k)} - n_{e,(i,j,k)})] \\
&+ \mu(E_x)E_{x,(i+\frac{1}{2},j,k)}^R[n_{e,(i+1,j,k)} + \psi(1/p_{i+1,j,k})(n_{e,(i,j,k)} - n_{e,(i+1,j,k)})]
\end{aligned}
$$
(5.11)

where

$$
p_{i,j,k} = \frac{n_{e,(i,j,k)} - n_{e,(i-1,j,k)}}{n_{e,(i+1,j,k)} - n_{e,(i,j,k)}}
$$

and ψ is the limiter function

$$
\psi(\theta) = \max\left(0, \max\left(1, \frac{1}{3} + \frac{\theta}{6}, \theta\right)\right).
$$

The diffusive flux is calculated with second-order central differences as

$$
F_{x,(i+\frac{1}{2},j,k)}^d = \mathbf{n}^T\mathbf{D}(\mathbf{E})\mathbf{n}(n_{e,(i,j,k)} - n_{e,(i+1,j,k)})/\partial x
$$
(5.12)

where $\mathbf{n}$ is a vector normal to the cell face.
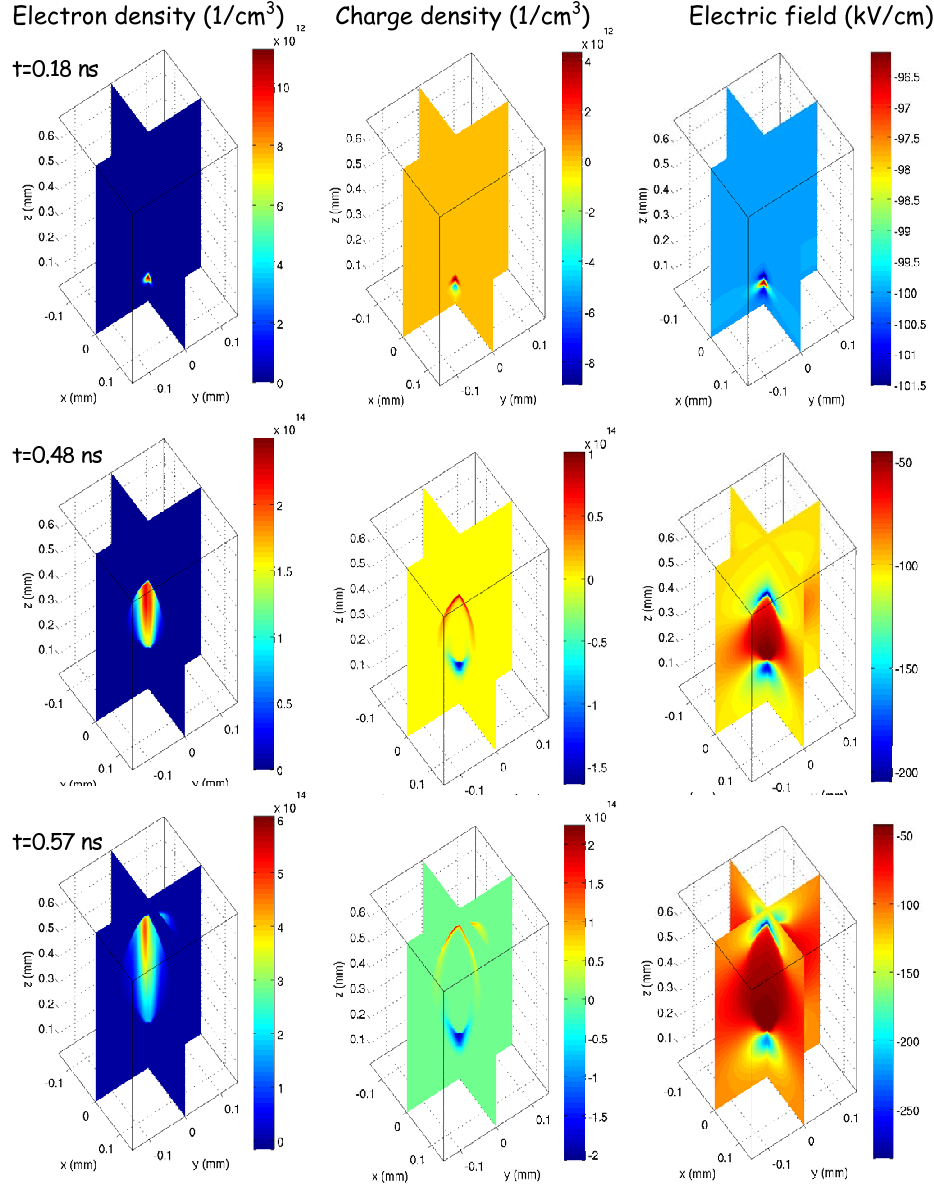
Figure 5.11: *Here we present 3D simulation results of the classical fluid model for a negative streamer developing in a background field of -100 kV/cm. First row: avalanche at t = 0.18 ns, second row: streamer at t = 0.48 ns, third row: streamer at t = 0.57 ns. The columns show from left to right: electron density, charge density, and electric field strength. Particle densities and fields are represented on two orthogonal planes that intersect with the 3-dimensional structure.*

5.3.3   Simulation result

Here we present 3D fluid simulation results for a negative streamer in nitrogen, propagating in a background field of -100 kV/cm. Note that we use the classical fluid model here. The initial particles are the same as in the particle simulation, 100 pairs of electrons and ions sitting at the same position. The simulation was carried out on a grid of $256 \times 256 \times 512$ points with $\Delta x = \Delta y = \Delta z = 2.3$ μm, on a system with $x \in$ [-0.29 0.29] mm, $y \in$ [-0.29 0.29] mm and $z \in$ [0 1.17] mm. The time step is $\Delta t = 3 \times 10^{-13}$ s.

In Fig. 5.11, the electron density (left column), charge density (middle column), and the electric field (right column) of a negative streamer simulated by the 3D fluid model, are shown at 0.18 ns (first row), 0.48 ns (second row), and 0.57 ns (third row). From the avalanche phase at 0.18 ns to the developed streamer at 0.57 ns, the maximal electron density increases from 1×10^{13} to 6×10^{14}/cm^3, while the maximal field increases from 101 kV/cm to about 300 kV/cm.

We have already shown the 3D particle simulation results at time 0.18 ns and 0.306 ns in Fig. 5.7. The results at the same time in the fluid model is also presented here, where t=0.18 ns is shown in Fig. 5.11 and t=0.306 ns is shown in in Fig. 5.12. The number of electrons in the streamer can be estimated from their densities in the fluid simulations. At 0.18 ns, there are 1.3×10^5 electrons in the fluid simulated streamer, which is higher than the number of electrons 10^5 in the particle simulation at the same time.

The particle model and the fluid model should produce about the same amount of electrons when the field has not changed much (see the comparison of swarms in Sect. 4.2.1). The difference is due to the initial conditions. Although the same number of seed electrons are implemented in both models, electrons in the particle model need time to gain energy before any ionization happens while the electron and ion densities in the fluid model start growing once the simulation starts. In both the particle model and the fluid model, the electric field has not changed much at 0.18 ns.

At 0.306 ns, the particle model reaches 1.5×10^7 electrons with real particle simulation, while the number of electrons in the fluid model is approximately 1.4×10^7, which is already less than in the particle model. As shown in Fig. 5.12, the streamer in the fluid model propagates slower since the field ahead is also lower than in the particle model, which is due to the lower ionization rate at the ionization front in the fluid model (see Chap. 2).

Within the time we investigated, the streamer in the particle simulation generates more electrons, which leads to a higher field enhancement and a higher front propagation speed than in the fluid simulation. These results agree with the compar-

Electron density   Charge density   Electric field
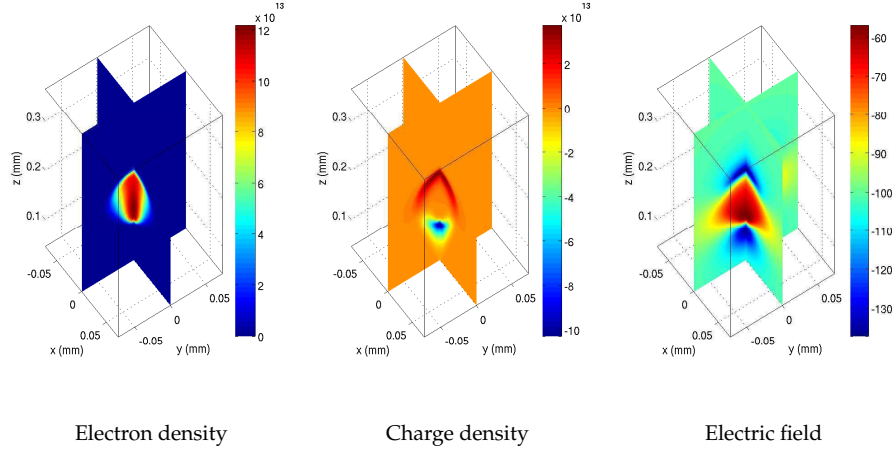
Figure 5.12: *The electron density (left), charge density (middle) and the electric field (right) in the fluid simulation at time 0.306 ns. Compared to the particle model at the same time, there are less electrons. The ionization front also propagates slower and the electric field ahead is less enhanced than in the particle simulation.*

ison of the two models for planar fronts, except that the different field enhancements are a generical 3D effect that can not be observed in planar fronts.

At 0.57 ns, the number of electrons is about 4.8×10^8 in the fluid simulation. With the real particle simulation, the particle model can never follow the streamer propagation to that stage. With super-particles, it is possible but it will take much longer time than in the fluid model, and the result may be strongly perturbed by the numerical heating and the stochastic error.

Chapter 6

Three-dimensional hybrid simulation

Based on the three-dimensional particle and fluid model discussed in Chap. 5 and on their hybrid coupling in one dimension discussed in Chap. 3 and 4, we here present development and first results of our 3D spatially hybrid scheme for streamer modeling. The 3D coupling in general employs the same method as the planar front, but new problems arise since the model interface is curved, and the transversal dimension of a grid cell is not a freely adjustable parameter anymore. A criterion for the position has to be developed, particles have to be traced properly across a stepped model interface, and particle number fluctuations in small computational cells near the model interface have to be dealt with. The 3D hybrid model is developed on a 3D uniform grid and first results are presented.
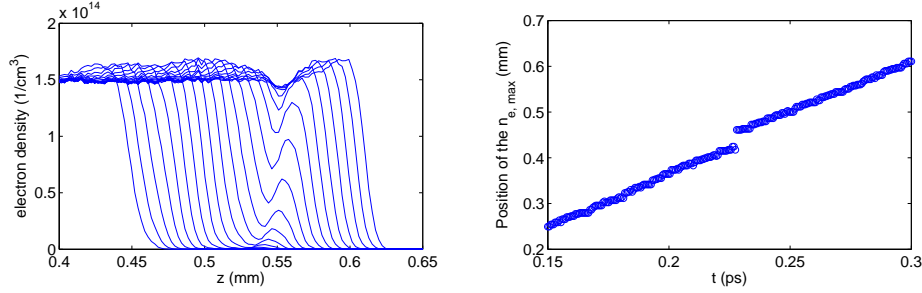
The electron density profiles of a planar front in a particle simulation within several time steps.

The position of the electron density peak as a function of time.

Figure 6.1: *Particle simulation of a negative planar ionization front in a high electric field of $E = -200\ kV/cm$ shows that the front can jump when one high energy electron flies out of the ionization front, relaxes ahead of it, and creates a new local avalanche.*

6.1   Introduction

If the computational cost is not a concern, the ideal streamer simulation is the Monte Carlo particle model that follows the movement of each real electron and includes all necessary collision processes. But in practice, the particle simulation is very much confined by its computational cost (see Sect. 5.2.3). And therefore the fluid model is widely used instead of the particle model.

The fluid model approximates the charged species as continuous densities and neglects the fluctuations due to individual particles. The simulation tools based on the fluid description are well developed [163, 151, 185, 188]. However, the electron energy distribution in the ionization front with its long tail at high energies may lead to a number of physical phenomena that can not be studied by the fluid model.

An example is shown in Fig. 6.1. A 1D particle simulation for a planar ionization front in nitrogen with a transversal area of $9.2 \times 9.2\ \mu m^2$ has been done in a field as high as $E^+ = 200$ kV/cm. The figure shows that the front moves more or less uniformly, until it eventually jumps forward. This jump is caused by a rare event: a single electron gains so much energy that it runs away from the front and creates a new avalanche ahead of it. The front edge of the new avalanche eventually becomes the front edge of the front after the jump.

Aiming at following these high energy electrons in a fully simulated streamer, a 3D hybrid model has to be developed. In the hybrid model, fluid or particle model

will be applied adaptively in suitable regions, which means: i) the model represents the correct physics, ii) high energy particle will be included in the particle region, and iii) the model is computationally as efficient as possible.

The interaction of two models is realized through the well know "buffer region" technique which has been employed in hybrid computations for air flow [251, 237, 86, 9, 10, 6, 232], liquid flow [180, 102, 63], and also in small scale solid systems [219, 211, 253]. A similar method that is more suitable for streamer simulations has been implemented and tested for planar fronts in Sects. 3 and 4. However, the complexity of the 3D geometry brings new challenges in finding the proper position for the model interface and in realizing the interaction between particle and fluid model.

6.2 Construction of the 3D hybrid model

In the 3D hybrid model, the particle model is the same as we discussed in Chap. 5 and the fluid model is the 3D version of the extended fluid model present in Sect. 4.2. The simulations are carried out in a domain of $x \in$ [-0.29 0.29] mm, $y \in$[-0.29 0.29] mm and $z \in$ [0 1.17] mm, that is represented by a uniform grid of $256 \times 256 \times 512$ grid points with the cell length $\Delta x = \Delta y = \Delta z = 2.3$ μm. The time step is $\Delta t = 3 \times 10^{-13}$ s = 0.3 ps.

6.2.1 From planar front to 3D streamer

The coupling of fluid and particle model was first realized in a planar front as discussed in Chapters 3 and 4. The relation between the full 3D streamer and the planar front was presented in Fig. 2.1. The planar front is obtained as a column across the ionization front with a small area in the transversal direction. The area is small enough that the curvature of the ionization front can be neglected and that the particle densities and the electric field do not vary much within such small region in the transversal direction.

The 3D streamer can be decomposed as many such volumes crossing the ionization front with small transversal area. And for each of them, the coupling methods for the planar front, such as the determination of the position of model interface and the construction of the buffer region, can also be applied.

When we apply the hybrid coupling scheme that was tested for a planar front, to the 3D hybrid calculation, the procedure is similar. At the beginning of a hybrid time step, we first set the position of the model interface and then the buffer region is constructed. The position of the model interface and the length of the buffer region of one column shall depend on the electron density and electric field profiles within this column.

Additional problems appear due to differences between a planar front and a column within a real 3D problem. For example, in a planar front, only one position for the model interface needs to be found; in 3D, the model interface of one column will influence the buffer regions of all columns around it. A strongly fluctuating model interface in some region will create large buffer regions and dramatically increase the computation cost. Also in a planar front, the model interface is a straight line and electrons crossing it will contribute to the density flux; in 3D, the shape of the model interface is more complicated, and crossing electrons need to be counted carefully.

6.2.2   The position of the model interface

The electrons inside of the streamer channel are very dense, around 10^{14} to $10^{15}/\text{cm}^3$. To constrain the computational costs, the fluid model will be used as much as possible in regions populated by electrons. The application of the fluid model is mainly limited by its deviation from the particle model at large density gradients and by our physical interest in high energy electrons.

We have compared the extended fluid model with the particle model in Sect. 4.2. The positions of the model interface in the hybrid model has been tested in both Chap. 3 and Sect. 4.3.3 where different fluid models are used. Both cases suggest that the particle model should cover at least part of the ionization front where the electron density gradient is large. To investigate run-away electrons and other phenomena related to high electron energies, the particle model should cover the region where most electrons with high energies are produced.

In Fig. 6.2, we show a negative streamer followed by a pure particle model after 0.306 ns of simulation time in a field of -100 kV/cm. The simulation starts from 100 pairs of electrons and ions. The discharge is still in the transition from avalanche to streamer, but there are already 15 million electrons in the particle list. Assuming that for this particle number the computation should switch from particle to hybrid model, the proper model interface now needs to be located. The figure shows the electron density (upper left), charge density (upper right), electric field (lower left) and the mean electron energy (lower right) at this moment.

The model interface is only needed within the region that is crossed by the streamer. The simulation domain is normally taken as much larger than length and width of the streamers in order to avoid perturbations of the electric field by unphysical boundaries. The streamer only passes through part of the simulation domain and leaves most of the space empty of ionization. The density model is more efficient than the particle model only in cells with many electrons, where the fluid model can approximate them as a density rather than calculating position and
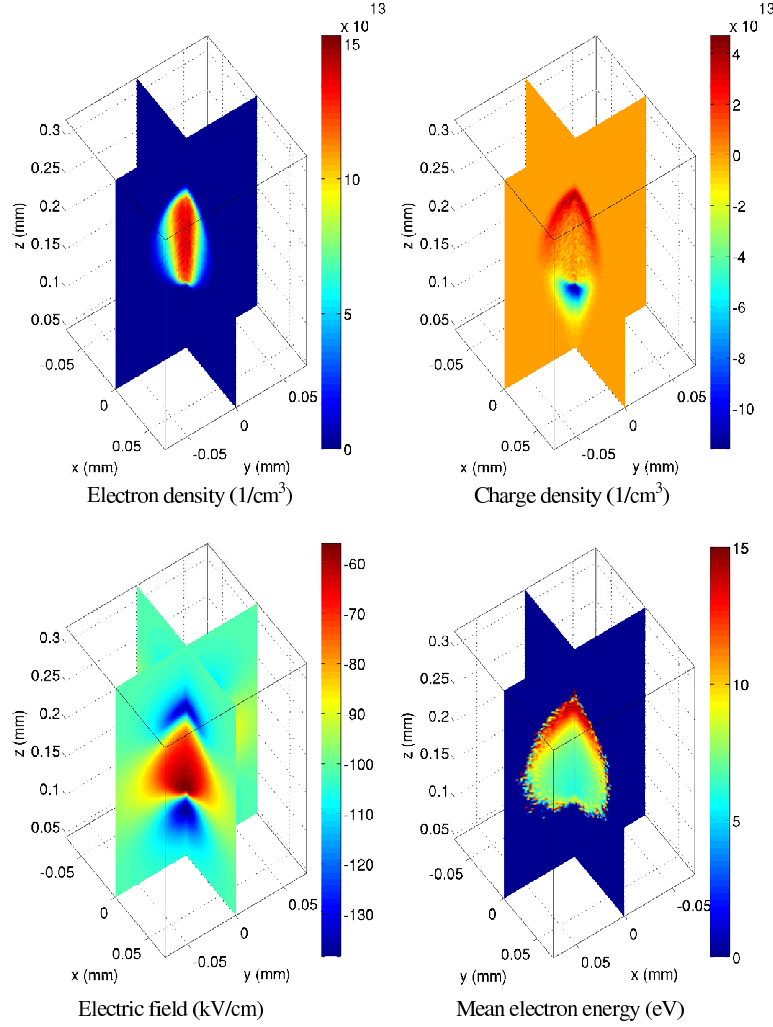
Figure 6.2: *We show a negative streamer with 1.5×10^7 electrons in a particle simulation in a field of -100 kV/cm. To transfer from the pure particle simulation to a hybrid simulation, we need to find the proper model interface. Here we present the following quantities which may be important for determining the model interface: the electron density (upper left), charge density (upper right), electric field (lower left) and the mean electron energy (lower right).*

velocity of all electrons. But for the large ionization free volume in the simulation domain, there is no efficiency problem. Furthermore, if the fluid model is applied in cells where rarely an electron is present, the probability that an electron might be

present, is treated as a very low electron density, which leads to wrong statistics and unphysical predictions. (We remark that in the fluid model developed in Amsterdam, the density is put to zero, if it drops below a threshold [163].) In our hybrid model, the particle model is applied in this electron free region.

In a 3D streamer simulation, each column of cells from bottom $z = 0$ to top $z = 1.1776$ mm with a width of one cell can be considered as a planar front, but differences remain. For example, in a planar front that propagates into a time independent electric field E^+, the field inside the streamer E^- vanishes, while in general, both fields are nonvanishing and varying as shown in Fig. 6.2. Furthermore, in 3D, E^+ is the maximal field ahead of the streamer and it decreases in the direction of streamer propagation rather than being constant as ahead of a planar front. Therefore, if we determine the model interface by $E = y\,E^+$ as in the planar front, such an E may not exist since if it is smaller than E^-.

Interface position according to the density

To find the proper interface position, in Fig. 6.3 we look at a 2D cross section of the 3D streamer. In the upper panel, we show a contour plot of electron densities within the cells in the x-z plane where $y = 0$. The electron densities decrease from the center of the streamer $x = 0$ to the side. In the lower panel, we show the electron densities in each cell-column of the upper 2D plot. The maximal densities of the curves for the cell-columns decrease from the center $x = 0$ to the edge of the simulated space $|\,x\,| = 0.29$. Each column or curve needs a proper position for the model interface.

For the planar front, we have suggested that the model interface should cover the complete density decay region or a certain part of it, depending on the field ahead of the front. Although we know that the model interface should be placed in the density decay region, it is not easy to identify it in the cell-column case. Here we would like to discuss another difference between a planar front and a cell-column in 3D. A planar front physically zooms into a column of the streamer with a small area in the transversal direction, but for the simulation, the area then can be enlarged to suppress fluctuations by averaging in the transversal direction, while the physical results stay the same. This is something we can not do for the cell-column in 3D. The density decay region can be identified quite easily in a planar front since the density peak is a clear starting point for the density decay. In the lower panel of Fig. 6.3, we marked the maximal density $n_{e,max}$ with a ″+″ for each cell-column. The density peaks are scattered in a rather large range due to density fluctuations. Another possible criterion for the density decay region is the density gradient $\partial n_e/\partial z$, but again the strong fluctuations make it difficult to evaluate it.

In general, we would like the model interfaces of all cell-columns to lie within a

Electron density contour plot $(1/cm^3)$

Electron densities in each cell-column $(1/cm^3)$
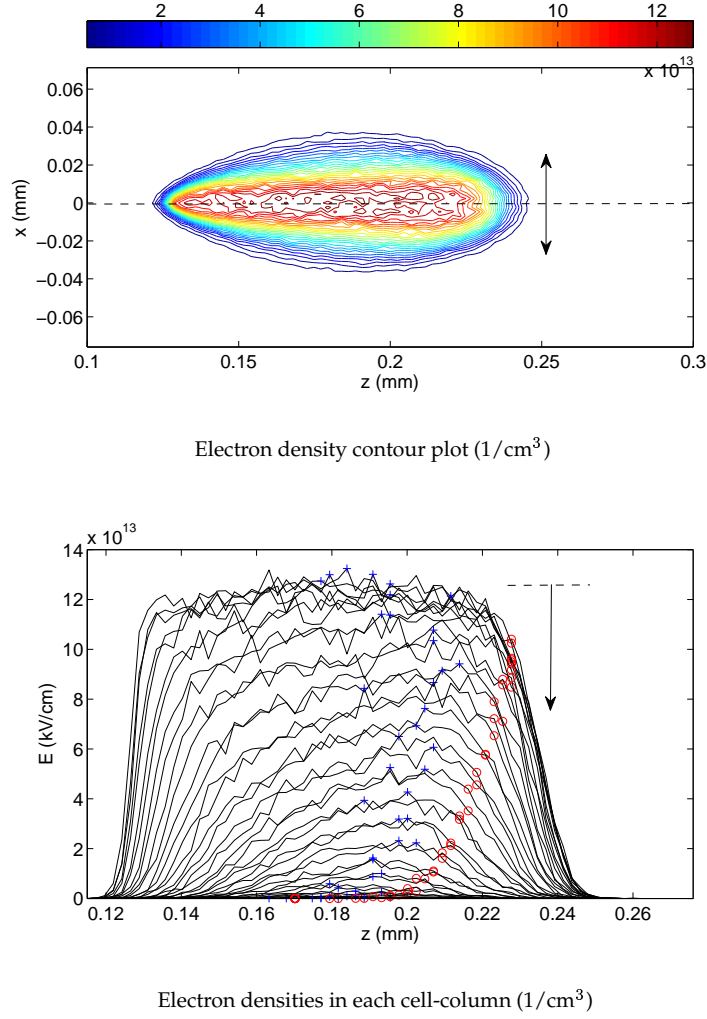
Figure 6.3: *In the upper panel we show a contour plot of the electron density in the x-z plane with $y = 0$. In the lower panel we show the electron densities in each cell-column as a function of z.*

smooth surface rather than fluctuating widely since this enhances the computational costs. A fluctuating model interface can require extra buffer regions which results in more electrons to be followed by the particle model, and it will create a large area of the model interface in the transversal directions where the motions of all electrons
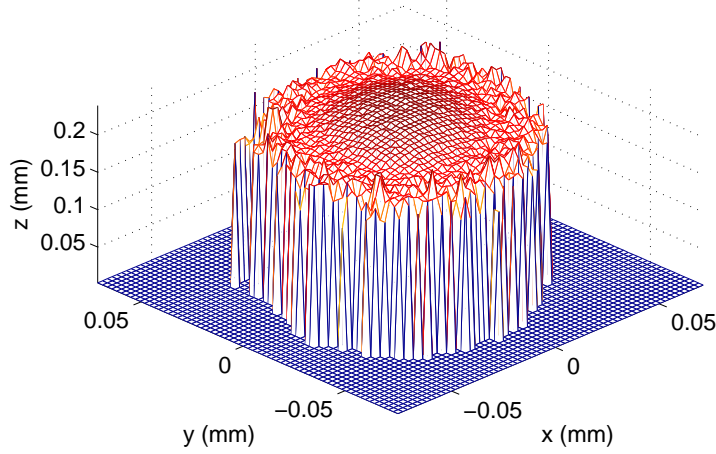
Figure 6.4: *The position of model interfaces at $n_e = 0.7 \, n_{e,max}$ along each cell-column. Far outside of the streamer where no free electrons and ions exist, the particle model is applied and the model interface is set at $z = 0$. In the center of the streamer, the interfaces are rather smooth, the fluctuations appear at the side of streamer.*

close to this large model interface have to be traced. From this point of view, it is not a good idea to relate the position of the model interface to the density peak.

In Fig. 6.3, we also mark the level $n_e = x \, n_{e,max}$ where $x = 0.7$ with "o". Although the density peak $n_{e,max}$ fluctuates a lot on z, the level $n_e = 0.7 \, n_{e,max}$ in the density decay region is much smoother, at least in the center of the streamer where $n_{e,max}$ is large enough. For planar fronts in fields between 75 and 175 kV/cm, a hybrid computation with a model interface at the level $n_e = 0.7 \, n_{e,max}$ deviates from the particle model by not more than 3% according to Sect. 4.4.

Fig. 6.4 shows the positions of the model interfaces at the level $n_e = 0.7 \, n_{e,max}$ within each cell column in the 3D particle simulation. The model interface is set to $n_e = 0.7 \, n_{e,max}$ only when $n_{e,max} > c$, where c corresponds to a density of at least one electron in a cell. It means that we split a cell-column into particle and fluid region only if it contains electrons; in the large area without electrons, the particle model is applied. The model interface is a rather smooth surface in the center where $n_{e,max}$ is comparably large, and it fluctuates strongly where $n_{e,max}$ is small. Even interface islands can be created where a few electrons have flied out of the channel. Therefore again a large buffer region will be created that extends the particle model far back into the high density region of the streamer channel.

A possible solution is to find a fit formula for the interface position near the streamer center and to extrapolate it to the side to calculate the interface position even if no electron exists in that cell-column. But besides concerns on the asymmetry of the density over the radius and on the difficulties of fitting, the interface position at the streamer side would not depend on local properties in this procedure, but on the fit to the streamer center; therefore it could happen that the complete ionization front at the side is included in the fluid region. Although the side of the streamer is less important for streamer propagation, branching and production of run-away electrons, it is not recommendable to neglect all the microscopic physics there.

Interface position according to the field

In the planar hybrid calculation, also an interface criterion depending on the field level $E = y\,E^+$ was tested. In a planar front, there is a clear correlation between the local electric field and the electron density, and the electric field is always more smooth and fluctuates less than the electron densities. The relation between particle density and electric field is not as clear in 3D, but we tried a field dependent criterion to avoid the density fluctuations.

The upper panel in Fig. 6.5 shows the electric field as a function of z for $y = 0$ and several values of x. On the streamer axis $x = 0$, the field is most strongly enhanced in the head and most suppressed in the channel. From the center to the side, the field variation along z decreases, and the field tends to a constant far from the streamer. We marked the position of the maximal density $n_{e,max}$ with "+" and the density based interface criterion $n_e = 0.7\,n_{e,max}$ with "o" at the corresponding electric field. They are also plotted in the lower panel of Fig. 6.5 together with the position of the maximal electric field strength E^+ (marked with "*"), and the field based interface criterion $0.85\,E^+$. As the figure shows, we found the field criterion for the model interface to agree well with the density criterion.

Using $E = 0.85\,E^+$ as a criterion for the position of the model interface may create a smoother surface. But at the side of the streamer where the field varies less than in the center, a level with $E = 0.85\,E^+$ may not exist in cell-columns where electrons are still present. Because there are only few electrons which occasionally fly out of the channel, we leave them to the fluid model. Therefore from the point where the level $E = 0.85\,E^+$ ceases to exist, the model interface is extended several cells outwards to include all particles at the streamer side into the fluid region; the resulting interface is shown in Fig. 6.6.

At the streamer side, we also add one or two extra cells for the density diffusion in the fluid calculation. In the particle model, the electron is discrete and the electron density is always $n * c$, where c is the density of only one electron per cell and n is
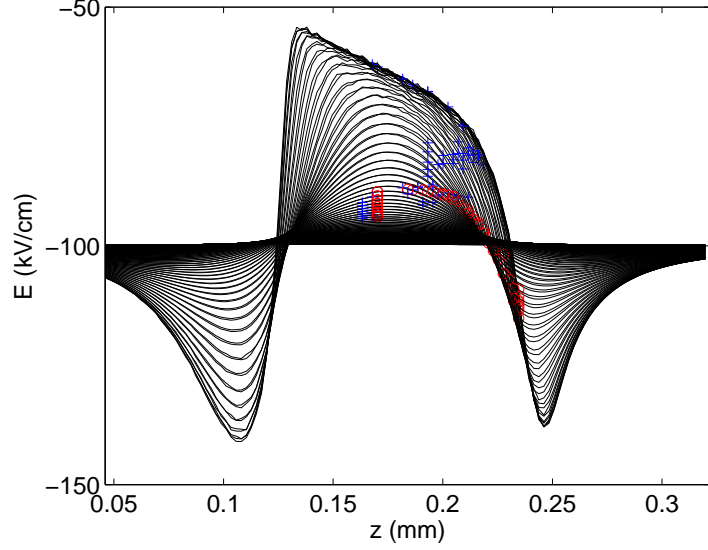
Electric field
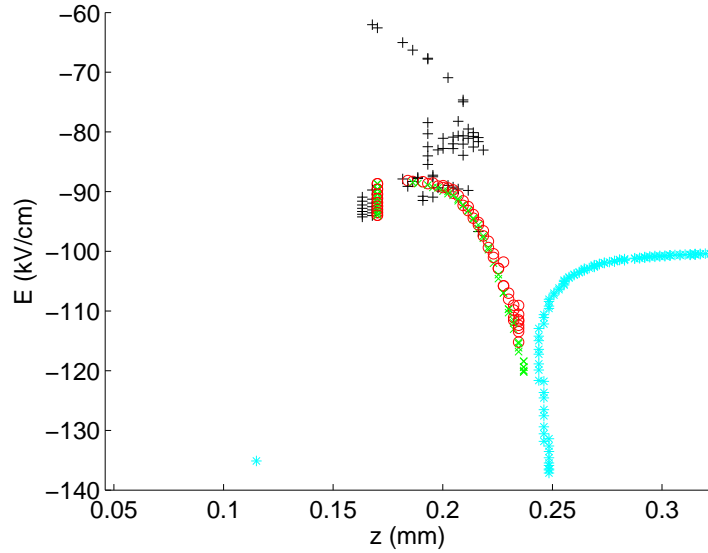
Positions of $n_{e,max}$, $0.7n_{e,max}$, E^+, and $0.85\,E^+$

Figure 6.5: *In the upper panel we show the electric field along each cell-column for several values of x with $y = 0$, as well as the position of $n_{e,max}$ (marked with "+") and of $0.7n_{e,max}$ (marked with "o") indicated on the height of the local field. In the lower panel we zoom into the interesting region and remove the lines. We again show the position of $n_{e,max}$ (marked with "+") and of $0.7n_{e,max}$ (marked with "o"), and we add E^+ (marked with "*"), and $0.85\,E^+$ (marked with "×") for each cell-column.*
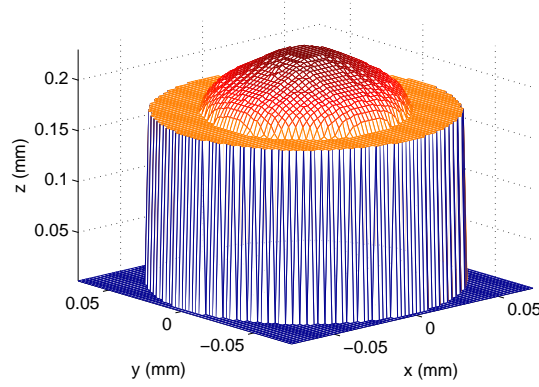
Figure 6.6: *The position of the model interface at $E = 0.85\ E^+$ in 3D.*

an integer. But in the fluid calculation, diffusion can fill the entire fluid region with a small $n_e > 0$. To avoid a continuous expansion of the fluid region to the side, the fluid electron density is set to zero if it drops below c.

6.2.3 The construction of the buffer region.

Once the position of the model interface is determined, the buffer region is created by extending the particle region several cells back into the fluid region. Here we set the length of the buffer region as 3 cells in the z-direction and 2 cells in x- and y-direction (see Table 4.2).

It is important that for any cell face, cell edge and cell corner shared by the particle region and the fluid region, a buffer region is built in the fluid region. A direct contact of particle and fluid model without a buffer region can cause electron leaking, which creates loss of mass and charge.

The so called "corner problem" is a technical but important issue when calculating the electron flux in the hybrid model. When an electron passes from the particle region into the fluid region or vice versa, it contributes to the flux on the cell face if the cell is in the fluid region. The cell face is not necessarily the model interface between particle and fluid region. A 2D example is shown in Fig. 6.7 to illustrate the problem. The particle region is at the upper right and the fluid region is in the lower left corner, the particle region extends into the fluid region by 2 cells in all directions and creates a buffer region. As illustrated in Fig. 6.7, when an electron flies from cell "a1" to "b1", it contributes to the flux on the model interface at cell face "a1↔
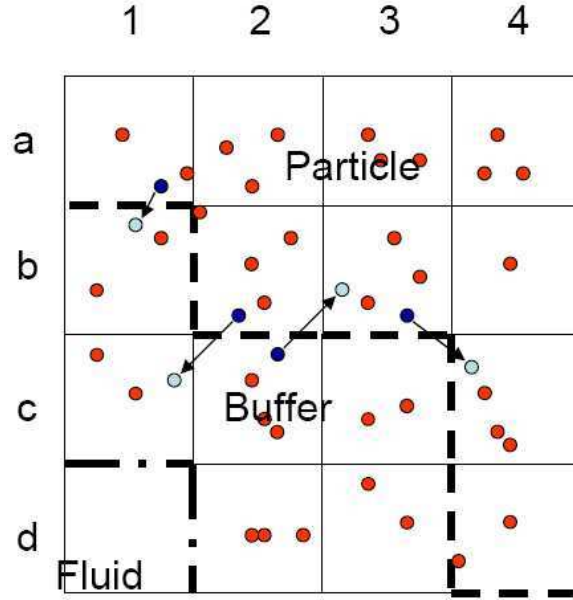
Figure 6.7: *Particle and fluid cells near the model interface.*

b1". A more complicated case occurs when an electron flies from cell "b2" to "c1",
it contributes not only to the model interface at cell face "b2↔ c2", but also to the
cell face "c1↔ c2". On the other hand, when the electron flies from cell "c2" to "b3",
it only contributes to the model interface at cell face "b2 ↔ c2". This example illus-
trates that fluxes must be evaluated where a particle crosses the interface, while the
region where the electron moves into is to be recognized. Finally, consider that the
electron flies from "b3" to "c4"; it flies over two model interfaces, but in the model
it contributes to neither of them since there is no mass change in the fluid region
because $\Delta x = \Delta y$.

Having described the procedure for locating the model interface and the buffer
region, we now present the splitting when the 3D simulation is transferred from
the particle to the hybrid model. In Fig. 6.8, we show electron density (upper left),
charge density (upper right), electric field (lower left) and mean electron energy
(lower right) with the model interface and the buffer region included. Note that the
middle row of Fig. 6.2 and Fig. 6.8 are based on the data of the same simulation at
the same moment.

After splitting into particle and fluid region with $E = 0.85\ E^+$, 12 million elec-
trons which are neither in the particle nor in the buffer region are removed from the
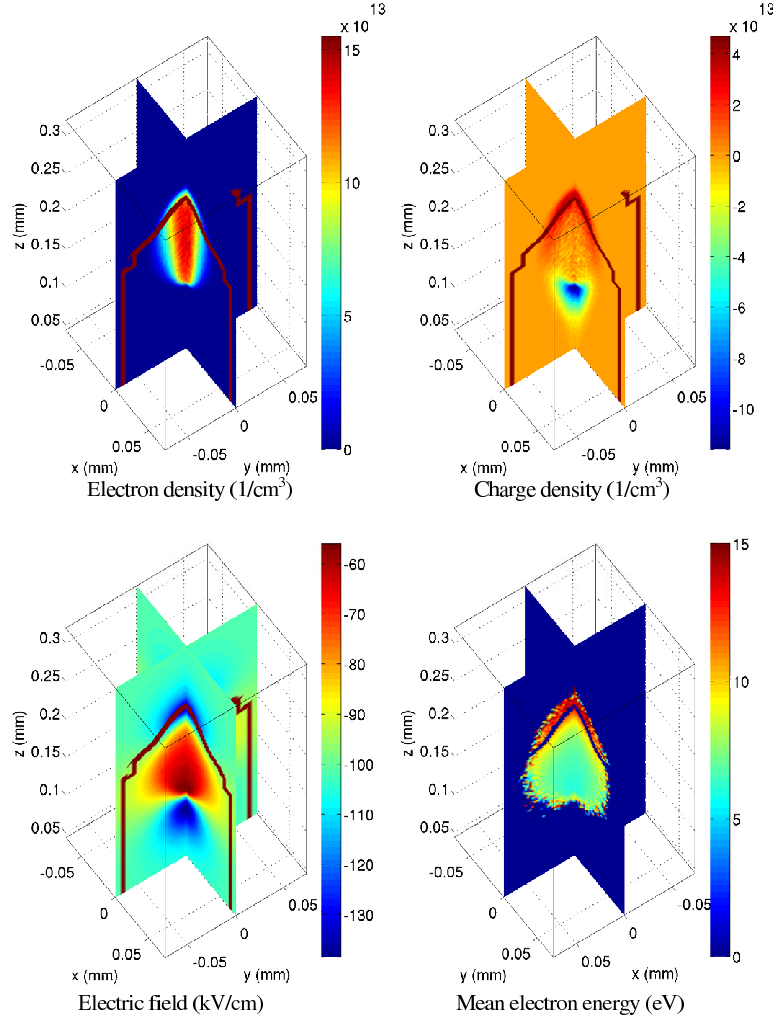
Figure 6.8: *Electron density (upper left), charge density (upper right), electric field (lower left) and the electron temperature (lower right) are presented with the model interface and buffer region marked.*

particle list and transferred into particle densities in the fluid region, while 3 million electrons remain in the ionization front. The splitting leaves most of the ionization front to the particle model; it is also remarkable that the majority of the high energy electrons remains in the particle list which gives a good beginning for the study of run-away electrons.

6.3   Simulation results and discussion

Having presented the details of the coupling techniques, here we present the hybrid simulation results with the model interface located according to the field criterion $E = 0.85\,E^+$ and with 3 buffer cells in the z-direction and 2 cells in x- and y-direction. In Fig. 6.9, we show the simulated streamer in a homogeneous background field of -100 kV/cm after 200 (upper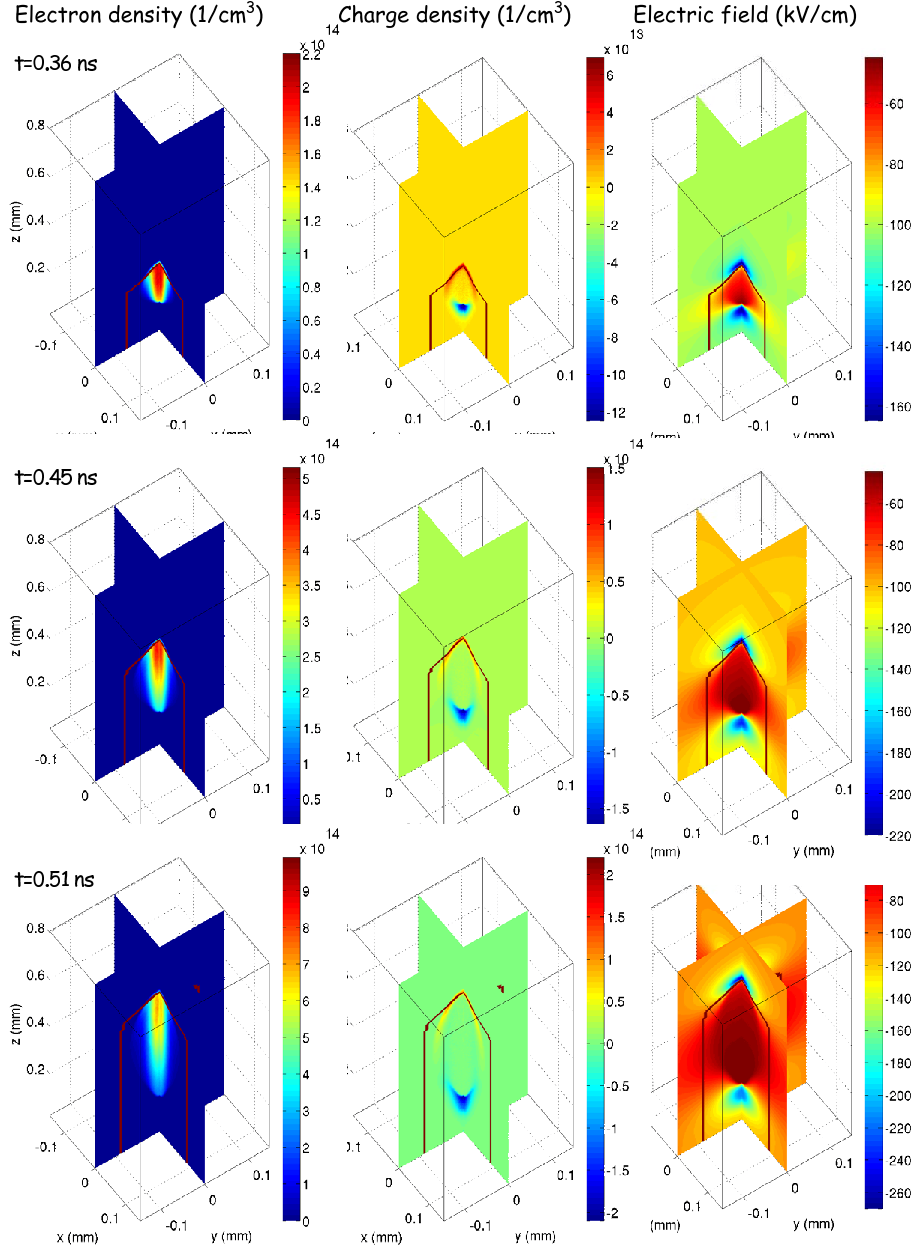 row), 500 (middle row), and 700 Δt (lower row) of the hybrid calculation, which corresponds to simulation times of about 0.36 ns, 0.45 ns and 0.51 ns; the switching from the pure particle simulation to the hybrid simulation is at 0.306 ns. The streamer is characterized by electron density (left), charge density (middle), and electric field (right). The location of the buffer region is marked in red.

At the simulation times 0.36 ns, 0.45 ns and 0.51 ns, there are in total 5×10^7, 2.5×10^8, and 7×10^8 electrons in fluid and particle model together, and about 4.5×10^6, 7×10^6, and 15×10^6 electrons are followed by the particle model; this is about $1/11$, $1/35$ and $1/47$ of the total electron number. The electric field enhancement continue to increase. This results in a higher electron peak and more electrons are included in the particle region. Even with the model interface moving together with the ionization front, more electrons are included in the particle region as the field enhancement and consequently the electron density peak increase.

Compared to the number of electrons in the 3D classical fluid simulation, that are 2.2×10^8 and 4.8×10^8 at times 0.48 ns and 0.57 ns, the hybrid model produces more electrons within a shorter time. The 3D comparison agrees with the comparison results of the planar front where the electron and ion densities behind the ionization front are lower in the classical fluid model when the field is above 50 kV/cm.

While a rather good resolution is needed at the streamer ionization front, the simulation needs to keep their outer boundaries far from the streamer to avoid artifacts in the electric field calculation. The main computation and storage costs in this simulation are not only for updating the electron positions and velocities in the particle model, but also for the calculation of the particle densities and potentials at the grid points. An adaptive grid refinement technique developed by Montijn, Hundsdorfer and Ebert [162, 163] for fluid modeling of streamers on a 2D radially symmetrical grid has been proven to be a powerful tool for the multi-scale problem where different resolution is need in different spatial regions. To simulate the streamer propagation within larger regions and with higher efficiency, the 3D spatially hybrid model needs to integrate the grid refinement.

Figure 6.9: *The 3D simulation results of the hybrid model after 200 (upper row), 500 (middle row), and 700 Δt (lower row) after switching from the pure particle simulation to the hybrid calculation, or after 0.36 ns, 0.45 ns and 0.51 ns of the full simulation. The streamer properties are characterized by electron density (left), charge density (middle), and electric field (right) on two orthogonal planes that intersect with the 3D structure; the location of the buffer region is marked in red.*

Chapter 7

Inception of positive streamers from needle electrodes

The observed electric fields in thunderclouds are generally too weak to initiate the atmosphere's electrical breakdown.

A.V. Gurevich and K.P. Zybin

In contrast to the previous chapters, here we discuss the inception process of streamers near a needle electrode. The inception of streamers is an important and little studied problem both in nature and in the laboratory. Focussing on positive streamers produced in the laboratory, the particle model is used to follow a group of free electrons with an initial density of $10^3/\text{cm}^3$ near a needle electrode which is simulated by a charge simulation method.

7.1   Introduction

The inception process of lightning is presently under heavy debate. The conventional breakdown as taught in textbooks originates from free electrons moving and being accelerated in an electric field. Electrons collide with neutral particles on their path. Electrons with sufficiently high energy (about 10-20 eV) are able to ionize the neutrals and to create new electron-ion pairs. Electrons with lower energies disappear when they attach to neutrals or recombine with the ionized molecules or atoms in the air. A conventional avalanche can start only if the electric field exceeds a threshold E_k such that the generation rate of new electrons is larger than the attachment and recombination rate. In air at atmospheric pressure, literature values for E_k range from $\simeq$ 20 kV/cm [100] to 32 kV/cm [204, 85]. The threshold field is approximately proportional to the air density and decreases with increasing altitude. But even after correcting for the lower density, all electric field measurements in thunderclouds reveal values less than those needed [85].

Furthermore terrestrial γ-ray flashes were recently observed from satellites [83] and found to be correlated with thunderclouds, and γ- or X-rays are also observed in rocket-triggered lightning experiments [69]. Therefore a growing group of researchers search an explanation of such lightning events in the so called run-away breakdown. The relativistic run-away breakdown theory argues that the discharge is triggered by MeV electrons produced by cosmic-ray showers, and these MeV electrons can cause a breakdown in a lower electric field.

The run-away breakdown and the related measurements of electric fields, radio pulses, X-ray and γ-ray bursts are of high interest, especially for geophysicists. But there are also other possibilities. X-rays and γ-rays have also been observed in long spark experiments in the laboratory [174], which indicates that MeV electrons and consecutive Bremsstrahlung radiation can also be produced by the discharge process itself. And the cosmic rays are a possible, but not a necessary condition for their appearance. Our suggestion for the origin of x-ray bursts in laboratory experiments is that the strongly enhanced field at the streamer head accelerates the electrons, and that the high energy electrons are produced in some part of the streamer zone ahead of a spark or lightning leader. To study the possible generation of run-away electrons produced by the streamers, we are developing the 3D spatially hybrid model as discussed in Chapter 6.

The electric fields in thunderclouds are normally measured by balloons [153] between the cloud and the ground and also within the cloud. However, the cloud microphysics may play a role in creating a sufficient field and initiate the discharge. There are large numbers of charged water droplets, ice crystals, graupel and dusty particles which collide and transfer charges between each other. Sharp edges of

such particles can create strong local fields; in this way they could be functioning actually in a quite similar manner as a needle electrode in laboratory experiments. Field measurements inside thunderclouds by balloons do not resolve such local field enhancements.

If one or a few electrons happen to be near this natural needle electrode, they may create an avalanche around the needle. The electric field strength drops quickly away from the tip of the needle, therefore the electric field drops below the critical value E_k within a small distance from the needle tip. But if the cloud particle is sufficiently charged or if a conducting particle with a sharp tip is in a strong background field, a sufficiently strong field can be created locally, and enough electrons and ions can be produced for an avalanche to streamer transition before the field decays to a level below E_k. The streamer can then propagate with the self-generated field even if the large scale external field is below E_k, and a discharge can occur.

Briels, Nijdam, Winands and their Ph.D. supervisors have conducted a series of streamer experiments in Eindhoven [258, 38, 260, 259, 36, 40, 41, 39, 37, 179, 178]. In particular, in [37] both negative and positive streamers were studied in different background gases between electrodes in needle-to-plane geometry. It was found that positive streamers in general start at a lower voltage between the electrodes than negative streamers, that is, the voltage threshold for the negative streamers is higher than for the positive ones in the same experiment.

Another open problem is the inception jitter of positive streamers. If the voltage is above the threshold for negative streamers, the discharge starts within nanoseconds or less, while for a positive streamer for a voltage just above the inception threshold, the delay can last up to several μs, which makes it much more difficult to take time resolved photos than for negative streamers.

The inception of a discharge is also of interest for the start-up of high pressure discharge lamps which is influenced not only by the electrode shape, but also by dielectric walls and the initial background ionization.

As a contribution to all these questions, a preliminary model has been developed that can describe the electron dynamics near a needle electrode. The model follows the electrons with the particle model and the electrodes are simulated with a so called charge simulation method.

7.2 Simulation of the electrodes

The simulation is carried out with a particle model in a needle-to-plane electrode setup. Between the electrodes, normal air, with 78% nitrogen, 21% oxygen and 1% argon, is filled in at standard temperature and pressure. Attachment is taken into

The   experimental   The needle electrode.
electrode geometry.
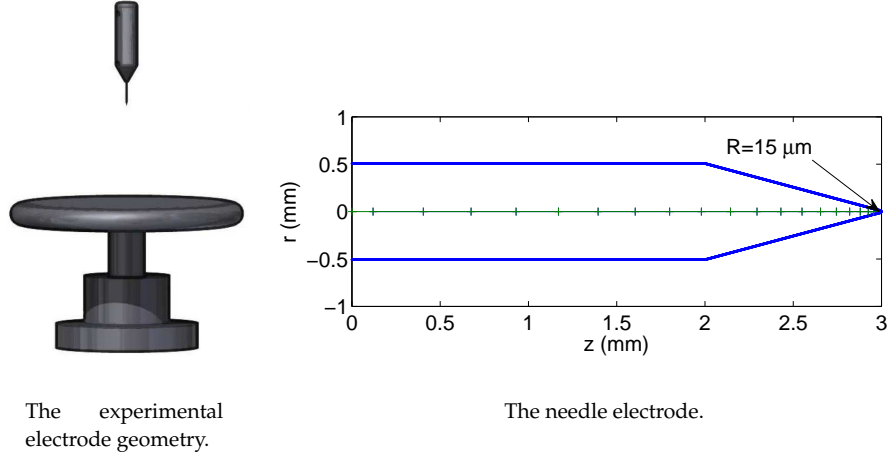
Figure 7.1: *The needle-to-plane electrode setup for the experiments in the laboratory is shown on the left (the picture is taken from Nijdam [178]). The shape of the needle electrode and the charge elements inside the electrode in our simulation are shown in the right plot.*

account, but photoionization is not. The simulation is carried out in a cubic of size $7.4 \times 7.4 \times 11$ mm^3.

We simulate the needle of the laboratory experiments described in [38, 36, 40, 41]. It is conical with spherical tip and cylindrical shank. The needle is set to 3 mm length and the half sphere at the tip has a radius of 15 μm. In Fig. 7.1, we show both the experimental setup in the laboratory [178] (left) and the shape of the needle electrode in the simulation (right). In the simulation, a positive voltage will be applied to the needle while a planar cathode is put about 1.1 cm away from the needle.

The simulation is carried out with the particle model. The calculation of the electric field requires the solution of the Laplace or Poisson equation with appropriate boundary conditions. This can be done with various numerical methods such as finite differences or finite elements though an accurate solution for a streamer is already quite demanding [163, 149]. However, when introducing an electrode into the simulation domain, the physical system is becoming even more complex. The solution needs to realize an equipotential electrode with a complicated shape. In this section, we present a method to couple the charge simulation method for the electrode with the FISHPACK subroutines, such that the equipotential electrode is represented by the charge simulation method and the field outside the electrode is calculated by FISHPACK.

7.2.1 Charge simulation method

The basic principle of the charge simulation method [225, 123, 152, 2, 3] is very simple. If several discrete charges of any type (point, line, or ring, for instance) are present in a region, the electrostatic potential in a point $\mathbf{r}$ (that does not carry a charge) can be found by summing up the potentials from the individual charges. Let Q_j, $j = 1, \ldots, n$ be the charge in a point $\mathbf{r}_j$, and let ϕ_i be the potential at a point $\mathbf{r}_i$ within the space, then we have

$$\phi_i = \sum_{j=1}^{n} P_{ij} Q_j, \tag{7.1}$$

where P_{ij} are the potential coefficients in the absence of external boundaries according to classical electrostatics as summarized in Appendix C. Thus once the types of charges and their locations are defined, it is possible to relate ϕ_i and Q_j quantitatively at any boundary point. In the charge simulation method, the simulation charges are placed inside an equipotential surface such as an electrode. If the boundary point $\mathbf{r}_i$ is located on the surface of a conductor, the ϕ_i at this contour point is set to the conductor potential ϕ_c. When this procedure is applied to m surface contour points, it leads to an $m \times n$ linear system

$$\mathbf{P} \cdot \mathbf{Q} = \mathbf{\Phi}, \tag{7.2}$$

which has to be solved for the charges $\mathbf{Q}$, where $\mathbf{P} \in \mathbb{R}^{m \times n}$, $\mathbf{Q} \in \mathbb{R}^n$ and $\mathbf{\Phi} \in \mathbb{R}^m$.

Due to the axial symmetry of the investigated needle electrode, the surface charge is simulated by a combination of point and line charges whose positions are fixed. The point charge is put at the tip center and the line charges with different length are distributed behind the point charge. To determine the unknown simulation charges, a set of contour points on the electrode surface is then chosen. And those boundary points are only chosen from the intersection between the electrode and the x-z plane with $y = 0$ due to its axial symmetry.

Error and stability of the charge simulation method solutions depend upon the types, numbers as well as locations of the simulation charges, the locations of the contour points and the complexity of the electrode profiles. For example, for different numbers n of charge elements, normally one chooses the same number of contour points to form a system with n equations for n unknown charges. However, the solutions can be unstable and negative charges may appear inside the positive electrode. In Fig 7.2, we show the charges on the charge elements. We tried 18, 22, 28 line charges and negative charges appear when 28 line charges are used.

To obtain a stable solution, an iterative method can be used to search for a good arrangement of charge elements. However, the high level of freedom in the system
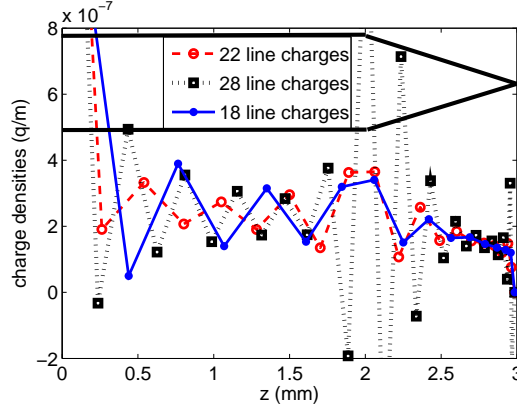
Figure 7.2: *Different arrangements of the simulation elements may generate different charges inside the electrode, even negative ones in a positive electrode.*

makes it difficult to apply the iterative method. Therefore we first fix most of the element positions and optimize the rest. Here we fix the shape of the electrode and the arrangement of the charge elements, and we use a least square error method to find a suitable number of contour points which are evenly distributed along z.

As mentioned above, in the conventional charge simulation method, the number of charge elements is equal to the number of contour points. In the least square error method (LSEM) [225, 152], there are more contour points than charge elements, i.e., $m > n$. The charges are found by minimizing

$$U = \sum_{i}^{m} (\phi_i - \phi_c)^2 \tag{7.3}$$

where ϕ_c is the potential of the electrode and ϕ_i is the potential created by all charges at the ith contour point as in Eq.(7.1). By partially differentiating U with respect to Q_j, and equating to zero, an $n \times n$ system is created

$$\mathbf{D} \cdot \mathbf{Q} = \mathbf{F}, \tag{7.4}$$

where $\mathbf{D} = \mathbf{P}^T\mathbf{P}$ and $\mathbf{F} = \mathbf{P}^T\mathbf{\Phi}$. This is actually Eq. (7.2) multiplied by $\mathbf{P}^T$ on both sides. The LSEM satisfies the boundary conditions at a large number of contour points and is therefore more accurate.

The charge simulation method can still obtain the charges of the fictitious elements for an equipotential electrode when the space charges in the discharge are included. The space charges can be viewed as many point charges at their grid points or they can be approximated by point, line or ring charges. They work together with the charge elements inside the electrode to maintain an equal potential

at the surface of the electrode,

$$\mathbf{P} \cdot \mathbf{Q} = \mathbf{\Phi} - \mathbf{P}_s \cdot \mathbf{Q}_s, \tag{7.5}$$

where $\mathbf{P}_s$ are the potential coefficients of the space charges and $\mathbf{Q}_s$ are the space charge elements.

7.2.2 Electric field calculation

If both the charges on the charge elements inside the electrode and the space charges in the gas discharge are known, we can calculate the potential on any point using Eq. (7.1). However, if a large grid is needed in the simulation, using the charge simulation method to calculate the potential and electric field for each grid point can be numerically very expensive. When potentials on grid points are needed, the 3D FISHPACK subroutine is used to solve the Poisson equations.

To calculate potentials on a grid, the boundary conditions need to be specified for the FISHPACK. At the side of the simulation domain, a Neumann boundary condition is used: $\partial\phi/\partial x = 0$ at $x_0 = -3.7$ and $x_l = 3.7$ mm, and $\partial\phi/\partial y = 0$ at $y_0 = -3.7$ and $y_l = 3.7$ mm. At the boundary $z_0 = 0$ and $z_l = 11$mm, a Dirichlet boundary condition is used. The size of the system is large enough to keep the effect of the lateral Neumann boundary condition small. Therefore, we assume the cathodes is put at $z_l = 11$mm and set $\phi = 0$. Potentials on the boundary points at z_0 is calculated with the charge simulation method using Eq. (7.1), where the influence of both charge elements inside electrode and of the space charge are taken into account. Note that this could be very time consuming if the potential is calculated for each grid point on the lower boundary, while it only needs to be solved with Eq. (7.1) on part of the points if the system is axial symmetric. Once the boundary conditions are set, the fast Poisson solver-FISHPACK is used to solve the Poisson equation on the grid.

However, since the upper boundary and the boundary at the side need to be kept far away, the size of the 3D system is too large to obtain a good resolution around the needle when a uniform grid is used. If we use the cell size $\Delta x = \Delta y = \Delta z = 2.3$ μm as in the previous chapters, the grid has a size of $3200 \times 3200 \times 4800$ which is too large to compute. Therefore adaptive grid refinement has been implemented to calculate the electric field in the whole domain while keeping a high resolution near the tip of the needle electrode.

The refinement strategy for the computation of the electric potential is based on a static regridding approach. The FISHPACK routine will be used on a sequence of nested unifrom grid. The solution on a coarse grid will be used to provide boundary conditions for the grid on the finer level. The refinement criterion is based on an error estimate approach which compares the solution on the grid and the interpola-

tion of the solution on the underlying coarser grid. These approach is explained in full detail in [250, 162, 163].

The computation of the potentials with the space charge is summarized as follows:

1. The fictitious simulation charge inside the electrode together with the space charge in the discharge maintain the needle electrode equipotential. Knowing the position of electrons and ions from the particle model, the fictitious simulation charges are obtained by Eq. (7.5).

2. The potentials of all charges on the grid points of the lower boundary are calculated using Eq. (7.1).

3. The 3D FISHPACK solves the potential on the grid with the given boundary conditions and the electric field is calculated.

4. Electrons in the particle model move and collide with air molecules within this field.

7.3 Simulation results and discussion

7.3.1 Avalanche without space charge induced field

In ambient air, there are typically free electrons with a low density of $10^3/\text{cm}^3$ due to cosmic radiation and radioactivity. The simulation is carried out in a cube of volume of 7.4 mm $\times$ 7.4 mm $\times$ 11 mm $\approx 0.6\text{cm}^3$, and therefore we initially place about 600 electrons at random positions. The needle electrode is located at the bottom of the cube. The potential is set to 10 kV on the needle electrode and to zero on the planar cathode. In Fig. 7.3, we plot the potential and the electric field calculated by the charge simulation method. A strong electric field is created around the anode, especially in the region near the tip of the needle, and it decays rapidly away from the electrode.

The particle model is applied within this electric field to follow the free electrons. With a different random number seed, the initial electrons may appear at different positions within the simulation domain. If an electron runs out of the simulation domain or attaches to a molecule, a new one will be generated randomly, which simulates the free electron density staying constant due to a balance of electron loss by attachment and electron gain due to radiation. In the simulation, one in general has to wait for a while for the ionization avalanche to start and the avalanche can appear anywhere near the needle electrode. In Fig. 7.4, we show the electrons in a particle simulation after 30 ns. Each small circle in the plot stands for one electron

Potential (V)   Electric field (kV/cm)
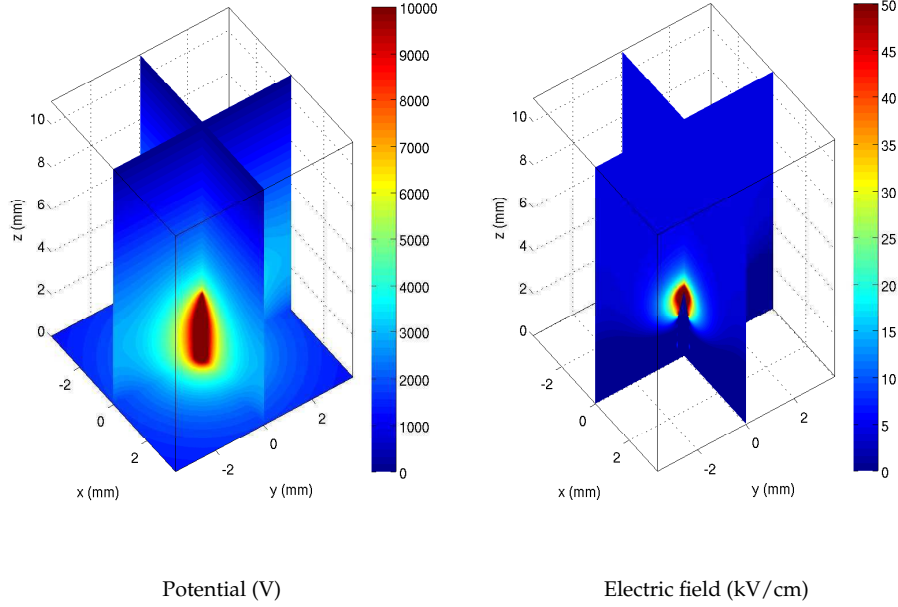
Figure 7.3: *On the left we show the potential when a voltage of 10 kV is applied to the needle electrode, and on the right the electric field is shown.*

chosen randomly from 10 electrons in the particle list. On the right, we zoom in into the region near the electrode; there is one electron swarm near the side of the needle already in the avalanche phase, and another small group of electrons near the tip of the needle is just initiating an avalanche. This simulation illustrates why in laboratory experiments sometimes the streamer initiates not only from the tip of the needle electrode, but also from the side of the needle.

Free electrons move slowly towards the electrode if the electron is not already close to the needle. If electrons get near the needle tip or near an edge where the field is strong enough, an avalanche starts. But for example, 1 μm from the needle tip, the field is 10^3 kV/cm, and 1 mm away from it, it is only 1 kV/cm. If there are electrons within a distance of 1 mm from the needle tip, they can reach the region where the field exceeds the threshold field E_k within a few ns and then create an avalanche. But if the nearest electron is for example 2 mm from the needle tip, on average it needs 0.5 μs to reach the distance of 1 mm.

Once the electrons start the avalanche, since they are moving towards a stronger field, the generation speed of new electrons increases closer to the electrodes. Charge

Electrons after 30 ns of one parti-
cle simulation, every tenth electron is
shown.

Zooming in near the needle elec-
trode
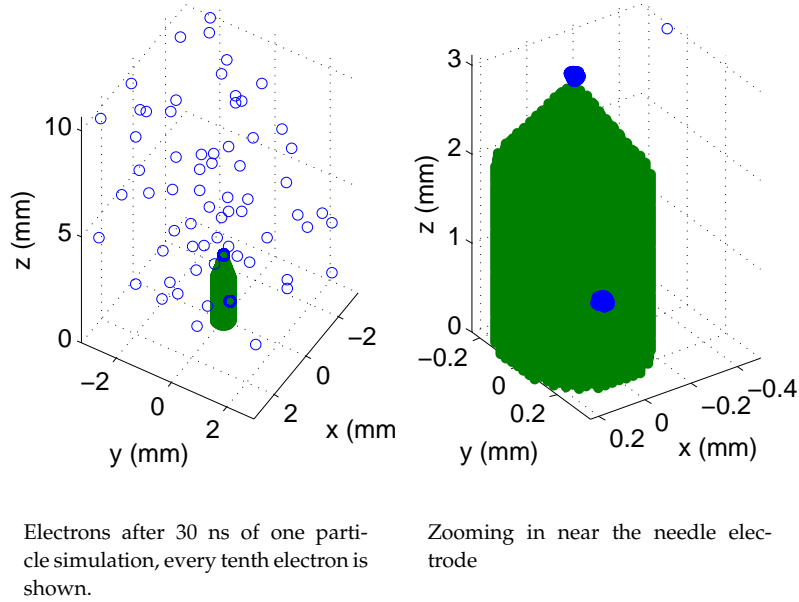
Figure 7.4: *On the left, we show the electrons after 30 ns of a particle simulation. On the right, we zoom in into the region near the electrodes.*

separation may start and a positive charge layer may form at the tail of the avalanche while electrons fly into the electrode. The effects of the space charge induced electric field is important in the inception of positive streamers and needs to be studied.

To start an avalanche near the needle anode, not only the shape of the electrode, but also the density of free electrons and their spatial distribution determines the inception process. The experiment also explains why the positive streamer at low voltage starts with a large jitter while the negative streamer does not. The source of the free electrons plays an important role. For a positive streamer to start, free electrons by chance have to get into the high field region near the electrode tip; this will take some statistically distributed waiting time. In contrast, when a negative streamer starts an avalanche, there are hardly any free electrons in the neighborhood. Actually during the rise time of the voltage, the needle cathode may blow away nearby electrons if there are any. Free electrons for an avalanche can only be generated by the (field) emission from the electrode; we suggest that this is actually the reason why a higher voltage is needed in the case of negative streamers. The shape of the electrode is very important from this point of view, i.e., the sharper the needle, the
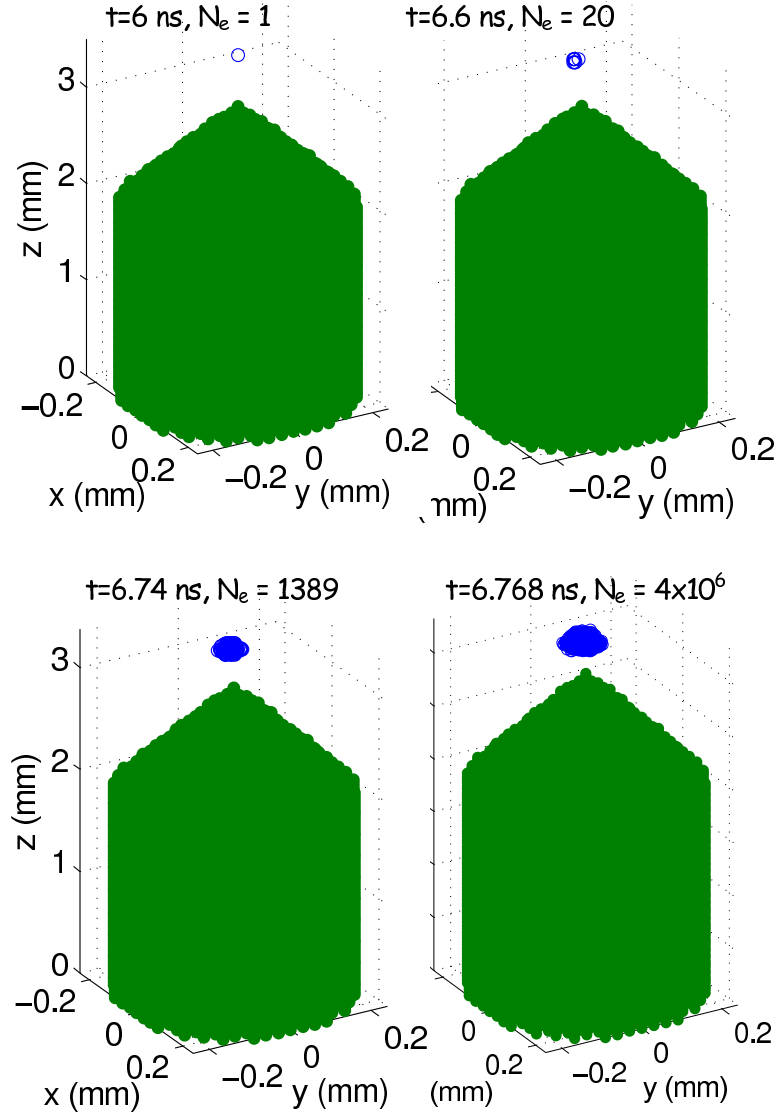
Figure 7.5: *The avalanche process triggered by an electron near the electrode tip.*

easier the electron emission. Once the voltage reaches a threshold and free electrons are released from the cathode, the avalanche starts. We may view the inception of a

lightning discharge in this manner. Ice crystal, graupel, dust, and water droplet or their congregated larger elements inside the thundercloud act like a needle electrode in the lab. If the discharge moves away into a weaker field, the field-enhancement at the streamer head supports the further growth, if the avalanche to streamer transition already has taken place.

7.3.2   Avalanche with the space charge induced field

The charge simulation method with point-line charge elements works well as long as potential and electric field are axially symmetric. But when the space charge is included, it breaks the symmetry. When the axial symmetry is perturbed, ring charge elements can be used together with point and line charge elements. The charge distribution on the ring is variable along the ring, for example, the distribution can be divided into a constant part and several cosinusoidal or sinusoidal harmonics, similar to a Fourier analysis [225, 152]. However, including of ring elements needs much more contour points on the 3D electrode surface to maintain a non-negative solution of Eq. (7.2), which makes it computationally more expensive.

To study how the avalanche starts under the symmetry constraint of our present simulation tool, we put one electron at a distance of 0.5 mm right over the tip of the needle rather than putting 600 electrons at random in our system. Since the streamer will propagate along the axis, the axial symmetry will be more or less conserved when the space charges are included. In this way, only point and line charges are used in the charge simulation method. In Fig. 7.5, we show the electrons at times $t = 6$, 6.6, 6.74 and 6.768 ns after the 20 kV voltage has been applied to the needle anode, the number of the particles at these times are 1, 20, 1389 and about 4 million, respectively.

The calculation of the electric field is rather time consuming when Eq. (7.1) has to be solved for each contour point on the electrode and for the grid points at the boundary. Therefore, we only update the electric field when the number of electrons in the system is above a certain level, for example 2×10^6 in this simulation, and when it has changed significantly, for example when $N_{e,new}/N_e > 0.2$ here, where N_e is the number of electrons in the system and $N_{e,new}$ is the new number of electrons produced since the last calculation of the electric field.

Only the pure particle model has been employed, but light weight super-particles were introduced. Before the simulation stopped, we have 3.2×10^7 electrons in the system, that are represented by 8×10^6 super-particles with the charge of 4 real electrons; at that moment no electron has reached the anode yet. In Fig. 7.6, we show the electric field near a needle electrode (left panal), and zoom into the region right above the tip of the needle (marked with a dashed circle). Comparing the electric
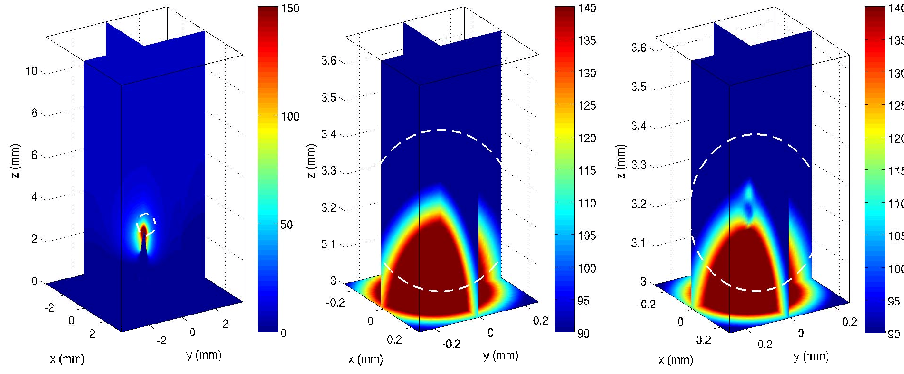
Figure 7.6: *The electric field near a needle electrode is shown in the left panal. The plots in other panals zoom in into the region (marked with dashed circle in the upper-left panal) right above the needle tip. In the middle panal we show the electric field in this region at the beginning of the simulation. And in the right panal we show the field at the end of the simulation. (Note here that the color bar of the electric field in the right column is confined to a region of 90-140 eV to highlight the field change.)*

field at the beginning (middel) and at the end (right) of the simulation, the electric field is obviously changed by the space charges. Comparing to the electric field in the beginning of the simulation, the electric field of 100 kV/cm extends 0.2 mm further from the needle by the space charges. As the discharge develops further, the high field region may extend further and attracts more free electrons.

The simulation is limited by the electron number as it uses a pure particle model. To simulate the development of a full streamer from the avalanche, the hybrid model should be used in the future.

Chapter 8

Conclusion and outlook

The main part of this thesis is devoted to the development of a hybrid model for streamers, where a microscopic particle model is spatially coupled with a macroscopic fluid model.

The hybrid model is developed in a systematical way. The parameters used in the fluid model, the electron mobility, diffusion rate and ionization rate, are first re-derived from particle swarm experiments to make the models consistent for electron swarms in a uniform constant field. The two models are then compared for a planar front in chapter 2. The comparison shows a discrepancy in the particle densities while the velocity is in good agreement. To understand this phenomenom, we studied the mean energies of the electrons at the ionization front and compared this with the underlying assumptions of the fluid model. The approximated energies in the fluid model nicely follow the mean energies in the interior of the ionized region while they are considerably lower in the region where the electron density decreases rapidly. These higher energies in the particle ionization front cause a higher ionization rate in the particle model, and result in higher electron and ion densities behind the front than in the fluid model.

The spatial coupling of the particle model and the fluid model has first been achieved for a planar front in 1D (see chapter. 3). With the model interface moving with the ionization front, a real particle description at the ionization front can be obtained with much lower computational cost than in a full particle model. It was found that the electron and ion densities behind the ionization front vary when the model interface is put at different positions in the ionization front. In general, the particle simulation results can be obtained when the hybrid simulation includes the whole density decay region of the ionization front in the particle region; and the hybrid simulation results tend to be close to the pure fluid results when only the very leading part of the ionization front is included in the particle description.

The first coupling model revealed a deficiency of the fluid model. Electrons in the fluid model are assumed to be in equilibrium with their local electric field, while a non-uniform electron energy distributions is found in a particle swarm simula-

tion in a uniform electric field. By underestimating the electron energy at the front and overestimating the electron energy at the tail of the swarm, the classical fluid model can obtain the same electron density profile as the particle model in a swarm experiment. However, this approach makes the definition of the electron mobilities and the ionization rate of the fluid model inconsistent with the particle model, and can cause problems in the coupling of the two models. Therefore in chapter 4, an extended fluid model which includes a density gradient term is introduced as an alternative to the classical fluid model.

The extended fluid model takes the nonlocal ionization rate into account and defines its transport coefficients coherently with particle swarms. This extended model is first compared with the particle model and the classical fluid model both in swarm and in planar front simulations. Then the hybrid model which couples the extended fluid model and particle model is compared with the particle model at varying fields. For each field, different positions of the model interface and different lengths of the "buffer region" are tested. A table with recommendable values for the position of the model interface and buffer length is then given for use in the 3D hybrid model.

The planar front is a simplified form of the ionization front of streamers, the coupling method for the planar front is therefore applicable in 3D for columns crossing the ionization front with small transversal cross-sections. Although many coupling tests have been done for planar fronts, the complexities of the 3D geometries bring new questions on the proper position of the model interface and the interaction of the two models. In Chapter 6, we present first results of the 3D hybrid simulation. The 3D hybrid model allows a particle description of the high-energy electrons in the ionization front during the streamer stage which can not be reached by a pure particle simulation because of computer limitations; compared to the classical fluid simulation, although the streamer propagation is qualitatively similar, quantities like field enhancement ahead of the streamer and number of electrons differ largely.

Although the main topic of this thesis is spatially hybrid modelling, we present a pure particle simulation in chapter 7, to study the inception of streamers at a needle electrode. The needle is the same as in the laboratory experiments [38, 36]. One observation is that the avalanche can not only start from the tip of the needle, but also from the side of the needle, which corresponds to observations in laboratory experiments. Another observation from our computation model is that even in the early stage of an avalanche, space charges can build up and influence the field near the needle.

We have thus developed a numerical code, which is able to study the kinetics of electrons in both an avalanche phase and at the ionization front during a streamer evolution. It is, however, only a first step towards simulations of more realistic and

complex streamers. In the future, we are planning to add the following features to the hybrid model:

1. The calculation of the electric field and densities in a hybrid model in 3D is a heavy task in both storage and time consumption. Therefore, the hybrid model should include a grid refinement technique in the future. (Note that the grid refinement for the calculation of the electric field has been implemented into the particle model, see chapter 7.)

2. To simulate positive streamers in air, other ionization mechanisms, in particular the photoionization or background ionization should be included in both the fluid model model and the particle model.

3. To follow the high energy electrons in higher energy ranges, the cross sections and the differential cross section for electron energies above 1 keV should be included.

This will allow us to make predictions on the phenomena discussed in the introduction:

1. the inception of streamers near a needle electrode,

2. the primary molecular excitations behind the streamer ionization front,

3. the branching time and structure taking discrete particle fluctuations into account,

4. and the generation of run-away electrons and hard x-ray radiation from a streamer.

Summary

Streamers are non-equilibrium plasma channels that propagate rapidly into a non-ionized medium due to a self-enhanced electric field at their tip. They are widely used in industry, for example, for the treatment of exhaust gasses, ozone generation, cleaning of polluted water, combustion control and in aero-space engineering. Streamers are also found in nature, in sparks or in lightning where a streamer corona creates the path of the lightning leader. In the past 20 years, sprite discharges and blue jets were found above active thunderclouds; sprites are now recognized to be upscaled versions of streamers.

In most cases, streamers have many branches. But understanding formation and underlying physics of the complete dielectric breakdown tree relies on the study of generic features of single streamer channels. The multiscale inner structure of single streamers is mostly studied with a fluid model that approximates the electrons as continuous densities. It consists of continuity equations for plasma species and the Poisson equation for the electric field. The fluid model is presently used to study streamer propagation, branching and interactions with other streamers, electrodes or walls.

On the other hand, physical phenomena where quite few or very energetic electrons play a role, cannot be handled accurately with a fluid model, but require tracing the dynamics of single electrons. Such phenomena are (i) the start-up of streamers from few electrons, (ii) electron density fluctuations during streamer branching, and (iii) the run-away of electrons from a streamer ionization front. (iv) Finally, the thesis shows that in a streamer with high field enhancement, the electron energies in the ionization front are actually higher than in the fluid approximation. As they start the plasma-chemistry inside the streamer channel, tracing the electron energies and collisions with a particle model is important for streamer chemistry as well.

The interplay of energetic electrons with discharges is a current topic in lightning physics; questions concern the origin of Terrestrial Gamma-Ray Flashes (TGFs) observed from satellites above thunderclouds, the origin of X-rays from approaching lightning leaders and from laboratory streamer-leader discharges, and the inception of a lightning stroke inside a thundercloud. Is energetic radiation due to cosmic particles with very high energies that form relativistic avalanches inside the thundercloud? Or can a streamer discharge by itself accelerate ambient electrons to high energies?

To answer these questions, the dynamics of single electrons inside the streamer discharge have to be followed. The particle model deals with the streamer dynamics

at the lowest atomic level and follows the movement of each individual electron. But the thesis shows that the number of electrons to be followed easily exceeds the memory space of a modern computer. As a remedy, superparticles representing many real particles have been introduced for some discharge problems. But the thesis shows that this is not a remedy for streamer simulations as it creates numerical artifacts.

The crucial insight is that in a streamer only the electrons in the high field region at the tip of the streamer channel have to be followed, and not the many electrons in the streamer interior. Therefore, in this thesis a numerical model is developed systematically that follows the dynamics of single electrons in the streamer ionization front while treating the many electrons with low energies in the channel interior with a fluid model.

This approach raises many questions: How can one reach consistency between the particle and the fluid model? Where should the interface between fluid and particle description be placed? How should the so-called buffer region between particle and fluid model be constructed? And after the interface is implemented into a one-dimensional ionization front, how does one implement the scheme in full three dimensions? All these questions are addressed and solved step by step.

The result is a hybrid model that allows one to study the real electron density and energy distribution at the tip of a streamer channel, and consequently the runaway electrons, the start-up of plasma-chemistry and the influence of single particle fluctuations on streamer branching. The last chapter contains a first study of streamer inception from available electrons near a needle electrode. All results can be achieved on a PC within reasonable computation times.

Appendix A
Approximating the ionization level behind the front

In the article [77], Ebert *et al.* have established that for a planar, uniformly propagating front with field independent electron mobility $\mu(E) = $ const. and for vanishing electron diffusion $D(E) = 0$, there is a unique relation between the field ahead of the front E^+, the ionization rate function $\alpha(E)$ and the degree of ionization $n_e^- = n_p^-$ behind the front, namely

$$n_e^- = n_p^- = \frac{\epsilon_0}{e} \int_0^{|E^+|} \alpha(e) \, de \qquad (A.1)$$

in dimensional units.

Such a simple identity does not hold for the full fluid model (2.6)–(2.10) with electron diffusion, but we can establish the expression (A.1) as an upper bound for the free electron density n_e^- behind the front; this upper bound is actually a very good approximation to the real value as table 2.4 shows. The upper bound is constructed as follows:

In the ionization source term $\mathcal{S}$ (2.8), we follow the usual procedure to take only the drift term of the electron current into account. We note at this place that this assumption requires some reconsideration, and one could argue that the complete current should be taken into account and that a decomposition into a drift and a diffusion part is artificial. This argument will have to be elaborated at some other place. We here just change the source term into

$$\mathcal{S}_j = |\mathbf{j}_e| \, \alpha(E), \qquad (A.2)$$

while keeping the equations unchanged otherwise. This change of the source term means that more ionization is created at each part of the front, and therefore the ionization level behind the front will be higher. This is because in a negative front, drift current and diffusion current point into the same direction, and therefore

$$|\mathbf{j}_e| = \left| -\underline{\mathbf{D}}(E) \cdot \nabla n_e - \mu(E) \, \mathbf{E} \, n_e \right| \gtrsim \mu(E) \, |\mathbf{E}| \, n_e. \qquad (A.3)$$

The dominant part of the current is the drift or Ohmic part, therefore the results with the changed source term (A.2) should be close to the original problem.

According to Maxwell's equations, the divergence of the total current vanishes

$$\nabla \cdot (\epsilon_0 \, \partial_t \mathbf{E} + \mathbf{j}) = 0, \tag{A.4}$$

where $\mathbf{j}$ is the electric current; in our case it is $\mathbf{j} = -\mathrm{e} \, \mathbf{j}_e$ with $\mathbf{j}_e$ from (2.7). If the front is planar, and if the electric field E^+ in the non-ionized region does not change in time, then it follows immediately that

$$\epsilon_0 \, \partial_t E = \mathrm{e} \, j_e \tag{A.5}$$

Now the growth of the ion density (2.6) is bounded by the source term (A.2) and the identity (A.4) is inserted:

$$\begin{aligned}
\partial_t n_p &= \mathcal{S} = \mu(E) \, |\mathbf{E}| \, n_e \, \alpha(E) \\
&\lessgtr \mathcal{S}_j = j_e \, \alpha(E) = \frac{\epsilon_0}{\mathrm{e}} \, \partial_t E \, \alpha(E).
\end{aligned} \tag{A.6}$$

The first and last expression in this inequality can be integrated in time with the result

$$n_p(\mathbf{x}, t) - n_p(\mathbf{x}, 0) \lessgtr \frac{\epsilon_0}{\mathrm{e}} \int_{E(\mathbf{x}, 0)}^{E(\mathbf{x}, t)} \alpha(e) \, de. \tag{A.7}$$

Now the time interval $[0, t]$ is taken in such a way that it contains the time range in which the ionization front passes over the point $\mathbf{x}$ of observation. $n_p(\mathbf{x}, 0)$ is then the ion density before and $n_p(\mathbf{x}, t)$ the ion density behind the front. As a result, we find that the expression (A.1) indeed is an upper bound and good approximation for the ionization level behind the front.

We finally note if there is electron attachment and positive and negative ions $n_{p,n}$ are formed, the statement stays true for the total ion charge density $n = n_p - n_n$ if the total source and sink term for the ion density n can be written in the form (A.2).

Appendix B

Total and differential cross sections for electron-N$_2$ collisions

We cannot measure the exact values of DCS for molecules intrinsically. Of course, we can measure the approximate values of DCS for molecules, but can measure the exact values of DCS for atoms.

M Hayashi and Y. Nakamura [104]

The electron-neutral collision is one of the fundamental parts in the study of generation and propagation of streamers. The modeling of the electron-neutral collisions requires knowledge of the energy and angle dependent differential scattering cross sections for a variety of collision processes. The differential cross section (DCS) is the number of particles per unit time that falls into the solid angle $d\Omega(\chi, \theta)$ per unit flux density of the incoming beam, where χ and θ are the longitudinal and transversal angle between the electron velocities before and after the collision. By integrating the DCS over all solid angles, one can obtain the total cross section (CS). The differential cross section $d\sigma/d\Omega$ and the total cross section $\sigma(\epsilon)$ are related through

$$\frac{d\sigma}{d\Omega}(\epsilon, \chi) = Q(\epsilon, \chi)\frac{\sigma(\epsilon)}{4\pi} \tag{B.1}$$

$$\int_0^\pi Q(\epsilon, \chi) \sin \chi d\chi = 2.0 \tag{B.2}$$

where ϵ is the energy of the incoming electron in eV. The distribution in the angle θ is isotropic. The factor Q is normalized so that Eq.(B.1) will yield the correct total cross section when integrated over all angles.

The importance of the DCS for electron-molecule collisions in the particle simulation has been discussed in Sect. 5.2.2 and also by other authors [130, 168]. With different sets of DCS, particle simulations can generate different electron energy distribution functions (EEDF), mobilities, diffusion rates and reaction rates of electrons in swarm experiments, and also different rates for the run-away electron generation.

Finding suitable DCS is not an easy task. Enormous amount of measured data are published in the literature, but widely scattered. To develop our particle code for

streamer simulations in both N_2 and air, we did a literature search to find the angle- and energy-dependent differential collision cross sections for electron scattering on N_2 and O_2. The DCS used in our model for nitrogen is described in Sect. 2.2.1 and Sect. 5.2. After the model had been developed, the effort of looking for more suitable data expanded from available measurements and theoretical calculations to reviews, compilations, and other published discharge models.

The literature review on DCS is motivated by two needs in the development of our model. First, by collecting the measured data, one aims at the particle model generated electron mobility, diffusion rate, and ionization rate to be close to the laboratory measurement. The electron-molecule collision is difficult to model because one needs realistic DCS for elastic, inelastic, and ionizing collisions and also spectra of ejected electrons in the ionizing collision. The qualities of the measured properties depend on the quality of gas and electron source, instrument setup, energy calibration of electrons, angular bias and other sources, while the theoretical calculations in general need assumptions. Although better data are generated while electron collision experiments and theoretical calculations increase in both type and sophistication, integrating them together into a particle model does no guarantee a good agreement with the measured electron transport coefficients.

Second, we would like to study run-away electrons and energetic radiation. The run-away phenomenon is a result of decreasing probability of electron interactions with neutral molecules for electron energies in the range from $\sim$150 eV to $\sim$1 MeV [101]. The phenomenon can be better understood from Fig. 5.2 where the total cross section starts to decrease beyond $\epsilon_{cr} = 150$ eV in pure N_2. Due to the reduced probability of collisions of electrons with energies above ϵ_{cr}, the electron will continue to be accelerated to very high runaway energies as long as a sufficient high electric field is present. The production of runaway electrons in the Earth's atmosphere has recently been linked to X-ray and Gamma-ray burst observed during lightning discharges. To study the possible run-away electrons from the streamer simulation, the particle model needs DCS of the high energy (> 1000 eV) electrons which we haven't included in our model.

B.1 Literature review of differential cross sections

Our review starts from the bibliography of electron cross sections with atoms and molecules compiled by M. Hayashi [104]. The Bibliography was prepared as a preprint of work performed as a collaboration research of the National Institute for Fusion Science of Japan, and it covers 17 atoms and 51 molecules. For nitrogen alone, it includes 2240 papers published between 1906 and 2000.

Table B.1: Electron-molecular collision total CS and DCS summarized by S. Trajmar for nitrogen.

Processes	Energy (eV)	Ref.
total CS	0.5- 51.33	A. Kennerly [119]
	17.5-750	Blaauw *et al.* [25]
	100-1600	Dalba *et al.* [61]
	2.2-700	Hoffman *et al.* [108]
	0.3-1.56	Baldwin [17]
elastic (CS)	20-800	Dubois[1] *et al.* [67]
	1.5-400	Shyn[1] *et al.* [223]
	7.0-75	Srivastava[1] *et al.* [228]
	13-100	T.G. Finn[1] *et al.* [82]
elastic (DCS)	300-500	Bromberg *et al.* [44]
	100-3000	Jansen *et al.* [114]
rotational(0,1) (DCS)	theoretical	I. Shimamura [220]
	1-4	S.F. Wong *et al.* [261]
	2.22-2.47	K. Jung *et al.* [117]
vibrational (0,1,2,3) (CS)	2.2-2.54	K. Jung *et al.* [117]
	3-30	H. Tanaka[1] *et al.* [238]
	5-75	D.G. Truhlar[1] *et al.* [242, 243]
vibrational (0,1,2,3) (DCS)	18-28	Z. Pavlovic *et al.* [192]
electronic		
$A^3\Sigma_u^+$ (CS)	8-40	W.L. Borst *et al.* [31]
$A^3\Sigma_u^+$, and others (DCS)[2]	10-50	D.C. Cartwright *et al.* [53]
$B^3\Pi_g$ (CS)	11.5-27	D.E. Shemansky *et al.* [217, 218]
$a^1\Pi_g$ (CS)	8-40	W.L. Borst *et al.* [31]
	10-208	J.M. Ajello [5]
	60-2000	J.F.M. Aarts *et al.* [1]
$C^3\Pi_u$	11.5-25	D.E. Shemansky *et al.* [217, 218]
	-1000	J.F.M. Aarts *et al.* [1]
$E^3\Sigma_g^+$	11-14	W.L. Borst *et al.* [32]
$b'^1\Pi_u$	-500	E.C. Zipf *et al.* [264]

---

[1]The DCS are also measured or calculated with the same or similar energy range.

[2]D.C. Cartwright, A. Chutjian, S. Trajmar, and W. Williams [53] published their integral and differential cross sections for electron-N_2 impact excitation with an extensive coverage of electronic states, including $A^3\Sigma_u^+$, $B^3\Pi_g$, $W^1\Delta_u$, $W^3\Delta_u$, $a^1\Pi_g$, $C^3\Pi_u$, $B'^3\Sigma_u^-$, $a'^1\Sigma_u^-$, and $E^3\Sigma_g^+$.

A number of the review articles in the literature present compilations and critical assessment of cross-sections available at their times. Here we will mainly look at the review paper by Trajmar [241], Brunger and Buckman [46], and Yukikazu Itikawa [112]. There are also a lot of special journal issues on the topic of electron-molecule collisions. For example in 1994, the special issue of Advances in Atomic, Molecular and Optical Physics (AAMOP) on CS data [20] covered most new techniques in the CS measurement and calculation in the 1980's. But the content of these special issues largely overlap with the above mentioned review articles.

In 1983 S. Trajmar [241] published a compilation of electron-molecule scattering for more than 24 molecules including N_2. Measurements from different experiments in the 1970's are listed together and their techniques are discussed. For N_2, it contains the total CS up to 1600 eV and DCS for the elastic, rotational, vibrational and some of the electronic excitation collisions. The measurements and calculation results are summarized in Table B.1 and classified by their collision process, the energy range of the measured CS or DCS, and the authors and the reference.

Table B.2: Electron-molecular collision total CS and DCS summarized by M.J. Brunger and S.J. Buckman for nitrogen.

Processes	Energy (eV)	Ref.
total CS	0.08-10	W. Sun *et al.* [233]
	0.1-1.5	W. Sohn *et al.* [227]
	0.05-1.5	K. Jost *et al.* [116]
	0.1-1.3	J. Ferch *et al.* [80]
	Theory	C.J. Gillan *et al.* [91]
	Theory	N. Chandra *et al.* [55]
	Theory	M.A. Morrison *et al.* [166]
elastic (CS)	0.08-10	W. Sun [3] *et al.* [233]
	0.1-1.5	W. Sohn [3] *et al.* [227]
	20-100	J.C. Nickel [3] *et al.* [176]
	10-200	M. Gote [3] *et al.* [96]
elastic (DCS)	Theory	N. Chandra *et al.* [55]
	Theory	M.A. Morrison *et al.* [166]
rotational(0,2,4,6,8) (CS)	10-200	M. Gote [3] *et al.* [96]
vibrational (0,1,2,3,4) (CS)	0.5-1.5	W. Sohn [3] *et al.* [227]
	2-5	M.J. Brennan [3] *et al.* [35]
Continued on Next Page...		

---

[3]The DCS is also measured or calculated with the same or similar energy range.

Processes	Energy (eV)	Ref.
	2-5	M.J. Brunger [3] *et al.* [49]
	0-5	M. Allan [3] [11]
	20-50	A.G. Middleton *et al.* [159]
electronic		
$A^3\Sigma_u^+$ (CS)	15-50	L. Campbell[4] *et al.* [50]
$A^3\Sigma_u^+$ (DCS)	Theory	C.J. Gillan *et al.* [92]
	15	P. Zetner *et al.* [263]
	15-50	M.J. Brunger *et al.* [47]
	15-20	L.R. Leclair *et al.* [135]
$B^3\Pi_g$ (CS)[2]	15-50	L. Campbell *et al.* [50]
$B^3\Pi_g$ (DCS)	15	P. Zetner *et al.* [263]
	15-50	M.J. Brunger *et al.* [47]
$W^3\Delta_u$(CS)[2]	15-50	L. Campbell *et al.* [50]
$W^3\Delta_u$(DCS)	15-50	M.J. Brunger *et al.* [47]
$B'^3\Sigma_u^{-}$[2] (CS)	15-50	L. Campbell *et al.* [50]
$B'^3\Sigma_u^{-}$ (DCS)	15-50	M.J. Brunger *et al.* [47]
$a'^1\Sigma_u^{-}$[2] (CS)	15-50	L. Campbell *et al.* [50]
$a'^1\Sigma_u^{-}$ (DCS)	15-50	M.J. Brunger *et al.* [47]
$a^1\Pi_g$ (CS)	9-141	N.J. Mason *et al.* [154]
	10-200	J.M. Ajello *et al.* [4]
	15	P. Zetner [3] *et al.* [263]
	15-50	L. Campbell *et al.* [50]
$a^1\Pi_g$ (DCS)	15-50	M.J. Brunger *et al.* [47]
$W^1\Delta_u$ (CS)[2]	15-50	L. Campbell *et al.* [50]
$W^1\Delta_u$ (DCS)	15-50	M.J. Brunger *et al.* [47]
$C^3\Pi_u$ (CS)	11-20	M. Zubek *et al.* [265]
	11-17	G. Poparic *et al.* [198]
	15-50	L. Campbell *et al.* [50]
$C^3\Pi_u$ (DCS)	15-50	M.J. Brunger *et al.* [47]
$E^3\Sigma_g^+$ (CS)	11.8-12.7	M.J. Brunger *et al.* [48]
	17.5-20	M. Zubek [3] *et al.* [265]
	11.9-12.13	G. Poparic *et al.* [199]
	15-50	L. Campbell *et al.* [50]
$E^3\Sigma_g^+$ (DCS)	15-50	M.J. Brunger *et al.* [47]

Continued on Next Page. . .

[4]Campbell *et al.* [50] derived CS for electronic excitations from the data of Brunger and Teubner [47].

Table B.2 – Continued

Processes	Energy (eV)	Ref.
$a''\Sigma_g^+$ (CS)	17.5-20	M. Zubek [3] et al. [265]
	15-50	L. Campbell et al. [50]
$a''\Sigma_g^+$ (DCS)	15-50	M.J. Brunger et al. [47]

The long review paper of Brunger and Buckman [46] in 2002 concentrates on DCS of electron collision with diatomic molecules like N_2, O_2, H_2, CO and NO. The measurements and the theoretical calculations in the 1980's and 1990's are well summarized and their results are compared with each other. Though the data is available at a higher energy range, the comparison is limited to within 50 eV. A clear fact is that with different experimental setups and techniques the measurements largely disagree with each other and with the earlier data, for example, there is a discrepancy of 20% of the total cross-sections or of 25% in the elastic collision DCS of electron at 0.55 eV. Brunger and Buckman also discussed the possible reasons for the long-standing discrepancies within the various experiments, and between experiment and theory, for example, the itinerant nature of the resonance profile between 2 and 4 eV. The discussed data sets are summarized in Table B.2, in which the measurements and theoretical calculations overlapping with Trajmar's review [241] are excluded.

Yukikazu Itikawa [112] recently collected and reviewed the electron-N_2 CS for: total scattering, elastic scattering, momentum transfer, excitations of rotational, vibrational and electronic states, dissociation, ionization, and emission of radiation. This report surveyed the literature within the last two decades. After reviewing available cross section data till the end of 2003, a set of recommended values of CS for each above mentioned collision process is given in the form of plots or tables. (Note that it is only for total CS, not for DCS). The total scattering, elastic scattering, some of the higher states of electronic scattering, and ionization are for the electrons in the energy range up to 1000eV, while the lower states electronic scattering CS covers up to 50 eV.

In the last 5-10 years, the major interest of measurements, theory and computations of electron-molecule collisions has transfered to studies of collision with polyatomic molecules, including bio-molecules and the electronic excitation at near threshold energies [121]. However, there are still some groups active in the improvement of measurements and calculation of DCS for electron-N_2 collisions [199, 12, 120, 115, 122, 172]. For example, Khakoo et al. and Johnson et al. published their measurements of the CS [115] and DCS [120] for electron impact excitation of

$A^3\Sigma_u^+$, $B^3\Pi_g$, $W^3\Delta_u$, $B^{'3}\Sigma_u^-$, $a^{'1}\Sigma_u^-$, $a^1\Pi_g$, $w^1\Delta_u$, and $C^3\Pi_u$, and M. Allan [12] also published new measurements of the DCS for elastic and v = 0-1 vibration excitation collisions.

The energy distribution of the secondary electrons ejected upon ionization collisions are important in a particle model [244]. There are several measurements of the angular and energy distribution, or the so called doubly differential cross section (DDCS) for ionization of N_2. Of these, the energy distribution of the ejected electrons measured by Opal *et al.* [182] has become a standard and their empirical fitting equation is widely used in different simulation groups. Later Goruganthu *et al.* [95] measured DDCS at 200, 500, 1000, and 2000 eV of the incident electron energy and the two sets of data are overall in good agreement.

B.2 Differential cross sections used by various authors

B.2.1 Model 1: Tzeng and Kunhardt

Tzeng and Kunhardt [129, 128, 244, 130] simulated an electron avalanche with a particle model and discussed the influence of the scattering angle and the energy partition in ionization collisions on the swarm properties. A total of 26 collision processes were included in the simulations. The sources for the cross sections for each process are summarized in Tabel B.3.

Kunhardt and Tzeng studied the influence of DCS on the EEDF and the reaction rates of a particle simulation swarm [129]. The DCS for elastic collisions are listed in Table B.4. The angular scattering for inelastic collisions was determined using the elastic DCS which is not a satisfactory assumption but most particle models adopt this technique.

Tzeng and Kunhardt also studied the effect of the energy partition in ionization collisions on the electron velocity distribution and reaction rate of different collision processes [244]. Four ways of partition were discussed: *i*) primary electrons take all, *ii*) Opal's empirical fit, *iii*) secondary electrons randomly take from zero up to half of the available energy, and *iv*) equal sharing. The differences in the EEDF and the reaction rates of the studied electron swarm increase as the applied fields increase. In their later work [130], Opal's empirical fit [182] is used for the energy partition in an ionization collision.

B.2.2 Model 2: KITES

KITES is a kinetic theory computer code for modeling the behavior of atmospheric electrons in the presence of strong, short-duration, fast-risetime or high-frequency

Process	Energy (eV)	Ref.
total CS [a]	0-0.3	A.G. Engelhardt *et al.* [78]
	0.3-5	D.E. Golden [94]
	5-15	E. Bruche *et al.* [45]
	15-750	H.J. Blaauw *et al.* [25]
	750-1600	G. Dalba *et al.* [61]
	1600-	Born approximation
rotational		A.V. Phelps and L.C. Pitchford [195]
vibrational		A.V. Phelps and L.C. Pitchford [195]
electronic		A.V. Phelps and L.C. Pitchford [195]
dissociative ionization	0-1000 eV	D. Rapp *et al.* [206]
ionization	0-1000	D. Rapp *et al.* [206]
	1000 - 20 k	B.L. Schram *et al.* [213]

[a]The elastic collision CS are defined as $\sigma_{elastic} = \sigma_{total} - \sum_i^m \sigma_{i,inelastic}$, where there are m=25 inelastical collision processes including ionization collision.

Table B.3: *CS set used by Tzeng and Kunhardt*

Energy (eV)	Ref.
0-100	T.W. Shyn *et al.* [224]
100-500	H. Kambara *et al.* [118]
500-	extrapolation method

Table B.4: *DCS set used for elastic collision by Tzeng and Kunhardt*

electromagnetic fields [170]. The model uses only experimentally measured cross sections as input and contains almost no free parameters [171]. The validity of the model was checked by comparing the results of KITES calculations with an analytic model and experimentally measured steady-state electron transport parameters and a good agreement is found [170]. The CS used in KITES are summarized in Table B.5.

One highlight of the KITES is that different DCS have been used for different collision processes. Here we summarize them in Table B.6. One interesting point is that to implement the measured DCS in a Monte Carlo procedure, they found fit formulas of the DCS for the electronic excitation and ionization collisions, and as for those no fit formula was available, they developed their own fit formula for the elastic, rotation and vibration collisions.

Process	Energy (eV)	Ref.
elastic	0-10k	A.V. Phelps and L.C. Pitchford [195]
	> 10k (theory)	J.H. Jacob [113]
rotational		A.V. Phelps and L.C. Pitchford [195]
vibrational		A.V. Phelps and L.C. Pitchford [195]
electronic	fit formula [a].	P.M. Banks and G. Kockarts [18]
dissociative ionization	0-1000 eV	D. Rapp *et al*. [206]
ionization	0-1000	D. Rapp *et al*. [206]
	1000 - 15 k	Opal *et al*. [182]
	15 k -	C.L. Longmire and H.J. Longley [146]

[a]It is a fit given by Banks and Kockarts with some modifications. The fits are compared with the experimental data of Cartwright *et al*. [54]

Table B.5: *CS set used by KITES*

Process	Ref.
elastic	T.W. Shyn [a] *et al*. [224]
rotational	S.F Wong *et al*. [261]
vibrational	L.S. Polak *et al*. [197]
electronic	D.C. Cartwright[b] *et al*. [53]
ionization	Opal *et al*. [182]
	R.D. Dubois *et al*. [68]

[a]It is a fit formula developed for the data of Shyn et al. [224]. The formula makes the DCS much easier to be implemented in a Monte Carlo procedure.

[b]Cartwright et al. [54] gave several fit formulas with their CS and DCS data.

Table B.6: *DCS set used by KITES*

B.2.3 Model 3: Babich

Babich *et al*. [16] published their work on the simulation of relativistic runaway electrons. The work contains two parts: the Monte Carlo particle simulation and the kinetic equation simulation. Due to their physical interests, the quality of CS and DCS at the higher energy range of $\epsilon > 0.1$ MeV is more important than at lower energies. Their particle model only follows electrons with energies above 1 keV.

The electron-molecule interactions incorporated in their model are elastic scattering, bremsstrahlung, excitation scattering and ionization of the K-shell. The CS for those collision processes are taken from the International Atomic Energy Agency (IAEA) data service library [60]: EEDL97 (electrons), EPDL97 (Photon-radiation)

Process	Energy (eV)
elastic	$10 - 10^{11}$
bremsstrahlung	$10 - 10^{11}$
excitation	$11.48 - 10^{11}$
ionization K(1S1/2) subshell	$404.85 - 10^{11}$
ionization K(2S1/2) subshell	$24.1 - 10^{11}$
ionization K(2p1/2) subshell	$12.04 - 10^{11}$
ionization K(2p3/2) subshell	$12.03 - 10^{11}$

Table B.7: *EEDL97 collision processes*

and EADL97 (relaxation of atomic shells). The library contains the photon and electron interaction database for atom and molecule species with atomic numbers from 1 to 100. The collision processes included in EEDL97 for N_2 are listed in Table B.7.

The EEDL97 also includes the DCS for elastic scattering. For the other collision processes, the electron is assumed to continue along its original direction of travel, so angular distributions are not given. This is obviously wrong for the low energy electrons, but a proper assumption for runaway electrons since such high energy particles scatter mostly in the forward direction in collisions. For bremsstrahlung, both the outgoing electron and the photon are described. The photon energy spectra are given, but angular distributions are not. For the electron, the average energy loss is given. The energy losses are also given for the excitation and ionization collisions.

B.2.4 Model 4: Dowds

Dowds [65] studied the streamer avalanche with a two-dimensional particle model. The model is rather simple since only ionization and elastic collisions are included and the CS of the elastic collisions is taken as a constant. The ionization collision cross section is fitted by a formula from the electron impact excitation and ionization collision database [124] of the National Institute of Standards and Technology (NIST). The database includes total ionization cross sections of around 100 different molecules and also includes cross sections for some atoms and energy distributions of ejected electrons for H, He, and H_2.

The NIST ionization CS covers the energy range from the ionization threshold energy up to 5000 eV for the electron-N_2 collisions. The fit formula is

$$\sigma_{ion}(k) = \frac{1}{k} \left[A \ln(k) + \frac{B \ln(k) + C(k-1)}{k+D} \right]$$ (B.3)

where $k = \epsilon/\epsilon_{ion}$, in which ϵ and ϵ_{ion} are the energy of the impacting electron and

Process	Energy (eV)	Ref.
total CS	0-0.4	A.V. Phelps and L.C. Pitchford [195]
	0.4-250	Szmytkowski *et al.* [236]
	250-600	H.J. Blaauw *et al.* [25]
	600-5000	G. Garcia *et al.* [87]
	5000-10000	A.V. Phelps and L.C. Pitchford [195]
rotational		A.V. Phelps and L.C. Pitchford [195]
vibrational		A.V. Phelps and L.C. Pitchford [195]
electronic		A.V. Phelps and L.C. Pitchford [195]
ionization		A.V. Phelps and L.C. Pitchford [195]

Table B.8: *CS set used by G.D. Moss and V.P. Pasko et al. [168]*

the ionization threshold energy. The constants A, B, C and D are functions of the impacting electron energy. The formula has been compared with several sets of the experimental measurement and shows a good agreement.

B.2.5 Model 5: Moss and Pasko

Recently Moss and Pasko *et al.* [168] studied the possible run-away electrons under the influence of a one dimensional simplified streamer electric field in air. A group of low energy electrons move and are accelerated in the field. They observed that the electrons can be accelerated from a few eV to up to 8 keV, hence the streamer head can produce thermal runaway electrons. The model therefore covers a large energy range of electron molecule collision DCS. Three gas species are included in the model: N_2, O_2 and Ar.

The composition of the CS data used in this paper [168] is similar to those of Tzeng and Kunhardt [129, 128, 244, 130]. The total CS is mainly from experimental measurements while the excitation and ionization collisions are from Phelps and Pitchford [195]. And the CS of the elastic collision is the difference of the total CS with the CS of inelastic collisions. The CS used in their model for N_2 are summarized in Table B.8.

The DCS for elastic collisions are divided into two parts: electrons with energy below 500 eV and above 500 eV; as in [129, 128, 244, 130], the angular scattering for inelastic collisions was determined using the elastic DCS. For electrons with an energy below 500 eV, the DCS is the same as used by Tzeng and Kunhardt. Four analytical or empirical fit formulas are given for electrons with energy above 500 eV and compared with the experimental data of Kambara [118] at 500 eV.

B.2.6 Model 6: Chanrion and Neubert

The CS data set from the BOLSIG package are used in our particle model [42, 137, 138], and also in the particle model of Chanrion and Neubert [56], which has been developed to study the distribution and acceleration of electrons in sprite-like discharge in air. The model used SIGLO data for electron-N_2 collisions up to 1000 eV, then the CS are extrapolated to high energies up to 100 keV by a first Born approximation [141] for the elastic cross section and a Born-Bethe approximation [111] for the inelastic cross section.

As in our model, the DCS comes from Okhiromovskyy's scattering formula which is based on the screened Coulomb potential between electrons and neutral molecules [181]. The difference between isotropic scattering and anisotropic scattering also has been tested.

B.3 Fit formulas for differential cross sections

The laboratory measured DCS are mostly published in tables in which the probabilities of one or several angles are listed for electrons at one or more energy levels. It is normally difficult or computationally expensive to directly implement these tables in the particle model, while their empirical fits are much more convenient and cheap for the Monte Carlo sampling. The scattering process is different for low energy or high energy electrons: the dominant process is relatively short-range polarization scattering for the low energy electrons while it is a Coulomb-like collision as between charged particles for the high energy electrons. The DCS for Coulomb-like collisions can be analytically derived, but cannot be directly used in the Monte Carlo sampling [168]. A number of approximations based on screened Coulomb scattering have been developed for this reason. Here we list some well known formulas for the scattering process.

In the first Born approximation of the quantum mechanics theory of scattering [133], the normalized differential cross section for screened Coulomb scattering of an electron is

$$\frac{d\sigma}{d\Omega} = \frac{1}{4\pi} \frac{1 + 8\bar{\epsilon}}{(1 + 4\bar{\epsilon} - 4\bar{\epsilon}\cos\chi)^2},$$ (B.4)

where $\bar{\epsilon} = \epsilon/E_0$, in which ϵ is the energy of the incident electron and $E_0 = 27.21$ eV is the atomic unit of energy.

A.V. Phelps gave an analytical differential scattering cross section approximation for elastic collisions from N_2 based on a screened Coulomb type scattering [194]

$$\frac{d\sigma}{d\Omega} = \frac{1}{4\pi} \frac{1}{[1 - (1 - 2\beta(\epsilon))\cos\chi]^2},$$ (B.5)

$$\beta(\epsilon) = \frac{0.6}{[1 + \sqrt{\epsilon/50 \text{ eV}} + (\epsilon/20 \text{ eV})^{1.01}]^{0.99}} \tag{B.6}$$

in which $\beta(\epsilon)$ is an algebraic screening parameter derived to fit experimental angular distributions from Phelps and Pitchford [195].

Similar to the procedure described by Phelps [194], A. Okhrimovskyy *et al.* [181] derived another form

$$\frac{d\sigma}{d\Omega} = \frac{1}{4\pi} \frac{1 - \xi^2(\epsilon)}{[1 - \xi(\epsilon)\cos\chi]^2}, \tag{B.7}$$

where $\xi(\epsilon)$ is equivalent to "$1 - 2\beta(\epsilon)$" in Phelps notation (see Eq.(B.5)). Generally speaking, the $\xi(\epsilon)$ is a function varying in the interval (-1,1), and the formula yields different scattering probabilities if $\xi(\epsilon)$ is a different function of energy. For electron scattering on N_2, an empirical fit for $\xi(\epsilon)$ from Phelps and Pitchford [195] is

$$\xi(\epsilon) = \frac{0.065\epsilon/\text{eV} + 0.26\sqrt{\epsilon/\text{eV}}}{1 + 0.05\epsilon/\text{eV} + 0.2\sqrt{\epsilon/\text{eV}}} - \frac{12\sqrt{\epsilon/\text{eV}}}{1 + 40\sqrt{\epsilon/\text{eV}}}. \tag{B.8}$$

Surendra and coworkers [235, 234] proposed an anisotropic scattering in gases in 1990, which has been widely used. It is an analytical expression based on screened Coulomb scattering from Ar

$$\frac{d\sigma}{d\Omega} = \frac{\epsilon/\text{eV}}{4\pi[1 + (\epsilon/\text{eV})\sin^2(\chi/2)]\ln(1 + \epsilon/\text{eV})}. \tag{B.9}$$

Shveigert [222] studied the fast electrons in an electron avalanche, the electron scattering is described as

$$\frac{d\sigma}{d\Omega} = \frac{1}{4} \frac{Z(Z+1)}{(\epsilon/\text{eV})^2} q_e^4 \frac{1}{(1 - \cos\chi + 2\eta(\epsilon/\text{eV}))^2}, \tag{B.10}$$

where Z is the number of protons in the atom's nucleus and $\eta(\epsilon) = 20(\epsilon + 96)/\epsilon^2$.

To describe the electron scattering in the high energy range, a modified Rutherford cross section was introduced by Moss and Pasko [168]

$$\frac{d\sigma}{d\Omega} = \frac{\epsilon/\epsilon_1}{4\pi \arctan(\epsilon/\epsilon_1)} \frac{1}{1 + (\epsilon^2/\epsilon_1^2)\sin^4(\chi/2)}, \tag{B.11}$$

where ϵ_1 is set to 4 eV to match the experimental data of Kambara and Kuchitsu [118] for electron scattering from N_2 at 500 eV.

There are also empirical fits for the measured elastic scattering, for example, Murphy [171, 170] finds a fit for the data of Shyn *et al.* [224]

$$\frac{d\sigma}{d\Omega} = \frac{4N\eta_1(1 + \eta_1)}{(1 - \cos\chi + 2\eta_1)^2} + \frac{4(1 - N)\eta_1(1 + \eta_2)}{(1 + \cos\chi + 2\eta_2)^2}, \tag{B.12}$$

where $\eta_1 = 5.77(\epsilon)/\text{eV}^{-1.377}$ and $\eta_2 = 2.64(\epsilon/\text{eV})^{-0.896}$, the factor N is an energy dependent function varying from 0.6 to 1 from very low energy to 10 keV.

Appendix C
Potential and field coefficients in the charge simulation method

When calculating the potential and the electrostatic fields around an electrode, the distributed charge on the surface of the electrode can be replaced by discrete charges arranged inside the conductor [225, 123, 152, 2, 3]. The discrete charge is normally in the form of point, finite line and ring charges and they are arranged in such a way that the surface of the conductors is equipotential. In order to determine the magnitude of n charges elements, m points on the surface of the conductors (contour points) are chosen, and it is required that at any of these points the potential resulting from the superposition of the charges is equal to the conductor potential ϕ_c

$$\sum_{j=1}^{n} p_{i,j} \cdot Q_j = \phi_c, \qquad (C.1)$$

where Q_j is the charge elements and $j = 1, \cdots, n$, and $p_{i,j}$ the associated potential coefficients of a discrete charge element j on the ith contour point $i = 1, \cdots, m$. Once the charges of the discrete charge elements are determined, the potential at interesting points can be obtained from Eq. (C.1) and the x-, y- and z- components of the electric field field can also be calculated,

$$
\begin{aligned}
E_x(i) &= \sum_{j=1}^{n} f_x(i,j) \cdot Q_j, \\
E_y(i) &= \sum_{j=1}^{n} f_y(i,j) \cdot Q_j, \\
E_z(i) &= \sum_{j=1}^{n} f_z(i,j) \cdot Q_j,
\end{aligned}
\qquad (C.2)
$$

where $f_x(i,j)$, $f_y(i,j)$ and $f_z(i,j)$ are the field coefficients of the charged element j at the ith contour point in the x-, y-, and z- direction.

The potential coefficient p and the field coefficient f are expressed for different charge element as follows.

1. *Point charge on the z-axis:* For a point charge q_j located at the coordinate $(0, 0, z_j)$, the potential coefficient for the ith space point $p_i(x_i, y_i, z_i)$ is expressed as

$$p_{i,j} = 1/(4\pi\epsilon_0 D),\qquad(C.3)$$

where ϵ_0 is the permittivity of the free space and $D = \sqrt{x_i^2 + y_i^2 + (z_i - z_j)^2}$ is the distance between the two points. The field coefficients at the ith space point are expressed as

$$\begin{aligned}
f_x(i,j) &= x_i/(4\pi\epsilon_0 D^3), \\
f_y(i,j) &= y_i/(4\pi\epsilon_0 D^3), \\
f_z(i,j) &= (z_i - z_j)/(4\pi\epsilon_0 D^3).
\end{aligned}\qquad(C.4)$$

2. *Finite line-charge on the z-axis:* For a finite line-charge q_j extending along the z-axis between z_{j1} and z_{j2}, the potential coefficient at the ith space point $p_i(x_i, y_i, z_i)$ is expressed as

$$p(i,j) = \frac{1}{4\pi\epsilon_0(z_{j2} - z_{j1})} \ln \frac{(z_{j2} - z_i + D_2)(z_{j1} + z_i + S_1)}{(z_{j1} - z_i + D_1)(z_{j2} + z_i + S_2)},\qquad(C.5)$$

where

$$D_1 = \sqrt{x_i^2 + y_i^2 + (z_{j1} - z_i)^2}, \qquad D_2 = \sqrt{x_i^2 + y_i^2 + (z_{j2} - z_i)^2},$$

$$S_1 = \sqrt{x_i^2 + y_i^2 + (z_{j1} + z_i)^2}, \qquad S_2 = \sqrt{x_i^2 + y_i^2 + (z_{j2} + z_i)^2}.$$

The field coefficients at the ith space point are expressed as

$$\begin{aligned}
f_x(i,j) &= \frac{1}{4\pi\epsilon_0(z_{j2} - z_{j1})}\frac{x_i}{r_i}\left(\frac{z_i - z_{j2}}{r_i D_2} - \frac{z_i - z_{j1}}{r_i D_1} + \frac{z_i + z_{j1}}{r_i S_1} - \frac{z_i + z_{j2}}{r_i S_2}\right), \\
f_y(i,j) &= \frac{1}{4\pi\epsilon_0(z_{j2} - z_{j1})}\frac{y_i}{r_i}\left(\frac{z_i - z_{j2}}{r_i D_2} - \frac{z_i - z_{j1}}{r_i D_1} + \frac{z_i + z_{j1}}{r_i S_1} - \frac{z_i + z_{j2}}{r_i S_2}\right), \\
f_z(i,j) &= \frac{1}{4\pi\epsilon_0(z_{j2} - z_{j1})}\left(\frac{1}{D_2} - \frac{1}{D_1} - \frac{1}{S_1} + \frac{1}{S_2}\right).
\end{aligned}\qquad(C.6)$$

where $r_i = \sqrt{x_i^2 + y_i^2}$.

3. *Ring charge:* For a ring charge q_j centered on the axis $(0, 0, z_j)$ with radius r_j, the potential coefficient at the ith space point $p_i(x_i, y_i, z_i)$ is expressed as

$$p(i,j) = \frac{1}{2\pi^2\epsilon_0}\left(\frac{K(k_1)}{\alpha_1} - \frac{K(k_2)}{\alpha_2}\right),\qquad(C.7)$$

where $K(k)$ is the complete elliptic integral of the first kind [51, 52], and

$$k_1 = \frac{2\sqrt{r_i r_j}}{\alpha_1}, \qquad k_2 = \frac{2\sqrt{r_i r_j}}{\alpha_2},$$

$$\alpha_1 = \sqrt{(r_i + r_j)^2 + (z_i - z_j)^2}, \qquad \alpha_2 = \sqrt{(r_i + r_j)^2 + (z_i + z_j)^2},$$

in which $r_i = \sqrt{x_i^2 + y_i^2}$. The field coefficients at the ith space point are expressed as

$$
\begin{aligned}
f_x(i,j) &= \frac{x_i}{4\pi^2\epsilon_0 r_i^2} \left(\frac{[r_j^2 - r_i^2 + (z_i - z_j)^2]E(k_1) - \beta_1^2 K(k_1)}{\alpha_1 \beta_1^2} \right. \\
&\qquad \left. - \frac{[r_j^2 - r_i^2 + (z_i + z_j)^2]E(k_2) - \beta_2^2 K(k_2)}{\alpha_2 \beta_2^2} \right), \\
f_y(i,j) &= \frac{y_i}{4\pi^2\epsilon_0 r_i^2} \left(\frac{[r_j^2 - r_i^2 + (z_i - z_j)^2]E(k_1) - \beta_1^2 K(k_1)}{\alpha_1 \beta_1^2} \right. \\
&\qquad \left. - \frac{[r_j^2 - r_i^2 + (z_i + z_j)^2]E(k_2) - \beta_2^2 K(k_2)}{\alpha_2 \beta_2^2} \right), \\
f_z(i,j) &= \frac{1}{2\pi^2\epsilon_0} \left[\frac{(z_i - z_j)E(k_1)}{\alpha_1 \beta_1^2} + \frac{(z_i + z_j)E(k_2)}{\alpha_2 \beta_2^2} \right]. \qquad \text{(C.8)}
\end{aligned}
$$

where $E(k)$ is the complete elliptic integral of the second kind, and

$$\beta_1 = \sqrt{(r_i - r_j)^2 + (z_i - z_j)^2}, \qquad \beta_2 = \sqrt{(r_i - r_j)^2 + (z_i + z_j)^2}.$$

Bibliography

[1] J. Aarts and F. D. Heer. Emission cross sections for NI and NII multiplets and some molecular bands for electron impact on N_2. *Physica*, 52(1):45–73, 1971.

[2] M. Abdel-Salam and A. Hashem. Positive corona inception in point-plane gaps as influenced by a surrounding dielectric enclosure. *J. Phys. D: Appl. Phys.*, 39:5169–5175, 2006.

[3] M. Abdel-Salam, M. Nakano, and A. Mizuno. Electric fields and corona currents in needle-to-meshed plate gaps. *J. Phys. D: Appl. Phys.*, 40:3363–3370, 2007.

[4] J. Ajello and D. Shemansky. A Reexamination of Important N_2 Cross Sections by Electron Impact with Application to the Dayglow: The Lyman-Birge-Hopfield Band System and NI (119.99 nm) . *J. Geophys. Res.*, 90(A10):9845–9861, 1985.

[5] J. M. Ajello. Emission Cross Sections of N_2 in the Vacuum Ultraviolet by Electron Impact. *J. Chem. Phys.*, 53:1156, 1970.

[6] O. Aktas and N. R. Aluru. A combined continuum-DSMC technique for multiscale analysis of microfluidic filters. *J. Comput. Phys.*, 178(2):342–372, 2002.

[7] M. Akyuz, A. Larsson, V. Cooray, and G. Strandberg. 3d simulations of streamer branching in air. *Journal of Electrostatics*, 59:115–141, 2003.

[8] N. Aleksandrov and I. Kochetov. Electron rate coefficients in gases under non-uniform field and electron density conditions. *J. Phys. D: Appl. Phys.*, 29:1476–1483, 1996.

[9] F. Alexander, A. Garcia, and D. Tartakovsky. Algorithm refinement for stochastic partial differential equations: I. linear diffusion. *J. Comput. Phys.*, 182(1):47–66, 2002.

[10] F. Alexander, A. Garcia, and D. Tartakovsky. Algorithm refinement for stochastic partial differential equations II: correlated systems. *J. Comput. Phys.*, 207(2):769–787, 2005.

[11] M. Allan. Excitation of vibrational levels up to =17 in N_2 by electron impact in the 0-5 eV region. *J. Phys. B: At. Mol. Opt. Phys.*, 18(22):4511–4517, 1985.

[12] M. Allan. Measurement of the elastic and v = 0-1 differential electron N_2 cross sections over a wide angular range. *J. Phys. B: At. Mol. Opt. Phys.*, 38:3655–3672, 2005.

[13] M. Arrayás, U. Ebert, and W. Hundsdorfer. Spontaneous branching of anode-directed streamers between planar electrodes. *Phys. Rev. Letters*, 88:174502, 2002.

[14] N. Y. Babaeva and G. V. Naĭdis. Two-dimensional modelling of positive streamer dynamics in non-uniform electric fields in air. *J. Phys. D: Appl. Phys.*, 29(9):2423, 1996.

[15] L. Babich. A new type of ionization wave and the mechanism of polarzation self-acceleration of electrons in gas discharge at high overvoltages. *Sov. Phys. Dokl.*, 27:215, 1982.

[16] L. P. Babich, E. N. Donskoy, I. M. Kutsyk, A. Y. Kudryavtsev, R. A. Roussel-Dupré, B. N. Shamraev, and E. M. D. Symbalisty. Comparison of relativistic runaway electron avalanche rates obtained from Monte Carlo simulations and kinetic equation solution. *IEEE Trans. on Plasma Science*, 29(3):430–438, 2001.

[17] G. Baldwin. Nitrogen total cross section for electrons below 2.0 eV. *Phys. Rev. A*, 9:1225, 1974.

[18] P. Banks and G. Kockarts. *Aeronomy*. Academic Press, New York, 1973.

[19] E. M. Bazelyan and Y. P. Raizer. *Lightning Physics and Lightning Protection*. Institute of Physics, Bristol, 2000.

[20] B. Bederson, H. Walther, and M. Inokuti, editors. *Cross section data, 33, Advan. in Ato. Mol. and Opt. Phys.* Elsevier, Oxford, 1994.

[21] C. M. Bender and S. A. Orszag. *Advanced Mathematical Methods for Scientists and Engineers*. McGraw-Hill, New York, 1978.

[22] A. Bhoj and M. J. Kushner. Avalanche processes in an idealized lamp: II. modeling of breakdown in Ar/Xe electric discharges. *J. Phys. D: Appl. Phys.*, 37:2510–2526, 2004.

[23] A. Bhoj and M. J. Kushner. Plasma dynamics during breakdown in an HID lamp. *IEEE Trans. on Plasma Science*, 33:518, 2005.

[24] C. K. Birdsall and A. B. Langdon. *Plasma Physics via Computer Simulation*. Adam Hilger, 1991.

[25] H. Blaauw, R. Wagenaar, D. Barends, and F. de Heer. Total cross sections for electron scattering from N_2 and he. *J. Phys. B: At. Mol. Opt. Phys.*, 13(2):359–376, 1980.

[26] D. Boccippio, E. Williams, S. Heckman, W. Lyons, I. Baker, and R. Boldi. Sprites, elf transients, and positive ground strokes. *Science*, 269:1088–1091, 1995.

[27] J. Boeuf, Y. Lagmich, T. Unfer, T. Callegari, and L. Pitchford. Electrohydrodynamic force in dielectric barrier discharge plasma actuators. *J. Phys. D: Appl. Phys.*, 40:652–662, 2007.

[28] J. Boeuf and L. Pitchford. Electrohydrodynamic force and aerodynamic flow acceleration in surface dielectric barrier discharges. *J. Appl. Phys.*, 97:103307, 2005.

[29] J. P. Boeuf and E. Marode. A Monte Carlo analysis of an electron swarm in a non-uniform field: the cathode region of a glow discharge. *J. Phys. D: Appl. Phys.*, 15:2169–2187, 1982.

[30] A. Bogaerts, V. Pasko, N. Liu, S. Clestin, P. Sgur, and E. Marode. Efficient models for photoionization produced by non-thermal gas discharges in air based on radiative transfer and the helmholtz equations. *Plasma Sources Sci. Technol.*, 16:656–678, 2007.

[31] W. Borst. Excitation of several important metastable states of N_2 by electron impact. *Phys. Rev. A*, 5:648, 1972.

[32] W. Borst, W. Wells, and E. Zipf. Excitation of the metastable $e^3 \sum_g^+$ state of N_2 by electron impact. *Phys. Rev. A*, 5:1744, 1972.

[33] E. Botta, K. Dekker, Y. Notay, A. vander Ploeg, C. Vuik, F. Wubs, and P. de Zeeuw. How fast the Laplace equation was solved in 1995. *Applied Numerical Mathematics*, 24:439–455, 1997.

[34] F. Brau, A. Luque, B. Meulenbroek, U. Ebert, and L. Schafer. Construction and test of a moving boundary model for negative streamer discharges. *Phys. Rev. E*, 77(2):026219, 2008.

[35] M. Brennan, D. Alle, P. Euripides, S. Buckman, and M. Brunger. Elastic electron scattering and rovibrational excitation of N_2 at low incident energies. *J. Phys. B: At. Mol. Opt. Phys.*, 25(11):2669–2682, 1992.

[36] T. M. P. Briels, J. Kos, E. M. van Veldhuizen, and U. Ebert. Circuit dependence of the diameter of pulsed positive streamers in air. *J. Phys. D: Appl. Phys.*, 39:5201–5210, 2006.

[37] T. M. P. Briels, J. Kos, G. Winands, E. M. van Veldhuizen, and U. Ebert. Positive and negative streamers in ambient air: measuring diameter, velocity and dissipated energy. *J. Phys. D: Appl. Phys.*, 41:234004, 2008.

[38] T. M. P. Briels, E. M. van Veldhuizen, and U. Ebert. Branching of positive discharge streamers in air at varying pressures. *IEEE Trans. on Plasma Science*, 33(2):264–265, 2005.

[39] T. M. P. Briels, E. M. van Veldhuizen, and U. Ebert. Positive streamers in air and nitrogen of varying density: experiments on similarity laws. *J. Phys. D: Appl. Phys.*, 41:234008, 2008.

[40] T. M. P. Briels, E. M. van Veldhuizen, and U. Ebert. Positive streamers in ambient air and in a nitrogen-oxygen-mixture (99.8:0.2). *IEEE Trans. on Plasma Science*, 36:906–907, 2008.

[41] T. M. P. Briels, E. M. van Veldhuizen, and U. Ebert. Time resolved measurements of streamer inception in air. *IEEE Trans. on Plasma Science*, 36:908–909, 2008.

[42] W. Brok. *Modelling of Transient Phenomena in Gas Discharge*. PhD thesis, Eindhoven University of Technology, The Netherlands, 2005.

[43] W. J. M. Brok, E. Wagenaars, J. van Dijk, and J. J. A. M. van der Mullen. Numerical description of pulsed breakdown between parabolic electrodes. *IEEE Trans. on Plasma Science*, 35(5):1325–1334, 2007.

[44] J. P. Bromberg. Absolute differential cross sections of elastically scattered electrons. iii CO and N_2 at 500, 400, and 300 eV. *J. Chem. Phys.*, 52:1243, 1970.

[45] E. Bruche, D. Lilienthal, and K. Schrodter. Uber den wirkungsquerschnitt der edelgase Ar, Ne, He gegenuber langsamen elektronen. *Ann. Phys. (Leipzig)*, 389:279, 1927.

[46] M. Brunger and S. Buckman. Electron-molecule scattering cross-sections. i. experimental techniques and data for diatomic molecules. *Phys. Rep.*, 357:215–458, 2002.

[47] M. Brunger and P. Teubner. Differential cross sections for electron-impact excitation of the electronic states of N_2. *Phys. Rev. A*, 41:1413, 1990.

[48] M. Brunger, P. Teubner, and S. Buckman. Near-threshold electron-impact excitation cross section for the $e^3\sigma_g^+$ state of N_2. *Phys. Rev. A*, 37:3570, 1988.

[49] M. Brunger, P. Teubner, A. Weigold, and S. Buckman. Vibrational excitation of N_2 in the $2\pi_g$ resonance region. *J. Phys. B: At. Mol. Opt. Phys.*, 22(9):1443–1453, 1989.

[50] L. Campbell, M. Brunger, A. Nolan, L. Kelly, A. Wedding, J. Harrison, P. Teubner, D. Cartwright, and B. McLaughlin. Integral cross sections for electron impact excitation of electronic states of N_2. *J. Phys. B: At. Mol. Opt. Phys.*, 34(7):1185–1199, 2001.

[51] B. Carlson. On computing elliptic integrals and functions. *J. Math. and Phys.*, 44:36–51, 1965.

[52] B. Carlson. Elliptic integrals of the first kind. *SIAM Journal on Mathematical Analysis*, 8:231, 1977.

[53] D. Cartwright, A. Chutjian, S. Trajmar, and W. Williams. Electron impact excitation of the electronic states of N_2. i. differential cross sections at incident energies from 10 to 50 eV. *Phys. Rev. A*, 16:1013, 1977.

[54] D. Cartwright, S. Trajmar, A. Chutjian, and W. Williams. Electron impact excitation of the electronic states of N_2. i. integral cross sections at incident energies from 10 to 50 eV. *Phys. Rev. A*, 16:1041, 1977.

[55] N. Chandra and A. Temkin. Hybrid theory and calculation of e-N_2 scattering. *Phys. Rev. A*, 13:188, 1976.

[56] O. Chanrion and T. Neubert. A PIC-MCC code for simulation of streamer propagation in air. *J. Comput. Phys.*, 227(15):7222–7245, 2008.

[57] S. Chapman and T. G. Cowling. *The Mathematical Theory of Non-Uniform Gases*. Cambridge University Press, 1974.

[58] G. Colver and S. El-Khabiry. Modeling of dc corona discharge along an electrically conductiveflat plate with gas flow. *IEEE Trans. on Industry Applications*, 35(2):387–394, 1999.

[59] R. Crompton. Benchmark measurements of cross sections for electron collisions: Electron swarm methods. *Advances in Atom., Mole., and Opt. Phys.*, 32:97–148, 1994.

[60] D. Cullen, J. Hubbell, and L. Kissel. Fishpack: Efficient FORTRAN subprograms for the solution of separable elliptic partial differential equations. http://www-nds.iaea.org/epdl97/.

[61] G. Dalba, P. Fornasini, R. Grisenti, G. Ranieri, and A. Zecca. Absolute total cross section measurements for intermediate energy electron scattering. II. N_2, O_2 and NO. *J. Phys. B: At. Mol. Opt. Phys.*, 13(23):4695–4701, Dec 1980.

[62] A. Davies, C. Evans, and F. Jones. Electrical breakdown of gases: the spatial-temporal growth of ionization in fields distorted by space charge. *J. Appl. Phys.*, 28:164–184, 1964.

[63] R. Delgado-Buscalioni and P. V. Coveney. Continuum-particle hybrid coupling for mass, momentum, and energy transfers in unsteady fluid flow. *Phys. Rev. E*, 67(4):046704, 2003.

[64] S. K. Dhali and P. F. Williams. Two-dimensional studies of streamers in gases. *J. Appl. Phys.*, 62(12):4696–4707, 1987.

[65] B. J. P. Dowds, R. K. Barrett, and D. A. Diver. Streamer initiation in atmospheric pressure gas discharges by direct particle simulation. *Phys. Rev. E*, 68:026412, 2003.

[66] M. J. Druyvesteyn and F. M. Penning. The mechanism of electrical discharges in gases of low pressure. *Rev. Mod. Phys.*, 12:87, 1940.

[67] R. DuBois and M. Rudd. Differential cross sections for elastic scattering of electrons from argon, neon, nitrogen and carbon monoxide. *J. Phys. B: At. Mol. Opt. Phys.*, 9(15):2657–2667, 1976.

[68] R. DuBois and M. Rudd. Absolute doubly differential cross sections for ejection of secondary electrons from gases by electron impact. ii. 100-500-eV electrons on neon, argon, molecular hydrogen, and molecular nitrogen. *Phys. Rev. A*, 17(3):843–848, 1978.

[69] J. Dwyer. Implications of x-ray emission from lightning. *Geophys. Res. Lett.*, 31:L12102, 2004.

[70] J. Dwyer, H. Rassoul, and Z. Saleh. X-ray burss produced by laboratory sparks in air. *Geophys. Res. Lett.*, 35:L20809, 2005.

[71] J. R. Dwyer. A fundamental limit on electric fields in air. *Geophys. Res. Lett.*, 30(20):2055, 2003.

[72] J. R. Dwyer, M. A. Uman, H. K. Rassoul, M. Al-Dayeh, L. Caraway, J. Jerauld, V. A. Rakov, D. M. Jordan, K. J. R. V. Corbin, and B. Wright. Energetic radiation produced during rocket-triggered lightning. *Science*, 299(5607):694–697, 2003.

[73] U. Ebert, C. Montijn, T. M. P. Briels, W. Hundsdorfer, B. Meulenbroek, A. Rocco, and E. M. van Veldhuizen. The multiscale nature of streamers. *Plasma Sources Sci. Technol.*, 15(2):S118–129, 2006.

[74] U. Ebert and W. van Saarloos. Breakdown of the standard perturbation theory and moving boundary approximation for "pulled" fronts. *Phys. Rep.*, 337:139–156, 2000.

[75] U. Ebert and W. van Saarloos. Front propagation into unstable states: Universal algebraic convergence towards uniformly translating pulled fronts. *Physica D*, 146:1–99, 2000.

[76] U. Ebert, W. van Saarloos, and C. Caroli. Streamer propagation as a pattern formation problem: Planar fronts. *Phys. Rev. Lett.*, 77(20):4178–4181, 1996.

[77] U. Ebert, W. van Saarloos, and C. Caroli. Propagation and structure of planar streamer fronts. *Phys. Rev. E*, 55(2):1530–1549, 1997.

[78] A. Engelhardt, A. Phelps, and C. Risk. Determination of momentum transfer and inelastic collision cross sections for electrons in nitrogen using transport coefficients. *Phys. Rev.*, 135:A1566–A1574, 1964.

[79] R. E. Ewing. *The mathematics of reservoir simulation*. SIAM, Philadelphia, 1983.

[80] J. Ferch, W. Raith, and A. Schweiker. *in: E. McCarthy et al. (Eds) Proceeding of the XVII ICPEAC, p. 211*. ICPEAC, Griffith University, 1991.

[81] P. Fife. *Dynamics of Internal Layers and Diffusive Interfaces*. SIAM, Philadelphia, 1978.

[82] T. Finn and J. Doering. Elastic scattering of 13 to 100 eV electrons from N_2. *J. Chem. Phys.*, 63:4399, 1975.

[83] G. Fishman, P. Bhat, R. Mallozzi, J. Horack, T. Koshut, C. Kouveliotou, G. Pendleton, C. Meegan, R. Wilson, W. Paciesas, S. Goodman, and H. Christian. Discovery of intense gamma-ray flashes of atmospheric origin. *Science*, 264(2):1313, 1994.

[84] R. C. Franz, R. Nemzek, and J. Winckler. Television image of a large upward electrical discharge above a thunderstorm system. *Science*, 249(2):48–51, 1990.

[85] M. Füllekrug, E. Mareev, and M. Rycroft, editors. *Sprites, Elves and Intense Lightning Discharges*. Springer, Berlin, 2006.

[86] A. L. Garcia, J. B. Bell, W. Y. Crutchfield, and B. J. Alder. Adaptive mesh and algorithm refinement using direct simulation monte carlo. *J. Comput. Phys.*, 154(1):134–155, 1999.

[87] G. Garcia, A. Perez, and J. Campos. Total cross sections for electron scattering from N_2^- in the energy range 600-5000eV. *Phys. Rev. A*, 38:654–657, 1988.

[88] E. Gerken and U. Inan. A survey of streamer and diffuse glow dynamics observed in sprites using telescopic imagery. *J. Geophys. Res.*, 107:1344, nov 2002.

[89] E. Gerken and U. Inan. Streamers and diffuse glow observed in upper atmospheric electrical discharges. *IEEE Trans. on Plasma Science*, 33:282, Apr 2005.

[90] E. Gerken, U. Inan, and C. Barrington-Leigh. Telescopic imaging of sprites. *Geophys. Res. Lett.*, 27:2637–2640, sep 2000.

[91] C. Gillan, O. Nagy, P. Burke, L. Morgan, and C. Noble. Electron scattering by nitrogen molecules. *J. Phys. B: At. Mol. Opt. Phys.*, 20(17):4585–4603, 1987.

[92] C. Gillan, J. Tennyson, B. McLaughlin, and P. Burke. Low-energy electron impact excitation of the nitrogen molecule: optically forbidden transitions. *J. Phys. B: At. Mol. Opt. Phys.*, 29(8):1531–1547, 1996.

[93] E. Gogolides and H. H. Sawin. Continuum modelling of radio-frequency glow discharges. I. theory and results for electropositive and electronegative gases. *J. Appl. Phys.*, 72(9):3971–3987, 1992.

[94] D. Golden. Low-energy resonances in e^--N_2^- total scattering cross sections: the temporary formation of N_2^-. *Phys. Rev. Lett.*, 17(16):847–848, 1966.

[95] R. Gorugnthu, W. Wilson, and R. Bonham. Secondary-electron production cross sections for electron-impact ionization of molecular nitrogen. *Phys. Rev. A*, 35:540, 1987.

[96] M. Gote and H. Ehrhardt. Rotational excitation of diatomic molecules at intermediate energies: absolute differential state-to-state transition cross sections for electron scattering from N_2, CL_2, CO and HCL. *J. Phys. B: At. Mol. Opt. Phys.*, 28(17):3957–3986, 1995.

[97] L. R. Grabowski, E. M. van Veldhuizen, A. J. M. Pemen, and W. R. Rutgers. Corona above water reactor for systematic study of aqueous phenol degradation. *Plasma Chem. and Plasma Proc.*, 26(1):3–17, 2005.

[98] L. R. Grabowskin, E. M. van Veldhuizen, A. J. M. Pemen, and W. R. Rutgers. Breakdown of methylene blue and methyl orange by pulsed corona discharge. *Plasma Sources Sci. Technol.*, 16:226–232, 2007.

[99] J. M. Guo and C. H. J. Wu. Two-dimensional nonequilibrium fluid models for streamers. *IEEE Trans. on Plasma Science*, 21(6):684–695, 1993.

[100] A. Gurevich and K. Zybin. Runaway breakdown and the mysteries of lightning. *Physics Today*, 58(5):37–43, 2005.

[101] A. V. Gurevich, G. M. Milikh, and R. Roussel-Dupre. Runaway electron mechanism of air breakdown and preconditioning during a thunderstorm. *Phys. Rev. A*, 165(5-6):463–468, 1992.

[102] N. Hadjiconstantinou. Hybrid atomistic-continuum formulations and the moving contact-line problem. *J. Comput. Phys.*, 154(2):245–265, 1999.

[103] G. J. M. Hagelaar and L. C. Pitchford. Solving the Boltzmann equation to obtain electron transport coefficients and rate coefficients for fluid models. *Plasma Sources Sci. Technol.*, 14(4):722–733, 2005.

[104] M. Hayashi, editor. *Bibliography of Electron and Photon cross sections with atoms and Molecules published in the 20th century: N_2 molecule*. NIFS, Toki, Japan, 2003.

[105] F. Hegeler and H. Akiyama. Spatial and temporal distributions of Ozone after a wire-to-plate streamer discharge. *IEEE Trans. on Plasma Science*, 25:1158–1165, 1997.

[106] F. Hegeler and H. Akiyama. Ozone generation by positive and negative wire-to-plate streamer discharge. *Japan J. Appl. Phys.*, 36:5335–5339, 1997.

[107] J. O. Hirschfelder, C. F. Curtiss, and R. B. Bird, editors. *Molecular Theory of Gases and Liquids*. Wiley & Sons, New York, 1964.

[108] K. Hoffman, M. Dababneh, Y. Hsieh, W. Kauppila, V. Pol, J. Smart, and T. Stein. Total cross section measurements for positrons and electrons colliding with H_2, N_2, and CO_2. *Phys. Rev. A*, 25:1393, 1982.

[109] L. G. H. Huxley and R. W. Crompton. *The diffusion and drift of electrons in gases*. Wiley, New York, 1974.

[110] U. Inan. Gamma ray made on earth. *Science*, 307(5712):1054–1055, 2005.

[111] M. Inokuti. Inelastic collision of fast charged particles with atoms and molecules-Bethe theory revisited. *Rev. Mod. Phys.*, 43:297–347, 1971.

[112] Y. Itikawa. Cross sections for electron collisions with Nitrogen molecules. *J. Phys. Chem. Ref. Data*, 35(1):31–53, 2006.

[113] J. Jacob. Multiple Electron Scattering through a Slab. *Phys. Rev. A*, 8:226, 1973.

[114] R. Jansen, F. de Heer, H. Luyken, B. van Wingerden, and H. Blaauw. Absolute differential cross sections for elastic scattering of electrons by helium, neon, argon and molecular nitrogen. *J. Phys. B: At. Mol. Opt. Phys.*, 9(2):185–212, 1976.

[115] P. Johnson, C. Malone, I. Kanik, K. Tran, and M. Khakoo. Integral cross sections for the direct excitation of the $A^3\Sigma_u^+, B^3\Pi_g, W^3\Delta_u, B^3\Sigma_u^-, a'^1\Sigma_u^-, a^1\Pi_g, w^1\Delta_u$, and $C^3\Pi_u$ electronic states in N_2 by electron impact. *Journal of Geophysical Research (Space Physics)*, 110(A9):11311, 2005.

[116] K. Jost, P. Bisling, F. Eschen, M. Felsmann, and L. Walther. *in: J. Eighler et al. (Eds) Proceeding of the XII ICPEAC, p. 91*. ICPEAC, Beilin, 1983.

[117] K. Jung, T. Antoni, R. Muller, K. Kochem, and H. Ehrhardt. Rotational excitation of N_2, CO and H_2O by low-energy electron collisions. *J. Phys. B: At. Mol. Opt. Phys.*, 15(19):3535–3555, 1982.

[118] H. Kambara and K. Kuchitsu. Measurement of differential cross sections of low-energy electrons elastically scattered by gas molecules, I. apparatus. *Jpn. J. Appl. Phys.*, 11(5):609–616, 1972.

[119] R. E. Kennerly. Absolute total electron scattering cross sections for N_2 between 0.5 and 50 eV . *Phys. Rev. A*, 21:1876, 1980.

[120] M. Khakoo, P. Johnson, I. Ozkay, P. Yan, S. Trajmar, and I. Kanik. Differential cross sections for the electron impact excitation of the $A^3\Sigma_u^+, B^3\Pi_g, W^3\Delta_u, B'^3\Sigma_u^-, a'^1\Sigma_u^-, a^1\Pi_g, w^1\Delta_u$, and $C^3\Pi_u$ states of N_2. *Phys. Rev. A*, 71(6):062703, 2005.

[121] M. Khakoo, M. Lima, and J. Tennyson. Advances and challenges in electroncmolecule scattering physics report of the 14th international symposium on electroncmolecule collisions and swarms. *Phys. Scr.*, 74:C7–C14, 2006.

[122] M. Khakoo, C. Malone, P. Johnson, R. Lewis, R. Laher, S. Wang, V. Swaminathan, D. Nuyujukian, and I. Kanik. Electron-impact excitation of $X^1\Sigma_g^{+1}(v''=0)$ to the $a^1\Sigma_g^1$, $b\Pi_u^1$, $c_3\Pi_u^1$, $o_3\Pi_u^1$, $b'\Sigma_u^1$, $c_4'\Sigma_u^1$, $G\Pi_u^3$, and $F\Pi_u^3$ states of molecular nitrogen. *Phys. Rev. A*, 77(1):012704, 2008.

[123] M. Khaled. A new method for computing the inception voltage of a positive rod-plane gap in atmospheric air. *ETZ-A*, 95:369–373, 1974.

[124] Y. Kim. NIST impact ionization cross section data. http://physics.nist.gov/PhysrefData/.

[125] I. Kossyi, A. Kostinsky, A. Matveyev, and V. Silakov. Kinetic scheme of the non-equilibrium discharge in nitrogen-oxygen mixtures. *Plasma Sources Sci. Technol.*, 1(3):207–220, 1992.

[126] A. A. Kulikovsky. The structure of streamers in N_2. I: fast method of space-charge dominated plasma simulation. *J. Phys. D: Appl. Phys.*, 27(12):2556–2563, 1994.

[127] A. A. Kulikovsky. Two-dimensional simulation of the positive streamer in N_2 between parallel-plate electrodes. *J. Phys. D: Appl. Phys.*, 28(12):2483–2493, 1995.

[128] E. E. Kunhardt and Y. Tzeng. Monte carlo technique for simulating the evolution of an assembly of particles increasing in number. *J. Comput. Phys.*, 67(2):279–289, 1986.

[129] E. E. Kunhardt and Y. Tzeng. Role of electron-molecule angular scattering in shaping the electron-velocity distribution. *Phys. Rev. A*, 34(3):2158–2166, 1986.

[130] E. E. Kunhardt and Y. Tzeng. Development of an electron avalanche and its transition into streamers. *Phys. Rev. A*, 38(3):1410–1421, 1988.

[131] E. E. Kunhardt, J. Wu, and B. Penetrante. Nonequilibrium macroscopic description of electrons in weakly ionized gas. *Phys. Rev. A*, 37(5):1654–1662, 1986.

[132] A. N. Lagarkov and I. M. Rutkevich. *Ionization Waves in Electrical Breakdown of Gases*. Springer, Berlin, 1994.

[133] L. Landau and E. Lifshiz. *Quantum Mechanics: Nonrelativistic Theory*. Pergamon, Oxford, 1977.

[134] B. Lay, R. Moss, S. Rauf, and M. Kushner. Breakdown processes in metal halide lamps. *Plasma Sources Sci. Technol.*, 12:8–21, 2003.

[135] L. LeClair and S. Trajmar. Absolute inelastic differential electron scattering cross sections for He, Xe, N_2 and CO at near-threshold impact energies for scattering angle 90. *J. Phys. B: At. Mol. Opt. Phys.*, 29(22):5543–5566, 1996.

[136] C. B. Leigh, U. Inan, and M. Stanley. Identification of sprites and elves with intensified video and broadband array photometry. *J. Geophys. Res.*, 106(A2):1741–1750, 2001.

[137] C. Li, W. J. M. Brok, U. Ebert, and J. J. A. M. van der Mullen. Deviations from the local field approximation in negative streamer heads. *J. Appl. Phys.*, 101:123305, 2007.

[138] C. Li, U. Ebert, and W. Brok. Avalanche to streamer transition in particle simulations. *IEEE Trans. on Plasma Science*, 36:914, 2008.

[139] C. Li, U. Ebert, W. Brok, and W. Hundsdorfer. Spatial coupling of particle and fluid models for streamers: where nonlocality matters. *J. Phys. D: Appl. Phys.*, 41:032005, 2008.

[140] C. Li, U. Ebert, and W. Hundsdorfer. Spatially hybrid computations for propagating pulled fronts. *J. Comput. Phys.*, in preparation.

[141] J. Liu. Total cross sections for high-energy electron scattering by $H_2(^1\sigma_g^+)$, $N_2(^1\sigma_g^+)$ and $O_2(^1\sigma_g^-)$. *Phys. Rev. A*, 35(2):591–597, 1987.

[142] N. Liu and V. P. Pasko. Effects of photoionization on propagation and branching of positive and negative streamers in sprites. *J. Geophys. Res.*, 109:A04301, 2004.

[143] N. Liu and V. P. Pasko. Effects of photoionization on similarity properties of streamers at various pressures in air. *J. Phys. D: Appl. Phys.*, 39:327–334, 2006.

[144] L. B. Loeb. *Electrical corona*. University of California Press, Berkeley, 1965.

[145] L. B. Loeb and J. M. Meek. *The Mechanism of the Electric Spark*. Clarendon Press, Oxford, 1941.

[146] C. Longmire and H. Longley. *Improvements in the treatment of compton current and air conductivity in EMO problems*. DNA 3192T, MRC-N-2, Mission Research Corporation.

[147] J. Lowke and J. Parker. Theory of electron diffusion parallel to electric fields. ii. application to real gases. *Phys. Rev.*, 181(1):302–311, 1969.

[148] A. Luque, F. Brau, and U. Ebert. Saffman-Taylor streamers: Mutual finger interaction in spark formation. *Phys. Rev. E*, 78:016206, 2008.

[149] A. Luque, U. Ebert, and W. Hundsdorfer. Interaction of streamers in air and other oxygen-nitrogen mixtures. *Phys. Rev. Lett.*, 101:075005, 2008.

[150] A. Luque, U. Ebert, C. Montijn, and W. Hundsdorfer. Photoionisation in negative streamers: fast computations and two propagation modes. *Appl. Phys. Lett.*, 90:081501, 2007.

[151] A. Luque, V. Ratushnaya, and U. Ebert. Positive and negative streamers in ambient air: modeling evolution and velocities. *J. Phys. D: Appl. Phys.*, 41:234005, 2008.

[152] N. Malik. A review of the charge simulation method and its applications. *IEEE Trans. on Electrical Insulation*, 24:3–20, 1989.

[153] T. Marshall, M. Stolzenburg, C. Maggio, L. Coleman, P. Krehbiel, T. Hamlin, R. Thomas, and W. Rison. Observed electric fields associated with lightning initiation. *Geophys. Res. Lett.*, 32:L03813, 2005.

[154] N. Mason and W. Newell. Electron impact total excitation cross section of the $a^1\pi_g$ state of N_2. *J. Phys. B: At. Mol. Opt. Phys.*, 20(15):3913–3921, 1987.

[155] M. McHarg, H. Stenbaek-Nielsen, and T. Kammae. Observations of streamer formation in sprites. *Geophys. Res. Lett.*, 34:L06804, 2007.

[156] J. M. Meek. A theory of spark discharge. *Phys. Rev.*, 57(8):722–728, 1940.

[157] B. Meulenbroek, U. Ebert, and L. Schafer. Regularization of moving boundaries in a laplacian field by a mixed dirichlet-neumann boundary condition: Exact results. *Phys. Rev. Lett.*, 95(19):195004, 2005.

[158] B. Meulenbroek, A. Rocco, and U. Ebert. Streamer branching rationalized by conformal mapping techniques. *Phys. Rev. E*, 69:067402, 2004.

[159] A. Middleton, M. Brunger, and P. Teubner. Vibrational excitation in isoelectronic molecules by electron impact: CO and N_2. *J. Phys. B: At. Mol. Opt. Phys.*, 25(16):3541–3549, 1992.

[160] C. Montijn. *Evolution of Negative Streamers in Nitrogen: a Numerical Investigation on Adaptive Grids*. PhD thesis, Eindhoven University of Technology, The Netherlands, 2005.

[161] C. Montijn and U. Ebert. Diffusion correction to the Raether-Meek criterion for the avalanche-to-streamer transition. *J. Phys. D: Appl. Phys.*, 39:2979–2992, 2006.

[162] C. Montijn, U. Ebert, and W. Hundsdorfer. Numerical convergence of the branching time of negative streamers. *Phys. Rev. E*, 73:065401, 2006.

[163] C. Montijn, W. Hundsdorfer, and U. Ebert. An adaptive grid refinement strategy for the simulation of negative streamers. *J. Comput. Phys.*, 219:801–835, 2006.

[164] C. Montijn, B. Meulenbroek, U. Ebert, and W. Hundsdorfer. Numerical simulations and conformal mapping analysis of growing and branching negative discharge streamers. *IEEE Trans. on Plasma Science*, 33(2):260–261, 2005.

[165] W. L. Morgan, J. P. Boeuf, and L. C. Pitchford. SIGLO cross sections. http://www.siglo-kinema.com.

[166] M. Morrison, B. Saha, and T. Gibson. Electron-N_2 scattering calculations with a parameter-free model polarization potential. *Phys. Rev. A*, 36:3682, 1987.

[167] M. Morrison and W. Trail. Importance of bound-free correlation effects for vibrational excitation of molecules by electron impact: a sensitivity analysis. *Phys. Rev. A*, 48:2874–2886, 1993.

[168] G. D. Moss, V. P. Pasko, N. Liu, and G. Veronis. Monte Carlo model for analysis of thermal runaway electrons in streamer tips in transient luminous events and streamer zones of lightning leaders. *J. Geophys. Res.*, 111:A02307, 2006.

[169] D. Moudry, H. Stenbaek-Nielsen, D. Sentman, and E. Wescott. Imaging of elves, halos and sprite initiation at 1 ms time resolution. *Journal of Atmospheric and Solar-Terrestrial Physics*, 65:509–518, 2003.

[170] T. Murphy. Development and testing of KITES. *Los Alamos National Lab. Report*, 1988.

[171] T. Murphy. Total and Differential electron collision cross sections for O_2 and N_2. *Los Alamos National Lab. Report*, 1988.

[172] J. Muse, H. Silva, M. Lopes, and M. Khakoo. Low energy elastic scattering of electrons from H_2 and N_2. *J. Phys. B*, 41(9):095203, 2008.

[173] G. V. Naidis. Effects of nonlocality on the dynamics of streamers in positive corona discharges. *Pis'ma Zh. Tekh. Fiz.*, 23:89–94, 1997.

[174] C. Nguyen, A. van Deursen, and U. Ebert. Multiple X-ray bursts from long discharges in air. *J. Phys. D: Appl. Phys.*, 41:234012, 2008.

[175] D. Nguyen, G. Deegan, and F. D'Alessandro. Fractal nature of probabilistic model of lightning discharge. *Electrical and Electronic Technology, 2001. TENCON. Proceedings of IEEE Region 10 International Conference*, 2:814–818, 2001.

[176] J. Nickel, C. Mott, I. Kanik, and D. McCollum. Absolute elastic differential electron scattering cross sections for carbon monoxide and molecular nitrogen in the intermediate energy region. *J. Phys. B: At. Mol. Opt. Phys.*, 21(10):1867–1877, 1988.

[177] L. Niemeyer, L. Pietronero, and H. Wiesmann. Fractal dimension of dielectric breakdown. *Phys. Rev. Lett.*, 52:1033–1036, 1984.

[178] S. Nijdam, C. Geurts, E. van Veldhuizen, and U. Ebert. Reconnection and merging of positive streamers in air. *J. Phys. D: Appl. Phys.*, to appear.

[179] S. Nijdam, J. Moerman, T. Briels, E. van Veldhuizen, and U. Ebert. Stereo-photography of streamers in air. *Appl. Phys. Lett.*, 92:101502, 2008.

[180] S. O'Connell and P. Thompson. Molecular dynamics in continuum hybrid computations: A tool for studying complex fluid flows. *Phys. Rev. E*, 52(6):R5792–R5795, 1995.

[181] A. Okhrimovskyy, A. Bogaerts, and R. Gijbels. Electron anisotropic scattering in gases: A formula for Monte Carlo simulations. *Phys. Rev. E*, 65:037402, 2002.

[182] C. B. Opal, W. K. Peterson, and E. C. Beaty. Measurement of secondary-electron spectra produced by electron impact ionization of a number of simple gases. *The Journal of Chemical Physics*, 55(8):4100–4106, 1971.

[183] S. Pancheshnyi. Role of electronegative gas admixtures in streamer start, propagation and branching phenomena. *Plasma Sources Sci. Technol.*, 14:645–653, 2005.

[184] S. Pancheshnyi, M. Nudnova, and A. Starikovskii. Development of a cathode-directed streamer discharge in air at different pressures: Experiment and comparison with direct numerical simulation. *Phys. Rev. E*, 71:016407, 2005.

[185] S. Pancheshnyi, P. Segur, J. Capeillere, and A. Bourdon. Numerical simulation of filamentary discharges with parallel adaptive mesh refinement. *J. Comput. Phys.*, 227(13), 2008.

[186] S. Pancheshnyi, S. Starikovskaia, and A. Starikovskii. Role of photoionization processes in propagation of cathode-directed streamer. *J. Phys. D: Appl. Phys.*, 34:105–115, 2001.

[187] S. Pancheshnyi and A. Starikovskii. Two-dimensional numerical modelling of the cathode-directed streamer development in a long gap at high voltage. *J. Phys. D: Appl. Phys.*, 36:2683–2691, 2003.

[188] V. Pasko. Topical review: Red sprite discharges in the atmosphere at high altitude: the molecular physics and the similarity with laboratory discharges. *Plasma Sources Sci. Technol.*, 16:13, feb 2007.

[189] V. Pasko, U. Inan, and T. Bell. Fractal structure of sprites. *Geophys. Res. Lett.*, 27(4):497–500, 2000.

[190] V. Pasko, U. Inan, and T. Bell. Mesosphere-troposphere coupling due to sprites. *Geophys. Res. Lett.*, 28(19):3821–3824, 2001.

[191] V. Pasko, M. Stanley, J. Mathews, U. Inan, and T. G. Wood. Electrical discharge from a thundercloud top to the lower ionosphere. *Nature*, 416:152, 2002.

[192] Z. Pavlovic, M. Boness, A. Herzenberg, and G. Schulz. Vibrational excitation in N_2 by electron impact in the 15-35-eV region. *Phys. Rev. A*, 6:676, 1972.

[193] T. B. Petrova, H. D. Ladouceur, and A. P. Baronavski. Numerical modeling of the electrical breakdown and discharge properties of laser-generated plasma channels. *Phys. Rev. E*, 76(6):066405, 2007.

[194] A. Phelps. Compilation of electron cross section used by A.V. Phelps. http://jilawww.colorado.edu/~avp/.

[195] A. V. Phelps and L. C. Pitchford. Anisotropic scattering of electrons by N_2 and its effect on electron transport. *Phys. Rev. A*, 31(5):2932–2949, 1985.

[196] L. C. Pitchford, S. ONeil, and J. R. Rumble. Extended Boltzmann analysis of electron swarm experiments. *Phys. Rev. A*, 23(1):294–304, 1981.

[197] L. Polak and D. Slovetskićić. Electron-impact vibrational excitation cross sections for molecular nitrogen. *Teplofiz. Vys. Temp.*, 10(3):645–646, 1972.

[198] G. Poparić, M. Vićić, and D. Belić. Vibrational excitation of the $C^3\pi_u$ state of N_2 by electron impact. *Chem. Phys.*, 240:283–289, 1999.

[199] G. Poparić, M. Vićić, and D. Belić. Differential cross sections at 0° and 180° for electron-impact excitation of the $E^3\sigma_g^+$ state of N_2. *Phys. Rev. A*, 66(2):022711, 2002.

[200] H. Raether. *Z. Phys.*, 107:91, 1937.

[201] H. Raether. The development of the electron avalanches in a spark channel(from observations in a cloud chamber). *Z. Phys.*, 112:464, 1939.

[202] H. Raether. *Electron Avalanches and Breakdown in Gases*. Butterworths, London, 1964.

[203] M. Rahman, V. Cooray, N. Ahmad, J. Nyberg, V. Rakov, and S. Sharma. X rays from 80-cm long sparks in air. *Geophys. Res. Lett.*, 35:L06805, 2008.

[204] Y. P. Raizer. *Gas Discharge Physics*. Springer, Berlin, 1991.

[205] V. Rakov and M. Uman. *Lighning: Physics and Effects*. Cambridge University Press, Cambridge, 2003.

[206] D. Rapp, P. Golden, and D. Briglia. Cross sections for dissociative ionization of molecules by electron impact. *J. Chem. Phys.*, 42:4081, 1965.

[207] P. Rice-Evans. Spark and streamer chambers. *J. of Phys. E*, 2:221, 1969.

[208] R. E. Robson, R. D. White, and Z. L. Petrovic. Colloquium: Physically based fluid modeling of collisionally dominated low-temperature plasmas. *Reviews of Modern Physics*, 77:1303, 2005.

[209] A. Rocco, U. Ebert, and W. Hundsdorfer. Branching of negative streamers in free flight. *Phys. Rev. E*, 66:035102(R), 2002.

[210] W. Rogowski. *Archiv Electrotech, (Berlin)*, 20:235, 1928.

[211] R. Rudd and J. Broughton. Concurrent coupling of length scales in solid state systems. *Physica Status Solidi (b)*, 217(1):251–291, 2000.

[212] N. Sato and H. Tagashira. Monte carlo simulation of the electron swarm in nitrogen under non-uniform field conditions. *J. Phys. D: Appl. Phys.*, 18:2451–2461, 1985.

[213] B. Schram, F. D. Heer, M. van der Wiel, and J. Kistemaker. Ionization cross sections for electrons (0.6-20 keV) in noble and diatomic gases. *Physica*, 31:94, 1965.

174

[214] U. Schumann and R. Sweet. A direct method for the solution of poisson's equation with neumann boundary conditions on a staggered grid of arbitrary size. *J. Comput. Phys.*, 20:171–182, 1976.

[215] P. Ségur, A. Bourdon, E. Marode, D. Beeieres, and J. Paillol. The use of an improved eddington approximation to facilitate the calculation of photoionization in streamer discharges. *Plasma Sources Sci. Technol.*, 15:648–660, 2006.

[216] D. D. Sentman, E. M. Wescott, D. L. Osborne, D. L. Hampton, and M. J. Heavner. Preliminary-results from the sprites94 aircraft campaign 1. red sprites. *Geophys. Res. Let.*, 22(10):1205–1208, 1995.

[217] D. Shemansky and A. Broadfoot. Excitation of N_2 and N_2^+ systems by electrons-i. absolute transition probabilities. *J. Quan. Spec. and Rad. Trans.*, 11(10):1385–1400, 1971.

[218] D. Shemansky and A. Broadfoot. Excitation of N_2 and N_2^+ systems by electrons-ii. excitation cross sections and N_2 1pg low pressure afterglow. *J. Quan. Spec. and Rad. Trans.*, 11(10):1401–1439, 1971.

[219] V. Shenoy, R. Miller, E. Tadmor, D. Rodney, R. Phillips, and M. Ortiz. An adaptive finite element approach to atomic-scale mechanics: the quasicontinuum method. *J. Mech. Phys. Solids*, 47(3):46, 1999.

[220] I. Shimamura. State-to-state rotational transition cross sections from unresolved energy-loss spectra. *Chemical Physics Letters*, 73:328–333, 1980.

[221] I. P. Shkarofsky, T. W. Johnston, and M. P. Bachynski. *The Particle Kinetics of Plasmas*. Addison-Wesley, 1966.

[222] V. Shveigert. Evolution of the electron distribution function in strong eletric fields. *High Temp.*, 28:35–39, 1990.

[223] T. Shyn and G. Carignan. Angular distribution of electrons elastically scattered from gases: 1.5-400 eV on N_2. II. *Phys. Rev. A*, 22:923, 1980.

[224] T. Shyn, R. Stolarski, and G. Carignan. Angular distribution of electrons elastically scattered from N_2. *Phys. Rev. A*, 6(3):1002–1012, 1972.

[225] H. Singer, H. Steinbigler, and P. Weiss. A charge simulation method for the calculation of high voltage fields. *IEEE Trans. on PAS*, 93:1660–1667, 1974.

[226] D. M. Smith, L. I. Lopez, R. P. Lin, and C. P. Barrington-Leigh. Terrestrial gamma-ray flashes observed up to 20 MeV. *Science*, 307:1085–1088, 2005.

[227] W. Sohn, K. Kochem, K. Scheuerlein, K. Jung, and H. Ehrhardt. Near-threshold vibrational excitation and elastic electron scattering from N_2. *J. Phys. B: At. Mol. Opt. Phys.*, 19(23):4017–4024, 1986.

[228] S. Srivastava, A. Chutjian, and S. Trajmar. Absolute elastic differential electron scattering cross sections in the intermediate energy region. II. N_2. *J. Chem. Phys.*, 64:1340, 1976.

[229] S. M. Starikovskaia. Plasma assisted ignition and combustion. *J. Phys. D: Appl. Phys.*, 39:265–299, 2006.

[230] H. Stenbaek-Nielsen and M. McHarg. High time-resolution sprite imaging: observations and implications. *J. Phys. D: Appl. Phys.*, 41(23):234009, 2008.

[231] V. Stojanovic and Z. Petrovic. Comparison of the results of monte carlo simulations with experimental data for electron swarms in N_2 from moderate to very high electric field to gas density ratios E/N. *J. Phys. D: Appl. Phys.*, 31(7):834–846, 1998.

[232] Q. Sun, I. Boyd, and G. Candler. A hybrid continuum/particle approach for modeling susonic, rarefied gas flows. *J. Comput. Phys.*, 194:256, 2004.

[233] W. Sun, M. Morrison, W. Isaacs, W. Trail, D. Alle, R. Gulley, M. Brennan, and S. Buckman. Detailed theoretical and experimental analysis of low-energy electron-N_2 scattering. *Phys. Rev. A*, 52:1229, 1995.

[234] M. Surendra, D. B. Graves, and G. M. Jellum. Self-consistent model of a direct-current glow discharge: Treatment of fast electrons. *Phys. Rev. A*, 41(2):1112–1125, 1990.

[235] M. Surendra, D. B. Graves, and I. J. Morey. Electron heating in low-pressure rf glow discharges. *Appl. Phys. Lett.*, 56(11):1022–1024, March 1990.

[236] C. Szmytkowski, K. Maciag, and G. Karwasz. Absolute electron scattering total cross section measurements for noble gas atoms and diatomic molecules. *Phys. Scr.*, 54:271–280, 1996.

[237] P. L. Tallec and F. Mallinger. Coupling boltzmann and navier-stokes equations by half fluxes. *J. Comput. Phys.*, 136(1):51–67, 1997.

[238] H. Tanaka, T. Yamamoto, and T. Okada. Electron impact cross sections for $I=0 \rightarrow 1$ vibrational excitation of N_2 at electron energies from 3 to 30 eV. *J. Phys. B: At. Mol. Opt. Phys.*, 14(12):2081–2088, 1981.

[239] L. Tarasova, L. Khudyakova, T. Loiko, and V. Tsukerman. Fast electrons and X rays from nanosecond gas discharges at 0.1–760 Torr. *Sov. Phys. Tech. Phys.*, 19:351, 1974.

[240] J. Townsend. *The theory of ionization of gases by collision*. Constable&Company Ltd., London, 1910.

[241] S. Trajmar, D. Register, and A. Chutjian. Electron scattering by molecules II. experimental method and data. *Phys. Rep.*, 97:219–356, 1983.

[242] D. Truhlar, M. Brandt, A. Chutjian, S. Srivastava, and S. Trajmar. Electron scattering by N_2 at 5 and 10 eV: Rotational-vibrational close-coupling calculations and crossed beam studies of vibrational excitation. *J. Chem. Phys.*, 65:2962, 1976.

[243] D. Truhlar, M. Brandt, S. Srivastava, S. Trajmar, and A. Chutjian. Quantum mechanical and crossed beam study of vibrational excitation of N_2 by electron impact at $30 \sim 75$ eV. *J. Chem. Phys.*, 66:655, 1977.

[244] Y. Tzeng and E. E. Kunhardt. Effect of energy partition in ioinizing collisions on the electron-velocity distribution. *Phys. Rev. A*, 34(3):2148–2157, 1986.

[245] L. N. L. Ullrich and N. Wiegart. The mechanism of leader breakdown in electronegative gases. *IEEE Trans. Electr. Insul.*, 24:309–324, 1989.

[246] W. van Saarloos. Front propagation into unstable states. *Physics Reports*, 386:29–222, 2003.

[247] E. M. van Veldhuizen, editor. *Electrical Discharges for Environmental Purposes: fundamentals and applications*. Nova Science Publishers, 2000.

[248] E. M. van Veldhuizen and W. R. Rutgers. Pulsed positive corona streamer propagation and branching. *J. Phys. D: Appl. Phys.*, 35:2169–2179, 2002.

[249] P. A. Vitello, B. M. Penetrante, and J. N. Bardsley. Simulation of negative-streamer dynamics in nitrogen. *Phys. Rev. E*, 49(6):5574–5589, 1994.

[250] J. Wackers. A nested-grid finite-difference poisson solver for concertrated source terms. *J. Comp. Appl. Math.*, 180:1–12, 2005.

[251] D. Wadsworth and D. Erwin. One-dimensional hybrid continuum/particle simulation approach for rarefied hypersonic flows. *AIAA paper*, 90:1690, 1990.

[252] E. Wagner, F. Davis, and G. Hurst. Time-of-flight investigations of electron transport in some atomic and molecular gases. *J. Chem. Phys.*, 47:3138–3147, 1967.

[253] G. Wagner and W. Liu. Coupling of atomistic and continuum simulations using a bridging scale decomposition. *J. Comput. Phys.*, 190:249, 2003.

[254] A. Ward. Calculations of midgap breakdown in gases. *J. Appl. Phys.*, 36:2540–2543, 1965.

[255] E. Wescott, D. Sentman, D. Osborne, D. Hampton, and M. Heavner. Preliminary results from the sprites94 aircraft campaign: 2. blue jets. *Geophys. Res. Lett.*, 22:1209–1212, 1995.

[256] E. Wescott, D. Sentman, H. Stenbaek-Nielsen, P. Huet, M. Heavner, and D. Moudry. New edvidence for the brightness and ionization of blue starters and blue jets. *J. Geophys. Res.*, 106:21549–21554, 2001.

[257] E. R. Williams. Problems in lightning physics – the role of polarity asymmetry. *Plasma Sources Sci. Technol.*, 15(2):91–108, 2006.

[258] G. Winands, Z. Liu, A. Pemen, E. van Heesch, and K. Yan. Long lifetime, triggered, spark-gap switch for repetitive pulsed power applications. *Review of Scientific Instruments*, 76(8):085107, 2005.

[259] G. Winands, K. Yan, A. Pemen, S. Nair, Z. Liu, and E. van Heesch. An industrial streamer corona plasma system for gas cleaning. *IEEE Trans. on Plasma Science*, 34(5):2426–2433, 2006.

[260] G. J. J. Winands, Z. Liu, A. J. M. Pemen, E. J. M. van Heesch, K. Yan, and E. M. van Veldhuizen. Temporal development and chemical efficiency of positive streamers in large scale wire-plate reactor as function of voltage waveform parameters. *J. Phys. D: Appl. Phys.*, 39(14):3010–3017, 2006.

[261] S. Wong and L. Dube. Rotational excitation of N_2 by electron impact: 1-4 eV. *Phys. Rev. A*, 17:570, 1978.

[262] W. Yi and P. Williams. Experimental study of streamers in pure N_2 and N_2/o_2 mixtures and a $\approx$ 13 cm gap. *J. Phys. D: Appl. Phys.*, 35(3):205–218, 2002.

[263] P. Zetner and S. Trajmar. *in: J. Geddes et al. (Eds) Proceeding of the XV ICPEAC, p. 307.* ICPEAC, Brighton, England, 1987.

[264] E. Zipf and M. Gorman. Electron-impact excitation of the singlet states of N_2. I. The Birge-Hopfield system ($b^1\pi_u - X_1\sigma_g^+$). *J. Chem. Phys.*, 73:813, 1980.

[265] M. Zubek and G. King. Differential cross sections for electron impact excitation of the $c^3\pi_u$, $e^3\sigma_g^+$ and $a''^1\sigma_g^+$ states of N_2. *J. Phys. B: At. Mol. Opt. Phys.*, 27(12):2613–2624, 1994.

Acknowledgments

I would like to thank my first supervisor Ute Ebert for her careful guidance during my Ph.D. research. I am very impressed by her energy and enthusiasm in research. Her scientific intuition has made her a constant oasis of ideas in science, which inspired and enriched my growth as a student, a researcher and a scientist as I want to be. From her I learned that scientific endeavor means much more than finding nice algorithms and implementing them in computer programs. I am deeply indebted to her.

I am deeply grateful to my co-supervisor, Willem Hundsdorfer for his advice, supervision, and for many ideas and suggestions he made with respect to the research presented in this dissertation. It was very enjoyable to work with him, not only because of his scientific experience which has nourished me, but also due to his friendly personality.

I am very glad that I have gradually learned to follow their example as I feel more and more pleasure in doing research rather than just to work hard. Above all and the most needed, they provided me with firm encouragement and support in various ways.

I would like to thank Prof. dr. Mark Kushner, dr. Leanne Pitchford and Prof. dr. Joost van der Mullen for being on the reading committee and prof. dr. ir. Gerrit Kroesen for being the committee chairman. I also would like to thank Prof. dr. Henk van der Vorst and dr. ir. Jan van Dijk for joining my Ph.D. committee.

Many thanks go, in particular, to Wouter Brok. I am much indebted to him for his valuable advices in scientific discussions, supervision and in help with writing. It is from his thesis, discussion, and many of my unintelligent questions, that I understand the Monte Carlo particle simulation.

I was very fortunate in having Rob Bisseling as my coordinator and Henk van der Vorst, Gerard Sleijpen and Will Schilder as my master thesis supervisors at Utrecht University. I especially thank Henk van der Vorst, without his axiom "An education program is to let people learn something from it", I might still be busy with my master program. I also would like to thank my classmate Tammo Jan Dijkema for the patient help and for being my basketball and football teammate, and game mate.

I also would like to thank my office mates Carolynne Montijn, Maksat Ashyraliyev, Valeriu Savcenco and Anna Mozartova for the scientific and personal discussions. Collective and individual acknowledgements are also owed to my colleagues at CWI and TU/e. Many

Curriculum Vitae

Personal Information

Date of Birth   : 07 Jan. 1978
Place of Birth   : Henan province, China
Nationality   : Chinese
Marital Status   : Single

Education and Employment:

Sept. 1996 - Sept. 1999	B.A. in Electrical and mechanical engineering, BeiHang University, Beijing, China
Sept. 1999 - Feb. 2000	Software Engineer, Motorola, Beijing, China
Feb. 2000 - May. 2002	Database Engineer, Statistical Bureau, Pingdingshan City, China
Sept. 2002 - Sept. 2003	B.A. in Production Design, Hogeschool van Utrecht, The Netherlands
Sept. 2003 - Dec. 2004	M.S. in Scientific Computing, Universiteit Utrecht (UU), The Netherlands Focus: Numerical methods, parallel computing Thesis: Mathematical Analysis of Cross Talk
Feb. 2005 - Feb. 2009	Ph.D. in Computational Science and Applied Physics, Centrum voor Wiskunde en Informatica (CWI), Amsterdam, The Netherlands Focus: Modeling and simulation of gas discharge, plasma physics Dissertation: Joining particle and fluid aspects in streamer simulations (Oral defense: 04 Feb. 2009 at TU Eindhoven, The Netherlands)

Publications:
In international journals:

[1] C. Li, W.J.M. Brok, U. Ebert, and J.J.A.M. van der Mullen, *Deviations from the local field approximation in negative streamer heads*, J. Appl. Phys. **101**, 123305 (2007).
[2] C. Li, U. Ebert, W.J.M. Brok, and W. Hundsdorfer, *Spatial coupling of particle and fluid models for streamers: where nonlocality matters*, J. Phys. D: Appl. Phys. **41**, 032005 (2008).
[3] C. Li, U. Ebert and W.J.M. Brok, *Avalanche-to-streamer transition in particle simulations*, IEEE Trans. Plasma Sci. **36**(4), 910 (2008).

In refereed proceedings:

[1] Chao Li, W.J.M. Brok, Ute Ebert, W. Hundsdorfer and J.J.A.M. van der Mullen, *Negative streamer fronts: comparison of particle and fluid models and hybrid coupling*

in space, XXVIII International Conference on Phenomena in Ionized Gases (ICPIG), 2P05-14, pp. 465-468, 2007, Prague, Czech Republic.

[2] Chao Li, W.J.M. Brok, Ute Ebert, W. Hundsdorfer and J.J.A.M. van der Mullen, *Particle and fluid models for streamers: comparison and spatial coupling*, 19th Europhysics Conference on the Atomic and Molecular Physics of Ionized Gases (ESCAMPIG), 2008, Granada, Spain.

Conference and Workshop Presentations:
Talks

Oct. 2006   *Particle versus density models for negative streamer fronts,* Seminar, Centrum voor Wiskunde and Informatica (CWI), Amsterdam, The Netherlands

Dec. 2006   *Particle versus density models and hybrid computations for negative streamer fronts,* 9th Euregional WELTPP-Workshop on the Exploration of Low Temperature Plasma Physics, Kerkrade, The Netherlands

Mar. 2007   *Particle versus density models and hybrid computations for ionization fronts,* 19th NNV-Symposium on Plasma Physics and Radiation Technology, Lunteren, The Netherlands

Oct. 2007   *Particle and fluid models for streamers: comparison and spatial coupling,* Workshop on Streamers, Sprites, Leaders, Lightning: from Micro- to Macroscales, Leiden, The Netherlands

Jun. 2008   *Particle and fluid models for streamers: comparison and spatial coupling,* Workshop on Coupling of Thunderstorms and Lightning Discharges to Near-Earth Space, Corte, France

Posters:

Dec. 2005   FOM-Decembergagen, Veldhoven, The Netherlands

Jun. 2006   Scientific ICT Research Event Netherlands (SIREN), Utrecht, The Netherlands

Jan. 2007   FOM-meeting Physics@Veldhoven, The Netherlands

Apr. 2007   *D*ynamics of Patterns Symposium, Twente, The Netherlands

Jul. 2007   XXIII IUPAP International Conference on Statistical Physics (Statphys 23), Genova, Italy

Jul. 2007   XXVIII International Conference on Phenomena in Ionized Gases (ICPIG), Prague, Czech Republic

Mar. 2008   20th NNV-symposium on Plasma Physics and Radiation Technology, Lunteren, The Netherlands

Jul. 2008   19th Europhysics Conference on the Atomic and Molecular Physics of Ionized Gases (ESCAMPIG), Granada, Spain

Sep. 2008   The Dynamics Days Europe, Delft, The Netherlands